Numerical Modelling of Optical Micro-cavity Ring Resonators for WDM Networks

Nabeil Abduljallil Abubaker Abujnah

A submission presented in partial fulfilment of the requirements of the University of Glamorgan/Prifysgol Morgannwg

for the degree of Doctor of Philosophy

This research programme was carried out in collaboration with the University of Sebha, Libya

July 2011

Certificate of Research

This is to certify that, except where specific reference is made, the work presented in this thesis is the result of the investigation undertaken by the candidate.

Signed: …….……..... (Candidate)

Signed: ……..... (Director of Studies)

Date: …….……..

Declaration

This is to certify that neither this thesis nor any part of it has been presented or is being currently submitted in candidature for any other degree other than the degree of Doctor of Philosophy of the University of Glamorgan.

Signed: ……..…… (Candidate)

Date: ……

I hereby give consent for my thesis, to be available for photocopying and for inter-library loan, and for the title and summary to be made available to outside organizations.

Signed: ……..…… (Candidate)

Date: ……

Acknowledgements

In the name of ALLAH, the most Beneficent, the most Merciful, the most Compassionate.

This thesis is dedicated to the soul of my father, may Allah forgive him and grant him his highest paradise (Ameen).

I am forever indebted to the greatest women in my life, my beloved mother, whose unconditional love and support at each time of my life made me that man that I am today. Her deep faith, her prayers, and supreme trust are always the most efficient motivation to accomplish my ultimate goal. No word can describe what you have done for me. Thank you for your selfless and endless love.

Warm thanks goes to my dearest brother, Mr. Essa and his lovely family; I will never be able to repay him for his absolute backing and support to me, meeting my needs before I knew I needed them. He has a special place in my heart.

My beloved, my wife, Reema, her prayers, patience, hard work, energy, dedication, enthusiasm, passion, support, and, most of all, her love; to these I owe where I stand today.

To the two lovely roses, my daughters Fatima and Lamar, whom have decorated my life and made it full of happiness and joy.

I wish to mention all my other brothers and sisters, who have all had a great influence in keeping me motivated throughout this PhD journey, when things made no sense, they made the PhD life look all the brighter and gave me the extra push when I needed one.

The author would also like to extend his sincere thanks to Libyan high Education ministry for their financial support.

I would like to express my gratitude to my thesis supervisor Prof. S. S. A. Obayya, whose mentorship and support made my graduate career a truly remarkable experience. Despite his busy schedule, he has always made time for discussion. In addition to the scientific side, he has also provided me with invaluable help in carefully planning and managing the different steps of my research. I have truly learned a lot during my PhD.

I would like to express my warm thanks to Dr. Rosa Letizia for her continuous and invaluable guidance. I shall always remember her for her kindness and all the support that she has given me through my study.

I would also like to thank Dr. Ramsy Selim, Dr. Domenico Pinto, and Eng. Ahmed Heikal for their valuable input academically and non-academically. They have had a positive lasting impact on me.

Lastly, I would like to offer my regards and blessing to all of those who supported me in any respect during the completion of this work as well as expressing my apologies that I could not mention them personally one by one.

To my lovely home country LIBYA

Abstract

Augmenting the level of integration for a lower cost and enhancing the performance of the optical devices have turned out to be the focus of many research studies in the last few decades. Many distinct approaches have been proposed in a significant number of researches in order to meet these demands. Optical planar waveguides stand as one of vital employed approach in many studies. Although, their low propagation loss, and low dispersion, they suffers from high power losses at sharp bends. For this reason, large radius of curvature is required in order to achieve high efficiency and compromise the high level of integration. For the purpose of this research, in this thesis different ways to improve the performance of optical microcavity ring resonators (MRRs) have been thoroughly investigated and new configurations have been proposed.

The Multiresolution Time Domain (MRTD) technique was further developed and employed throughout this thesis as the main numerical modelling technique. The MRTD algorithm is used as a computer code. This code is developed and enhanced using self built Compaq Visual Fortran code. Creating the structure and Post-processing the obtained data is carried out using self built MATLAB code. The truncating layers used to surround the computational domain were Uniaxial Perfectly Matched Layers (UPML). The accuracy of this approach is demonstrated via the excellent agreement between the results obtained in literature using FDTD method and the results of MRTD.

This thesis has focused on showing numerical efficiency of MRTD where the mesh size allowed or the total number of computed points is about half that used with FDTD. Furthermore, the MRR geometry parameters such as coupling gap size, microring radius of

curvature, and waveguide width have been thoroughly studied in order to predict and optimise the device performance.

This thesis also presents the model analysis results of a parallel-cascaded double-microcavity ring resonator (PDMRR). The analysis is mainly focus on the extraction of the resonant modes where the effect of different parameters of the structure on transmitted and coupled power is investigated.

Also, accurate analysis of 2D coupled microcavity ring resonator based on slotted waveguides (SMRR) has been thoroughly carried out for the purpose of designing optical waveguide delay lines based on slotted ring resonator (SCROW).

The SCROW presented in this thesis are newly designed to function according to the variation of the resonance coupling efficiency of a slotted ring resonators embedded between two parallel waveguides.

The slot of the structures is filled with SiO2 and Air that cause the coupling efficiency to vary which in turn control both the group velocity and delay time of SCROW structures results from the changing the properties of the bent slotted waveguide modes which strongly depends on the slot's position.

Significant improvements on the quality factor and greater delay time have been achieved by introducing sub-wavelength-low-index slot into conventional waveguide.

Table of Contents

List of Tables

List of Figures

List of Abbreviations

1D	One Dimension
2D	Two Dimensions
3D	Three Dimension
APF	All Pass Filter
AWG	Arrayed Waveguide Grating
CDF	Cohen Daubechies Feauveau
CPU	Central Processing Unit
CROWs	Coupled Resonator Optical Waveguides
CW	Continues Wave
EM	Electromagnetic
FD	Frequency Domain
FDTD	Finite Difference Time Domain
FFT	Fast Fourier Transform
FOM	Figure Of Merit
FSR	Free Spectral Range
FWHM	Full Width at Half Maximum
InP	Indium Phosphide
$LiNbO_3$	Lithium Niobate
MoM	Method of Moments
MRRs	Microcavity Ring Resonators
MRTD	Multiresolution Time Domain
OADM	Optical Add Drop Multiplexers
PDMRR	Parallel-cascaded Double Microcavity Ring Resonator

PLCs	Planar Lightwave Circuits
PML	Perfect Matching Layer
Q-factor	Quality factor
SCISSORs	Side Coupled Integrated Spaced Sequence of Resonators
SCROW	Slotted Coupled Resonator Optical Waveguide
Si	Silicon
SiO_2	Silicon Dioxide
SMRR	Slotted Micro-Ring Resonator
SMRRs	Slotted Micro-Ring Resonators
S-MRTD	Scaling Multi-Resolution Time Domain
SOAs	Semiconductor Optical Amplifiers
SOI	Silicon On Insulator
TD	Time Domain
TE	Transverse Electric Mode
TIR	Total Internal Reflection
UMPL	Uniaxial Perfectly Matched Layer
VLSI	Very Large Scale Integrated
WDM	Wavelength Division Multiplexing
WG1	Input Waveguide
WG2	Output Waveguide
WGMs	Whispering Gallery Modes

Chapter 1

Introduction

1.1 Future Trend of Optical Communications

Optical communication is one of the greatest achievements accomplished in the last century. This is due to its capability to introduce an excellent solution for the information flow. The rapidly growing volume of internet services has led to conversion from telecommunication to data communication [14, 41].

Since the digital data traffic has been quarter every year, fibre-optic communication technologies have quickly expanded in order to support this revolution. Compared to their counterpart twisted-pair and coaxial-cable, these sophisticated techniques have not only provided higher speed but also larger capacity [18].

Hence, twisted-pair and coaxial-cables are being gradually displaced. Following the establishment of long distance fibres, the check point of the optical communication system is progressing towards functional photonic components that are utilised to link the terminals and the customers. Diverse functional devices such as, optical power splitters, optical switches, and optical (de) multiplexers, are needed to either add or drop signals [33].

Planar Lightwave Circuits (PLCs) play an essential role in optical communications networks. Conventionally, PLCs suffer from a variety of problems such as polarisation dependence and optical losses. In addition, they were temperature sensitive and were restricted to only two dimensions. However, in recent years, many of these problems have been solved, making PLCs in particular attractive due to their properties of compactness, low losses, improved functionality, and also have potential for mass productivity [73, 58]. With merit to the recent advances in material technology and fabrication techniques, fabricating PLCs with complex functions has been made

possible. The requirements of conforming to the demands on integration with as many functions as possible, for the lowest cost as possible, as well as computing and signal processing devices to complement or competitively replace their microelectronic counterparts in integrated circuits, make it essential that PLCs be explored [73, 58].

In PLCs the signal is carried using optical signals rather than electrical once. This is due to the high frequency of light that, not only permits a very large bandwidth transport, but also allows huge amount of information to be managed [33]. High bandwidth and multiplexing capacity, reduced weight, immunity to electromagnetic interference, low transmission loss, high thermal and mechanical stabilities, and low power consumption are considered as figures of merit distinguishing PLCs based devices over their counterparts based on previous technologies [34]. PLCs are designed to carry out certain function such as the generation, guiding, splitting, multiplexing, amplification, switching and detection of the light signals [73].

A variety of devices based on PLC technology have been developed, including arrayed waveguide gratings [70, 36], matrix switching [93], star and multimode interference couplers [108, 72, 95]. An optical waveguide plays an essential role in constructing the photonic components in the same way that the electrical wire is used for electronics [52]. To a certain extent, photonics can be considered as the equivalent to electronics with the signal being carried using light instead of electric current. Whilst an electrical signal exists in the region of high electrical conductivity, an optical signal is travelling along in medium of high refractive index. By means of total internal reflection (TIR) of light, several of geometrical structures have been used to realise the optical waveguide.

Common examples include embedded waveguides, rectangular dielectric waveguides, dielectric strip waveguides, rib waveguides, strip-loaded waveguides and ridge waveguides [66]. Different materials have been used to construct optical waveguides including polymer [48], Silicon on Insulator (SOI) [2], InP [72], SiO_2 [5], and $LiNbO_3$ [83].

Each material has advantages and disadvantage relying on specific required functions. Due to the outstanding advantages of providing small propagation loss as well as low cost, SiO_2 stands as an ideal option for passive devices. While SOI can be a good platform for high density integration this is due to its ability for providing high-index-contrast. However, as the silicon is indirect bandgap material, it is difficult to obtain light emission. Whereas, InP can be best selected for monolithic integration because of its ability to support both active and passive optical functions [58].

1.2 Optical Microcavities

Optical microcavities can be viewed as photonic devices in which the light can be resonantly trapped in structures of physical dimension comparable to optical wavelength. Optical microcavity ring resonators stand as the most commonly used example, where light can be travelling in medium of circular geometry with curvature radius of few tens of microns. Owing to high refractive index of guiding materials, the confinement mechanism is performed by means of total internal reflection. Generally, optical microcavities play a significant role in many applications ranging from quantum electrodynamics to telecommunications components, all the way to optical sensors [6, 50].

A basic property of optical microresonators has been arisen from their size-dependent spectral response. The light, once the interference condition takes place, is particularly stored in the resonator at precise frequency values that can be used to design filters for optical communication applications [22]. In addition, these modes can resonate with high quality factor (Q) in the cavity where the long photons lifetime allows the field within the cavity to be built from a considerably weaker input. This property makes the optical cavities an ideal platform not only to realise optical sensors and studying light-matter interaction [27, 85] but it also allows for new kinds of laser devices [104].

In the last few years, research interest has been strongly directed to the design of optical ring resonators based on high-index-contrast semiconductor materials [10, 25, 37, 62]. These research efforts have clearly demonstrated that those structures naturally permit realisation of small-radius microcavities with negligible bending losses resulting in large longitudinal mode spacing. For this reason, they allow the integration of a bulky number of devices on optical circuits foreseen for very large scale integrated (VLSI) photonics [10]. Since the MRRs have been recognised as complicated structures, hence, realistic simulations that accurately predict their performance are of major importance.

There are many benefits of these simulations, some include:-

1. Saving time and cost of re-fabrication
2. Accurate analytical simulations lead to modifications and enhancements of the MRRs device that in turn leads to improved developed designs

1.3 Existing Approaches for Modelling MRRs

Since 2D MRRs have been considered as complicated structures, both analytical and numerical techniques have been adopted in order to investigate the properties of MRRs. Although analytical techniques can be used to study the physical effects of the structure, they are incapable of predicting experimental realisation [46].

Therefore, a number of numerical techniques have been developed for such complex electromagnetic structures. There are mainly two numerical techniques by which Maxwell's equations in an electromagnetic system can be analysed; frequency-domain (FD) and time-domain (TD). The FD techniques have showed significant progress [54]; however, even the most advanced FD schemes are exhausted by several volumetrically complex structures of interest. Alternatively, TD methods hold many advantages over their FD counterpart. One of the main advantages is that one simulation of MRRs devices in time-domain results in broadband information that can be analysed.

In this research, Multiresolution Time Domain scheme is successfully extended to accurately model optical devices based on MRRs. The idea behind this technique is to apply multiresolution analysis in the context of the Method-of-Moment (MoM) to discretise Maxwell's equations, where electromagnetic field components are expressed as weighted sums of specific scaling and wavelet functions in space and in time domain. Substituting these expansions into Maxwell's equations and following the wavelet-Galerkin method, an arbitrary high-order time domain scheme is derived [9, 62, 68], [106]. This scheme has proven in literature to be highly accurate if compared to most used FDTD techniques, which strongly suffer from numerical dispersion at fixed resolution in space [28, 82, 98].

1.4 Aims and Objectives

Recent years have witnessed a flurry of activities aimed at development of techniques that can lead to a significant support of the explosive expansion of high-density, ultra-fast and efficient systems in the telecommunications markets. In order to support this revolution, all-optical systems have been developed rapidly to meet the high performance characteristics required by today and next generation telecommunications.

The progress in integrated optical technology may significantly have an effect on the future rate of development of optical networks. It should be noted that despite the advances in integrated optical devices they lack in the scale of integration and level of sophistication when compared to their integrated electronic counterpart. Therefore integrating as many functions as possible is needed for low cost devices. In particular, it is desirable when the devices can be created with standard processes in mass production scale.

In addition, versatile building blocks that can not only be utilised for optical functions such as filtering, sensing, and switching, but also suitable for integration are of high necessity. Recent advances in micro and nanofabrication technology have brought a new interest in building optical devices with physical dimensions comparable to optical wavelength. Optical microcavities play an important role in modern optical communications. It can serve as flexible passive and active components in photonic integrated circuits. The requirements of achieving higher performance for the future of optical communication devices, as well as computing and signal processing devices to complement or competitively replace their microelectronic counterparts in integrated circuits, make it essential that novel optical microstructures be explored. Since the

microcavity resonators have been recognised as complicated structures, their fabrication requires ultra-high degree precision in addition to highly complicated laboratory facilities. Hence, the characteristics of these devices usually necessitate a full- wave numerical simulator that can allow for design optimisation before fabricating the device. Furthermore, accurate computations can be capable of predicting complex physical phenomena inherent in these devices.

This research work has been focused on the numerical modelling of microcavity ring resonators from time-dependent Maxwell's equations. The goal and novelty of this work is to investigate the electromagnetic wave interaction with linear Si and SiO_2 based semiconductor microring resonators and demonstrate the use of such passive devices for optical filtering and photonic delay lines.

In order to choose a particular simulation approach, generally two criteria have to be taken into account. Firstly, the desired results need to be accomplished with available resources and secondly, CPU simulation time has to be optimised to obtain these results. Since the first aspect is related to the convergence rate of the used techniques, large computational problems can be studied with a highly convergent algorithm. On the other hand, the execution simulation time not only relies on the cost of time per time step but also depends on the number of time steps that have to be carried out. Among the existing full-wave techniques, Finite Difference Time Domain is known as a popular framework for low-cost feasibility studies and permit design optimisation before fabricating the device [10]. Although this method is simple and flexible, it puts a heavy burden on computer resources particularly when modelling complicated problems with large computational domain.

For this research, the multiresolution time domain method has served as the basis for the computational studies and algorithm development. Since it was introduced in 1996 for the microwave ranges [68] and has since been extended also for the optical range [82]. This method uses a high order approximation of the derivative in space in order to reduce the numerical phase error of FDTD. By doing so, MRTD does not require the use of very fine mesh size to discretise the structure geometry, thus high numerical accuracy can be achieved while mitigating the computational burden. The possibility of saving CPU running time makes MRTD an efficient alternative numerical scheme to the commonly used FDTD for the design of optical microring structures.

1.5 New Contributions to the Knowledge

Optical microcavity ring resonator is an optical waveguide that forms a ring shaped structure whose circumference is in the range of tens of hundreds microns. Light in this manner can be coupled into and out of this structure by placing it in close proximity between another two straight waveguides.

The design and simulation play a very important role in the development of photonic devices. With appropriate simulation tools, the design of such devices becomes much more efficient. The cost for product development could be reduced dramatically by using efficient designs that give good performance and compactness. Thus this research aims at implementing a numerical, yet accurate and comprehensive model that can be utilised to explore a detailed study of the MRRs. This aim has been fulfilled through the following objectives:-

- Review of optical microcavity ring resonators
- Develop MRTD simulation of MRRs
- Numerically provide detailed study of the single MRR geometry parameters
- Model the double MRR systems and assess the system resonance mode, where the effect of different parameters of the structure on transmitted and coupled power is investigated
- Investigate slotted MRRs with two different slot materials
- Analyse optical delay lines based on slotted MRRs and assess their performance

In order to meet these aims, the following milestones have been pursued:-

- Create UPML – MRTD
- Numerical assessment of the UPML-MRTD through comparison with results in literature
- Investigation of the performance of MRRs based on high-index-contrast waveguides
- Modelling the performance of SMRRs
- Suggest and demonstrate a novel design of optical delay lines based on SMRRs

All the work and results related to the accomplishment of the objectives stated above will be discussed in detail in the next chapters of this thesis

1.6 Outline of the Thesis

Since the initial proposal of microcavity ring resonator [26], both analytical and numerical techniques have been adopted. With their unique properties and the potential to significantly build up a higher field from a weaker input field, MRRs may find applications in many fields of science and engineering. This thesis brings MRRs into higher numerical precision realm that can not be predicted analytically to provide a full framework to understand and explain the light propagation in MRRs and to optimise the device performance before fabrications.

Chapter 2 the features of optical microcavity ring resonators in wavelength division multiplexing are described and their many benefits explained. This covers all the necessary general concepts and relevant basic theory which are all well established in literature. The optical properties of MRRs are gradually analysed – starting with a form of single microring resonator that is useful for understanding their properties such as the power exchange phenomena. Also, the electromagnetic derivations based on the single ring resonator can be extended and applied in the analysis of more complex structures including the two rings configuration.

In chapter 3, MRTD technique has been proposed for the first time for analysis of MRRs. The MRTD method relies on applying multiresolution analysis in context of method-of-moments to discretise Maxwell's equations where electromagnetic computational field components are expressed as weighted sums of specific scaling and wavelet functions in space and time domain. This scheme has proven in literature to be highly accurate compared to the more used FDTD method which strongly suffers from numerical dispersion at fixed resolution in space.

In chapter 4, several examples have been analysed in order to assess the Uniaxial Perfectly Matched Layer for the MRTD in the context of optical slab waveguide as well as MRRs.

Chapter 5 presents MRR based on high-index-contrast waveguide. The effect of the structure geometry parameters such as the gap between the ring and input/ output waveguides, the ring radius., and the width of the input/output and the ring resonators is thoroughly investigated.

In chapter 6, an accurate analysis of two-dimensional coupled microring resonators based on high-index-contrast waveguide is carried out. The normalised transmission spectra for a single-ring and double ring configurations have been investigated by using robust and accurate MRTD technique in conjunction with UPML absorbing boundary condition the rigorously terminate the computational window. Two different configurations are considered in this chapter, single-ring resonator, and double-ring resonator in parallel. The major physical characteristics of the waveguide-coupled MRR have been numerically investigated, including the resonance wavelength, the free spectral range, the coupling and rejection ratio, and the resonance-mode quality factor.

Slotted microcavity ring resonators are analysed in chapter 7. The performance of these devices in terms of coupling efficiency and normalised transmission spectra has been accurately investigated by means of MRTD technique in conjunction with UPML absorbing boundary conditions that rigorously terminate the computational window. Two different slot filling materials, air and SiO_2, are considered for comparison. The variation of coupling efficiency and quality factor with the slot design specifications, such as position and width of the slot, has been thoroughly investigated.

In chapter 8, a novel design of coupled-resonator optical waveguide delay line based on slotted ring resonator (SCROW) is proposed and analysed. Coupling efficiency can be reduced to control both group velocity and delay time by changing the geometry of the bent slotted waveguide which strongly affects the properties of the propagation modes. The coupling efficiency between the multiple coupled resonators plays an essential role in the determination of the SCROW performance and can be controlled by changing the effective refractive index of the ring. Due to the presence of curved materials interference and greatly different length scale linked with the sub-wavelength sized slots and the waveguide-resonators coupling region, this typical system offers important challenges to both direct numerical solution and semi-analytical methods. The simulations are carried out using MRTD scheme in conjunction with UPML boundary conditions that rigorously truncate the computational window.

Finally, in chapter 9, conclusions and final remarks of the present research are drawn, and a view of the potential future topics is given.

Chapter 2

Background of Optical Microcavity Ring Resonators (MRRs)

2.1 Introduction

Microcavity resonators based on Whispering-Gallery-Modes (WGMs) play a significant role in many applications ranging from quantum electrodynamics to telecommunication devices and optical sensors [101]. In recent years, research has dedicated great attention to optical microcavity ring resonators. This is due to their attractive features of compactness and functionality. Consequently, they hold promise for future modern Wavelength Division Multiplexing (WDM). This chapter gives rigorous overview of the microring resonators and their properties. The chapter covers some essential background theory, and applications, which in turn shed light on the versatile of such structures.

2.2 Microring Resonators Based WDM

2.2.1 Overview of WDM

The optical fibre in optical communication networks has significant bandwidth which, unless exploited properly, would be exhausted on a signal channel being sent via the fibre. This is where optical WDM can be practical [35]. According to the different wavelengths (colours) of laser light, this technique is based on dividing the light in the optical fibre into distinctive channels. Each channel conveys the same amount of data as a single fibre that has not been overlapped. The basic idea behind of optical WDM can be illustrated in figure 2.1.

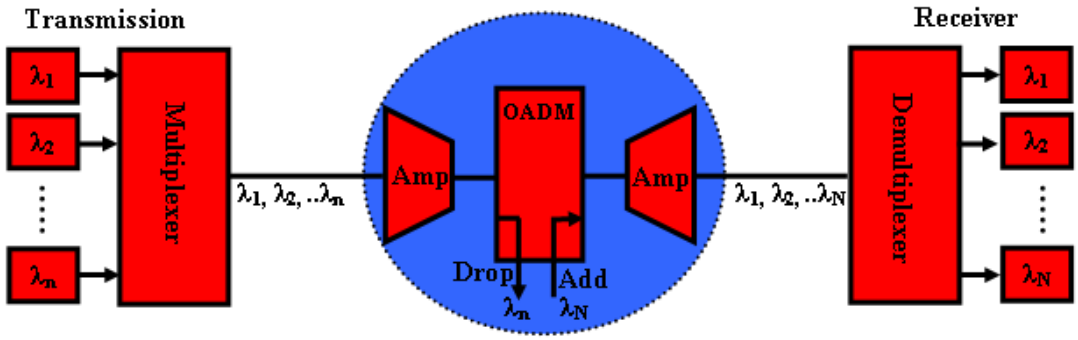

Figure 2.1 Simplified point-to-point WDM transmission system with amplifiers

Transmitters, multiplexer, optical fibre link with perhaps amplifiers, and demultiplexers are basic connection components in point to point WDM. For extra nodes in the middle of WDM, optical add-drop multiplexers (OADM) are required. At the transmitter side a WDM multiplexer combines a number of different signals to a single optical fibre. While at the OADM, specific wavelength can be dropped and another one with new data can be added. The signals reaching at the demultiplexer will be split and directed to one of the *N* receivers. Ideally, such a system would have a switching device that simultaneously broadcasts and receives signals. In telecommunication, the key advantage of WDM is its capability to increase the capacity of the network without changing its backbone. This is often done by employing filtering devices and deploying optical amplifiers all over the optical network [81].

2.2.2 Optical Microcavity Ring Resonators in WDM

Integrated optical filter in WDM system can be used as (de)multiplexer and add-drop components. In general, there are different types of devices that can be employed as add-drop filter and (de)multiplexer. This is including the Arrayed Waveguide Grating

(AWG), Bragg gratings, and thin films filters [70]. However, more often than not these devices are bulky and relatively hard to be incorporated in compact devices with multi functionality. Recent advances in micro and nano system technology have brought a new interest in building optical devices with physical dimension comparable to optical wavelength [10]. In particular, integrated optical filters based on microcavity ring resonators can become as small as 10^{-4} cm and can be promising candidates in the future of VLSI photonics.

Low-index-contrast and high-index-contrast are two classes of microring resonator devices that can be utilised in WDM applications. The conventional low-index-contrast resonators have the advantage of showing low propagation loss [10]. On the other hand, since a very large bend radius is required to achieve a high efficiency bend, resonators based on such waveguides involve a very large radius for the design of the circular waveguide which build the ring. As a result, the overall size of the ring resonator is increased while the Free Spectral Range (FSR) which is inversely proportional to the diameter of the ring is limited [10]. Research efforts have been directed towards designing new structures to achieve a wide FSR without decreasing the diameter of the ring. Different approaches in literature include double-ring and triple-ring resonators [10, 51, 94]. Thanks to the recent advances in material technology and fabrication techniques, microring devices with physical dimension comparable to optical wavelength have been made possible to be fabricated with negligible bending loss [10]. The requirements of achieving higher performance for the future of optical communication devices, as well as computing and signal processing devices to complement or competitively replace their microelectronic counterparts in integrated

circuits, make it essential that novel optical microstructures be explored. High FSR, high extinction ratio, small size, and selectivity of coupling to the output ports are considered as figure of merits defining the good performance of these kinds of structures [10].

2.3 Microcavity Ring Resonators Devices

2.3.1 MRRs Shape

MRRs are a ring-shaped waveguide evanescently coupled at particular points vertically or horizontally to one or two straight waveguides as shown in figure 2.2.

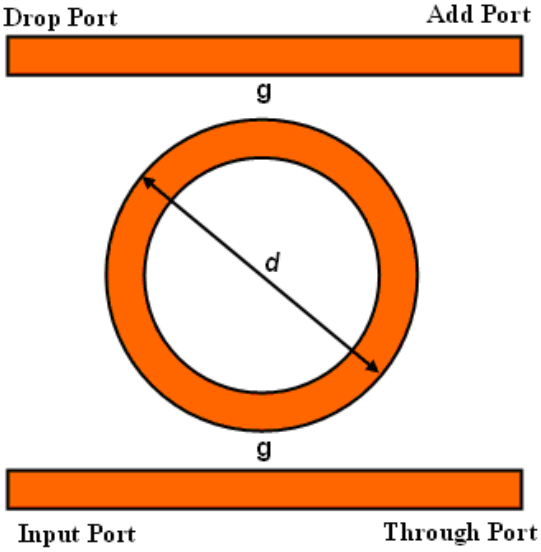

Figure 2.2 Schematic drawing of a microcavity ring resonator

At particular wavelengths, the amount of power coupled to and from the ring can be determined by either the effective index of the waveguide, the distance between the waveguides, or the length of the ring. If, for a given frequency, the optical length of the ring is equivalent to a multiple of the frequency then constructive interference takes

place and light can be stored in the cavity and as a result the waveguide transmission will be decreased [81, 97].

The shape of the MRRs is basically not constrained to circle. The racetrack is another optical resonator geometry [80] which is shown in figure 2.3.

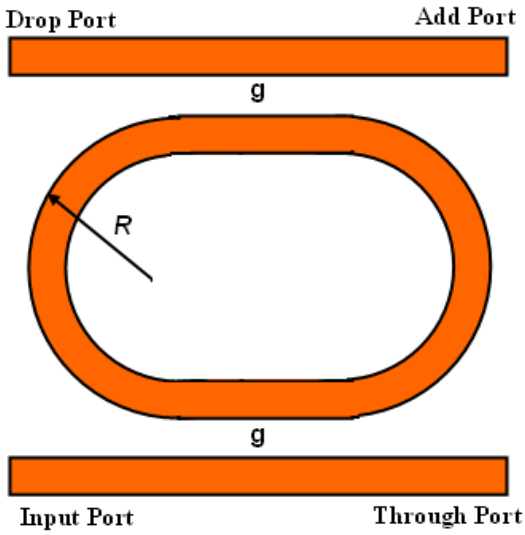

Figure 2.3 Schematic diagram of racetrack resonator

Due to the long and straight coupling path, the coupling between semi-circle resonator and the straight bus waveguide can be controlled allowing longer interaction length which in turn not only reduces the coupling loss but also permits the enlargements of the distance between the semi-circle resonator and the straight bus waveguide. However, they are counterbalanced with some drawbacks of introducing transition losses at the transition between the curved and straight portions. In addition, due to longer coupling length, FSR will be reduced [57].

An additional common configuration is illustrated in figure 2.4, is known as the disk resonator [86].

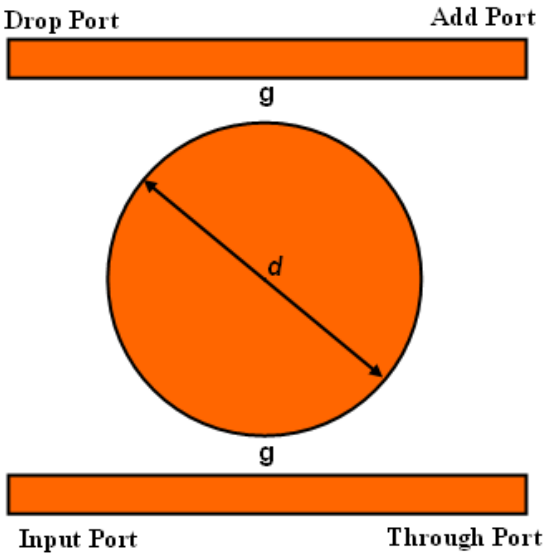

Figure 2.4 Schematic diagram of disk resonator

Although higher lateral contrast can be achieved compared to the circular resonators, thus lower losses can be gained, potentially high order modes can be arisen.

2.3.2 Coupling Scheme of MRRs

Lateral and vertical coupling scheme are mainly two approaches in which the light can be coupled from the input waveguide to the ring and from the ring to the output waveguide. This section is devoted to discussing these two schemes in details.

2.3.2.1 The lateral Coupling Scheme

When the input and output bus waveguides are situated in the same plane with ring, the coupling between the waveguides takes place horizontally, this is recognised as lateral coupling as shown in figure 2.5.

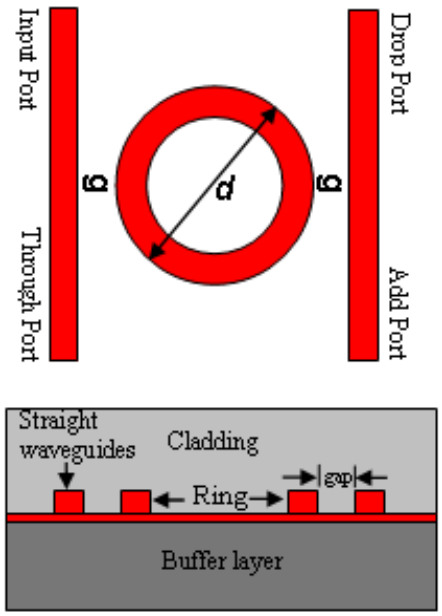

Figure 2.5 Schematic layout of single microcavity ring resonator in top view and cross-section; lateral coupling

The coupling efficiency can be controlled by the etched gap between the input/output waveguide and the ring [86, 12]. As the strength of the coupling extremely depends on the distance between the input/output waveguide and the ring, this scheme is very sensitive to the lithography and engraves procedures that construct the gap. For high-index-contrast structures, as semiconductors, the gap size requires to be in the range of 100 nm in order to achieve a considerable coupling, for this reason, e-beam lithography is necessary.

2.3.2.2 The vertical Coupling Scheme

This configuration is based on placing the input and output bus waveguides either on top or bottom of the ring as illustrated in figure 2.6, where the coupling between the waveguides occurs vertically; this is known as vertical coupling scheme.

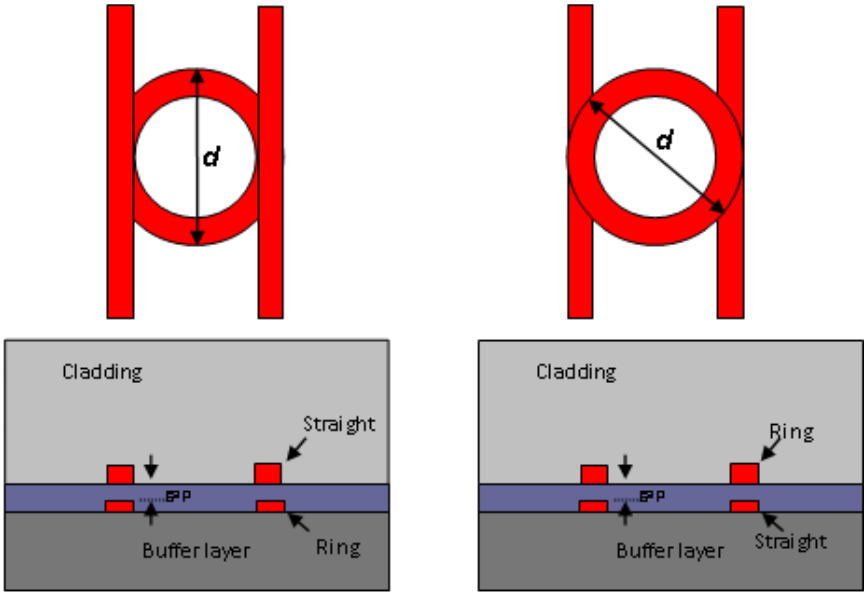

Figure 2.6 Schematic layout of single microcavity ring resonator in top view and cross-section; vertical coupling

Although this scheme presents superior coupling efficiency owing to larger region under interaction, it is harder to fabricate. This is because of the input and output waveguides are placed in different levels [55]. In this case, the coupling strength is calculated by the thickness of the layer between the ring and waveguides.

2.4 Cascaded Multiple Microcavity Ring Resonator Devices

Optical microcavity ring resonators can be made of either single or multiple resonators. Figure 2.2 shows a configuration of horizontal coupling single ring resonator. This kind of device has shown promising functionality in all-optical PLCs such as delay signal devices. A specifically tailored delay line response with an increased performance as required in applications such as synchronisation can be achieved by cascading multiple microcavity ring resonators and selecting appropriate parameters.

Serial and parallel are two configurations in which multiple ring resonators can be arranged. In the following section, both arrangements will be explained.

2.4.1 Serial Configuration

The schematic diagram of multiple cascaded resonators in serial configuration, known as Coupled Resonator Optical Waveguides (CROWs), is illustrated in figure 2.7.

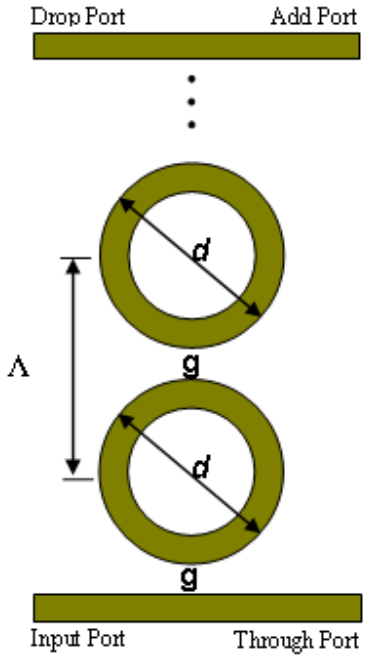

Figure 2.7 Schematic diagram of multiple cascaded resonators in serial configuration

The key point is that a number of coupled resonators are placed between two straight bus waveguides acting as input and output ports. The coupling between the input and output waveguides and the ring as well as between the rings takes place by means of directional couplers with coupling efficiency, κ. The microring radius and separation distance are indicated by *d* and *g* respectively [24].

Referring to figure2.7, the light in this manner can be exited through the input port

where part of it, on-resonance case, couples into the first ring and starts to travel along the ring. After one round trip inside the cavity constructive interference occurs with the light that has just joined to the ring leading to coherent build up within the ring. After that, a substantial portion of power will be coupled to the neighbour ring and carry on until is coupled ultimately to the drop port. In this case, all the rings required to be resonate at the same wavelengths. Therefore, an accurate control in terms of fabrication process is extremely needed to ensure identical interactions between the nearest neighbour cavities. At off-resonance, the portion of light remains uncoupled and keeps propagating along the input waveguide where it can be detected at through port [24].

2.4.2 Parallel Configuration

Figure 2.8 shows the schematic layout of parallel multiple ring resonators configuration, also known as Side Coupled Integrated Spaced Sequence of Resonators (SCISSORs).

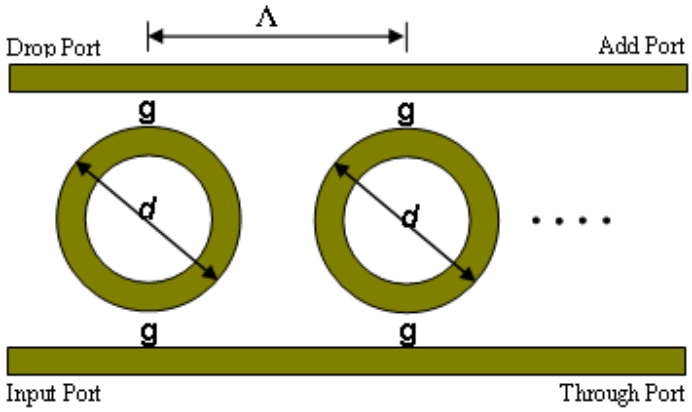

Figure 2.8 Schematic diagram of multiple cascaded resonators in parallel configuration

As shown in figure 2.8, the ring are arranged in such a way there is no straight coupling between them, but they are indirectly coupled via the bus waveguide. Thus, the light can

travels within unique direction preventing from counter propagation. This kind of configuration is found to be more flexible in terms of fabrication process than serial one. On the other hands, due to the possibility of phase changing in the connecting length, Λ between the rings which optimised only for narrow wavelength range, the useful wavelength range of these rings is limited [24]. Exceeding this range could lead the output at drop port to be largely varied in unforeseen way owing to interference of light coupled from each individual resonator.

The coupling between each ring and the straight bus waveguide is taken place by means of directional coupler. Since each resonator is characterised by the following parameters: ring diameter, the gap distance between the rings and bus waveguides, and the distance of centre to centre between the nearest neighbour rings that needs to be carefully chosen in order to achieve the required interference at the specific wavelength range [24].

2.5 Microcavity Ring Resonators Applications

Over the last decades, optical microcavity ring resonators have attracted a great attention in the scientific community. Since then, they found their way in a wide range of applications. This section highlights some of these applications.

2.5.1 Dispersion Compensation

Optical ring resonator can be used as flexible dispersion compensation components in WDM [16, 32]. Figure 2.9 shows the block diagram of multistage dispersion compensator using microcavity ring resonator.

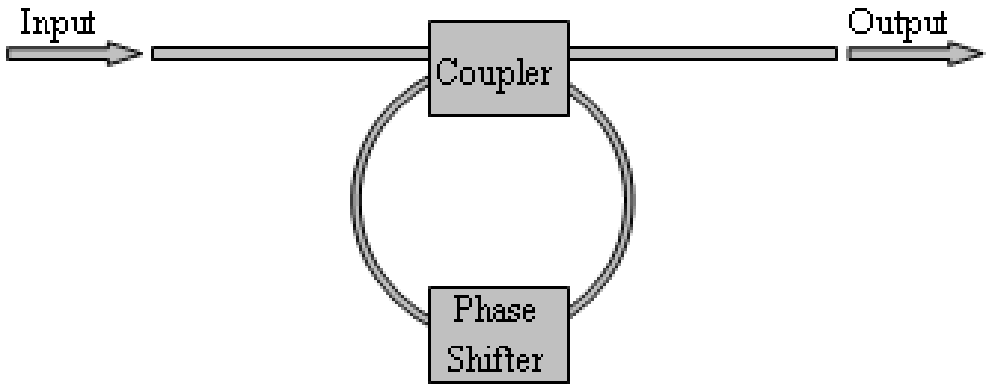

Figure 2.9 Schematic diagram of microcavity ring resonator as multistage dispersion compensator

The variation in the group velocity of light propagating along optical fibre with alters in optical wavelengths can leads to chromatic dispersion.

A spectrum of wavelengths are associated within any data pulse propagates along optical fibre, in this manner, the shorter wavelength components are likely to be travelled faster than the ones with longer wavelength components. This leads to broadening the pulse and consequently, interference takes place with neighbouring pulses which cause distort the transmitted signal. In this case, practical dispersion components that can limit tenability and have uniform insertion loss upon tuning of dispersion and multiple wavelength operation are extremely required. Optical microcavity ring resonators have the ability to augment the physical length by means of forcing the light to pass through the physical distance many times.

2.5.2 Notch Filters and (de) mulitplexers

By means of strategic coupled of microring and Mach-Zehnder interferometer as in figure 2.10, it has been possible to design many optical devices in a very easy and compact way.

Examples include notch filters [76], and a periodic (de)multiplexer [67].

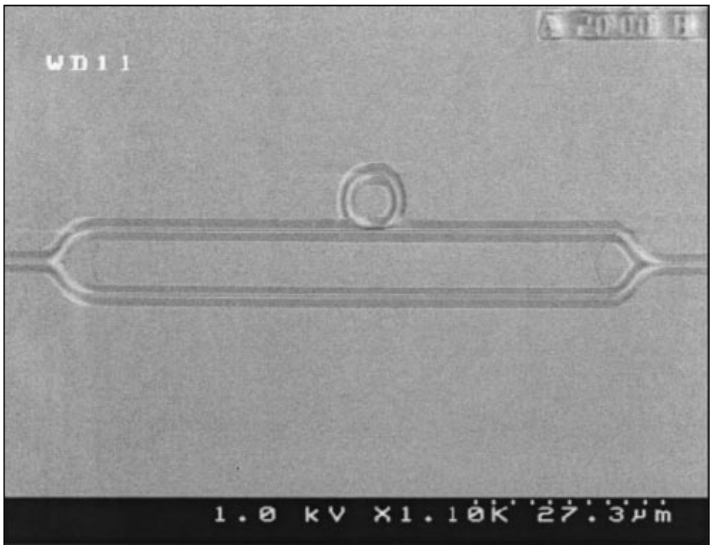

Figure 2.10 Schematic diagram of microcavity ring resonator coupled to one arm of a Mach-Zehnder interferometer [76]

2.5.3 Add-Drop Filters

It has been possible to design add-drop filters based on microcavity ring resonator using either double or triple ring resonators integrated with Semiconductor Optical Amplifiers (SOAs) for the flexible use of WDM channel in wavelength division multiplexing networks [23]. The schematic diagram of add-drop filter is shown in figure 2.11.

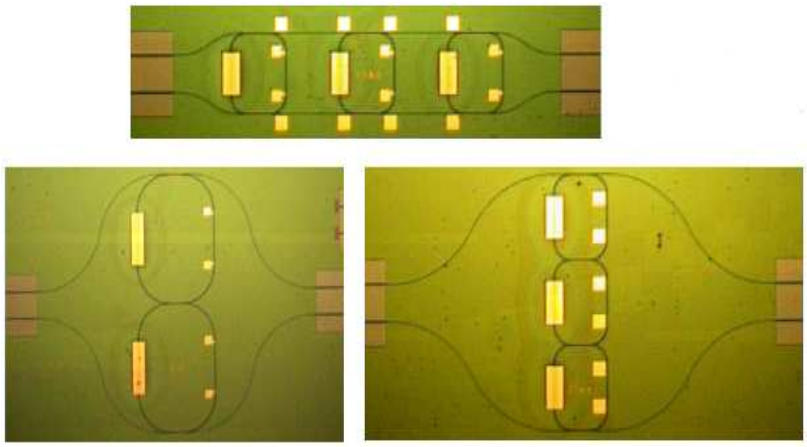

Figure 2.11 Schematic diagram of add-drop filters integrated with SOA using MRRs [23]

2.5.4 Millimetre Wave Generation

The use of soliton pulse propagates within system of optical microcavity ring resonator can leads to a new design of a simultaneous short-wave and millimetre-wave generation [90].

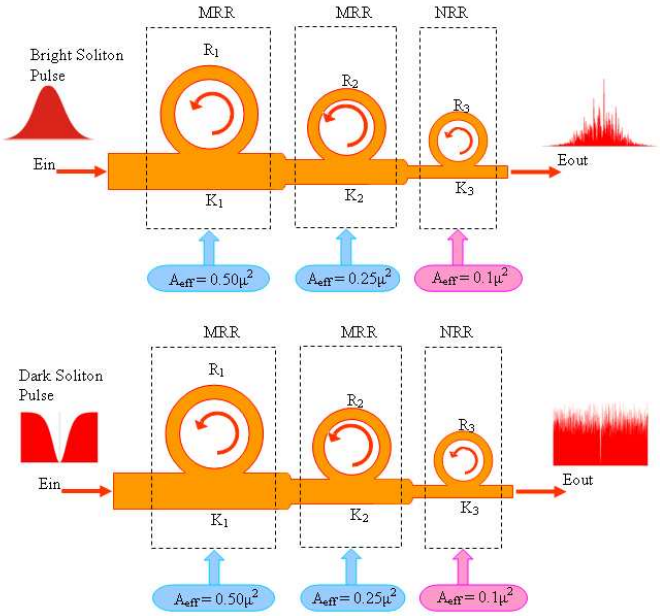

Figure 2.12 Schematic diagram of cascaded ring resonators used for generation of mm-wave signals [90]

By means of suitable parameters such as input soliton power, coupling coefficients, and ring radii, a novel system of micro and nano ring resonators can be designed in such way that can generate broad bandwidth [90]. A similar configuration can also be used for chaotic communication [77].

2.5.5 Biosensors

Optical microcavity ring resonators have found their way even in biology applications as biosensors [21]. The design principle of this device is based on monitoring the change in transfer characteristics of the microring cavity when biological materials drop on top of the ring resonator.

2.5.6 Optical Logic Gates

Photonic logic gates are vital components for realising optical signal processing and computing systems. In this regard, optical microcavity ring resonators have been found to be possible candidates for the realisation of photonic logic gates such as NOR gate [101] and ultra fast all-optical AND logic gate [89].

2.5.7 Optical Delay Lines

The slow light can play an important role for applications where the dynamic control of the delay is needed for synchronisation purposes, multiplexing, and data storage [8]. In this context, optical microcavity ring resonators is one of the most important building block for more complicated nano-waveguide based structures which can support slow light operations [30, 71, 3, 4].

These are only some of the applications which can be realised with microcavity ring resonators. The following section presents the operation principles of microcavity ring resonators.

2.6 Microcavity Ring Resonators: Theory and Operation Principles

Circular integrated optical micocavity ring resonators are increasingly utilised as compact and versatile wavelength filters. The resonators are functionally represented in terms of one or two directional couplers with suitable connection using bent and straight bus waveguides. This section is dedicated to discuss add-drop model of microavity ring resonators.

2.6.1 Add-Drop MRRs Theory

The typical layout of the add-drop microcavity ring resonator is shown in figure 2.13. It consists of ring waveguide and two bus waveguides.

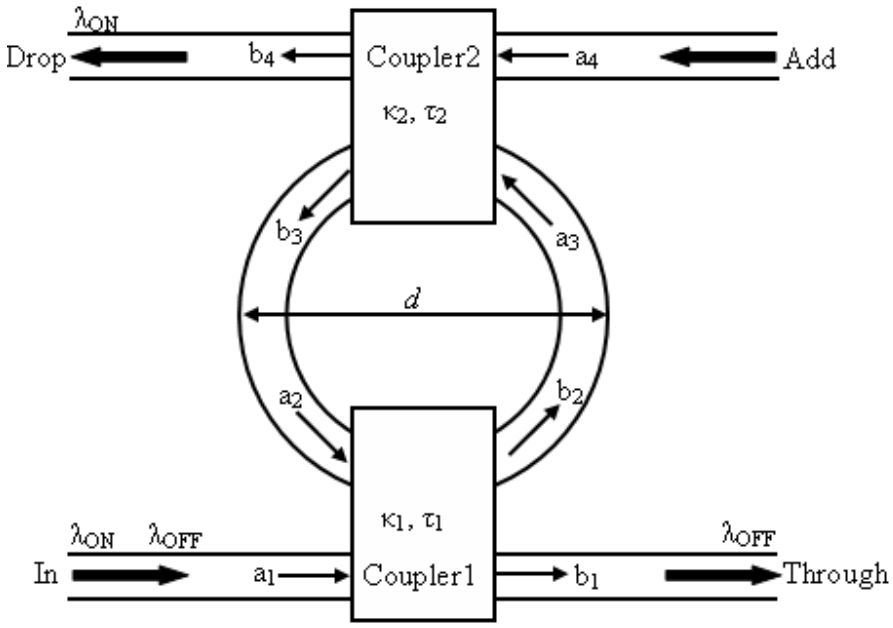

Figure 2.13 Schematic diagram of add-drop microcavity ring resonator

Similar to any resonator, the working principles of this kind of resonator is based on the following main quantities, firstly the coupling efficiency, which determine the amount

of power coupled to/from the ring, secondly the propagation losses, which have an effect on the quality of the resonator, ultimately, the roundtrip phase, which determines the resonance condition.

The structure in figure 2.13 is designed to drop an optical signal at drop port if proper phase matching conditions exist [21].

$$n_{eff} \quad \pi \quad d = m \quad \lambda \tag{2.1}$$

where λ is the signal wavelength inside the medium, n_{eff} is the effective refractive index of the medium, *d* is the ring radius, *m* is an integer.

When a defined spectral range is injected as a source, the frequencies that can resonate inside the ring are coupled to the second waveguide (on-resonance case) via the ring, while the others, for which the relation (2.1) is not satisfied, carry on propagating inside the first waveguide and can be found at through port (off-resonance case). After one roundtrip the field inside the ring is decreased by $\sigma = e^{-\alpha L/2}$, where α is the propagation loss inside the ring. The coupling of the field between the input bus waveguide and the ring, and between the ring and output bus waveguide can be explained by means of the coefficients κ_i and τ_i. As it is illustrated in figure 2.13, κ_i is the amplitude coupling coefficients, while τ_i is the amplitude transmission coefficients across the coupling region [11, 44]. Assuming lossless coupling, the relation $\kappa_i + \tau_i = 1$ holds. Using these definitions, the intensity at through port can be expressed by:

$$I_{Through} = \left|\frac{b_1}{a_1}\right|^2 = \frac{\tau_1^2 - 2\sigma\tau_1\tau_2\cos(\varphi) + \sigma^2\tau_2^2}{1 - 2\sigma\tau_1\tau_2\cos(\varphi) + \sigma^2\tau_1^2\tau_2^2} \tag{2.2}$$

The intensity at the drop port is proportional to the intensity inside the ring at second coupling region:

$$I_{Drop} = \left|\frac{b_4}{a_1}\right|^2 = \sigma \kappa_2^2 I_{Ring} \tag{2.3}$$

where

$$I_{Ring} = \left|\frac{b_2}{a_1}\right|^2 = \frac{\kappa_1^2}{1 - 2\sigma\tau_1\tau_2 \cos(\varphi) + \sigma^2\tau_1^2\tau_2^2} \tag{2.4}$$

2.6.2 Add-Drop MRRs Performance Parameters

The design consideration is based on taking into account the performance of the ring. Thus, several parameters are significant in the description of resonators, this including the free spectral range, the spectral width, the quality factor, and the finesse. This section is devoted to discuss these terms that qualify the performance of the microcavity ring resonator.

According to Equation 2.2, the typical transmission spectrum of add-drop microcavity ring resonator is shown in figure 2.14.

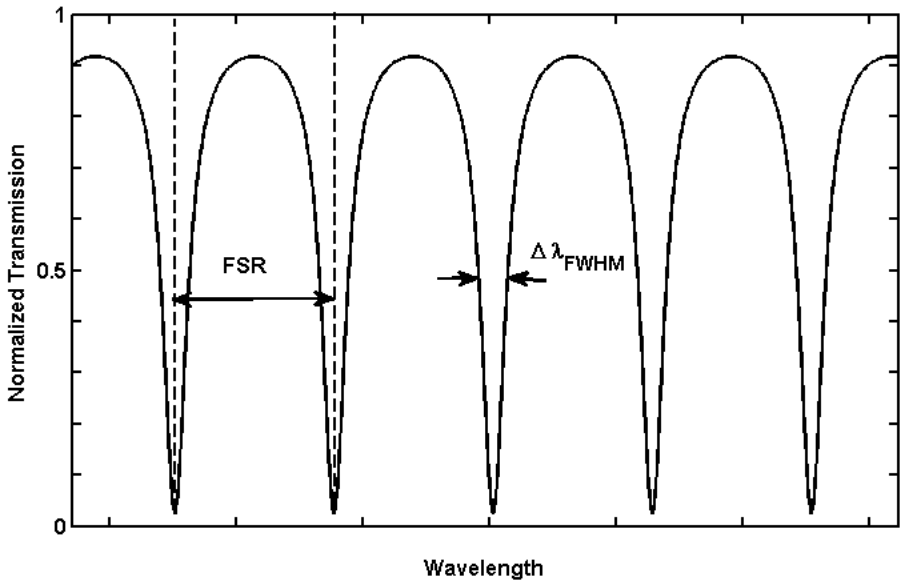

Figure 2.14 Typical transmission characteristics of microcavity ring resonator at through port

At precise wavelength values, an essential property of optical microcavity ring resonator can be stemmed from this size-dependent spectrum. The following quantities can be commonly used to describe the microcavity ring resonator behaviour.

2.6.2.1 Free Spectral Range

A parameter that is inversely proportional to the resonator diameter is the FSR. It is defined as the spacing between two adjacent resonant wavelengths. By differentiating the equation 2.1 with respect to the wavelength, the FSR can be expressed as [24]

$$FSR = \lambda_{m+1} - \lambda_m = \frac{\lambda^2}{\pi d n_g} \tag{2.5}$$

where the group effective index, n_g which contains the material dispersion can be defined as

$$n_g = n_{eff} - \lambda \frac{\partial n_{eff}}{\partial \lambda} \tag{2.6}$$

It is obvious from equation 2.5 that the ring diameter is basically having an effect on the FSR, where large FSR requires small resonator. For example, A ring diameter of 5μm ($n_{eff} \cong 3$) implies FSR=50 nm.

2.6.2.2 The Spectral Width

The spectral width determines how fast optical data can be processed by microcavity ring resonator and can be defined as the full width at half maximum (FWHM) of the transmission spectrum peak as shown in figure 2.14. Using equation 2.3 for drop port, the intensity can be written as [24].

$$\frac{\sigma \kappa_2^2 \kappa_1^2}{1 - 2\sigma \tau_1 \tau_2 \cos(\varphi) + \sigma^2 \tau_1^2 \tau_2^2} = \frac{0.5\ \sigma \kappa_2^2 \kappa_1^2}{1 - 2\sigma \tau_1 \tau_2 + \sigma^2 \tau_1^2 \tau_2^2} \tag{2.7}$$

where

$$\varphi = \Delta \omega \frac{\tau_R}{2} \tag{2.8}$$

Equation 2.7 can be rewritten as

$$1 - 2\sigma \tau_1 \tau_2 \cos(\varphi) + \sigma^2 \tau_1^2 \tau_2^2 = 2\,(1 - 2\sigma \tau_1 \tau_2 + \sigma^2 \tau_1^2 \tau_2^2) \tag{2.9}$$

By means of Euler formula, for small φ, $\cos(\varphi) = 1 - (\varphi^2/2)$ thus

$$\varphi^2 = \frac{(1 - \sigma \tau_1 \tau_2)^2}{\sigma \tau_1 \tau_2} \tag{2.10}$$

Taking into account equation 2.8 and equation 2.10, considering symmetric coupling, and after mathematical manipulations the FWHM of wavelength is derived as

$$\Delta \lambda_{FWHM} = \frac{1 - \sigma \tau^2}{\sqrt{\sigma}\,\tau} \cdot \frac{FSR}{\pi} \tag{2.11}$$

It is obvious that the roundtrip loss and the coupling efficiency influence the FWHM.

2.6.2.3 The Quality Factor

The quality factor of the microcavity ring resonator gives details of the ratio of the energy stored in the resonator to the energy lost per one roundtrip [24]:

$$Q = \omega_0 \times \frac{stored\ \ power}{lost\ \ powe} \tag{2.12}$$

The quality factor is an important quantity for microcavity ring resonator that measures the sharpness of the resonance relatively to its central wavelength and can be analytically expressed in other way as [24].

$$Q = \frac{\lambda_m}{\Delta \lambda_{FWHM}} = \frac{\pi\ L\ n_g}{\lambda_m} \frac{\sqrt{\sigma}\,\tau}{1 - \sigma \tau^2} \tag{2.13}$$

2.6.2.4 The Finesse

The finesse can be defined as the ratio of FSR and $\Delta\lambda_{FWHM}$ and can be expressed as [24]

$$F = \frac{FSR}{\Delta \lambda_{FWHM}} = \frac{\pi \sqrt{\sigma}\,\tau}{1 - \sigma \tau^2} \tag{2.14}$$

This relation is very important to balance between the FSR which has to be preferably high and $\Delta\lambda_{FWHM}$ which has to be rather low to differentiate between the adjacent resonance peak and the shift in the working resonance peak. Thus, higher finesses mean better sensitivity and selectivity [55].

2.7 Summary

This chapter has covered the essential background theory of microcavity ring resonators. This included highlighting their capability to manipulate the flow of light. The operation principles was explained starting from brief overview of WDM followed by reviewing MRRs as WDM components, and then the applications of MRRs were presented. The phenomena of coupling and controlling the flow of light through MRRs structures were covered.

In order to successfully model and simulate these MRR structures, the MRTD numerical modelling method was used. This technique is presented in details in chapter three.

Chapter 3

Multiresolution Time Domain (MRTD)

3.1 Introduction

Since 2D MRRs have complicated structures and cannot be analysed using simple techniques, several numerical methods have been developed for such complicated electromagnetic structures. Therefore, this monograph presents techniques that can be used to model such complex structure in MRTD.

3.2 Background

Introduced for the first time by Krumpholz and Katehi in 1996 [68], MRTD is a known technique for the simulation of microwave devices in terms of mitigation of computational burden and low numerical dispersion [28, 62, 98]. Recently Letizia and Obayya [82] have successfully extended this technique for the accurate analysis of photonic devices for linear and nonlinear applications, proving to be a flexible, powerful tool for electromagnetic computation in optics.

The field expansion in space of MRTD is based on the Cohen-Daubechies-Feauveau (CDF) scaling basis function of order (2, 4) which being chosen from the family of biorthogonal interpolating functions, have proved to give good compromise between increased number of computations and improved accuracy [62, 98, 107]. Haar pulse functions are instead applied to the field expansion in time leading to a leapfrog scheme similar to the one used in FDTD. Furthermore, UPML scheme has been implemented at the boundaries to rigorously terminate the computational domain. Being time domain technique, it is capable of obtaining a wide range of frequencies with one simulation using Fast Fourier Transform (FFT) post-processing of the temporal data. In particular, for problems involving complicated structures such as MRR that cannot be analysed

using simple techniques, the complicated electromagnetic structures are more efficiently modelled numerically in time-domain instead of those operate in frequency-domain. Hence, this research is mainly concerned with the time-domain computational techniques and specifically the MRTD.

The MRTD algorithm is used as a computer code that is developed and enhanced to analyse the propagation characteristics of MRR structures. The following section provides a detailed review of the MRTD.

3.3 Multiresolution Fundamentals

3.3.1 MRTD Analysis overview

The MRTD method was introduced in [68] in which the basis of the MRTD technique for solving Maxwell's equations (see Appendix A) in time-domain on space grid was explained. Their technique relies on using wavelet expansion followed by Method-of-Moments (described in Appendix B) as a new way to increase both accuracy and efficiency of numerical techniques for solving interaction of electromagnetic wave problems. The scheme that they initially proposed in [68] is proving to be flexible and capable of providing a general discretisation technique to be utilised with diverse kinds of wavelet basis. In a typical manner, the wavelet system used in MRTD is orthonormal not only with scaling function but also with mother wavelet. In this scheme, the scaling functions are used firstly to develop the mother function which in turn is used to generate all the other wavelet basis functions. Numerical accuracy of MRTD stems from the levels of wavelet resolution terms. Each level contains a set of functions that can be

added to the expansion in order to increase the accuracy of the discretisation. The scaling functions $\varphi_i(x)$ can be written as [74]

$$\varphi_i(x) = \varphi\left(\frac{x}{\Delta x} - i\right) \tag{3.1}$$

At the same time as a wavelet coefficient $\psi_{i,p}^r(x)$ is represented by

$$\psi_{i,p}^r(x) = 2^{r/2}\psi_0\left(2^{r/2}\left(\frac{x}{\Delta x} - i\right) - p\right) \tag{3.2}$$

where r is the wavelet resolution and p is an integer in the range [0, 2^r-1]. Each level of resolution r consists of 2^r wavelets that are offset in space by $\Delta x/2^r$.

The following relationships describe scaling functions and wavelet coefficients [74, 75]

$$\int \varphi_i(x)\varphi_j(x) = \delta_{i,j} \tag{3.3}$$

$$\int \varphi_i(x)\psi_{j,p}^r(x) = 0 \quad \forall i, j, r, p \tag{3.4}$$

$$\int \psi_{i,p}^r(x)\psi_{j,q}^s(x) = \delta_{i,j}\delta_{r,s}\delta_{p,q} \tag{3.5}$$

$$\delta_{i,j} = \begin{cases} 1 & i = j \\ 0 & i \neq j \end{cases} \tag{3.6}$$

From the space of square integrable functions $L^2(R)$, all wavelets of resolution r form a set of subspaces $\{V_i\}_{i\in Z}$ which fulfil the following properties [109]

$$\{0\} \subset \ldots \subset V_{-2} \subset V_{-1} \subset V_0 \subset V_1 \subset V_2 \subset \ldots \subset L^2(R) \tag{3.7}$$

That is $V_s \subset V_{s+1}$ for all s in Z (nested subspaces)

$$\lim_{s\to\infty} V_s = \overline{\bigcup_{i\in Z} V_i} \qquad \text{(dense in } L^2(R)\text{)} \tag{3.8}$$

$$\lim_{s\to-\infty} V_s = \overline{\bigcap_{i\in Z} V_i} = \{0\} \text{ (coarser to zero)} \tag{3.9}$$

where Z stands for the set of all integers.

The accuracy of MRTD scheme relies on either increasing or decreasing of the wavelet resolution.

3.3.2 MRTD Scheme

In order to develop a MRTD scheme to solve Maxwell's equations, the electric and magnetic fields have to be represented as expansion in scaling and wavelet functions in space and time and then to apply the MoM.

For the simplest case based on one-dimensional scheme, the expansion of each field component in scaling and wavelet functions with arbitrary order of resolution up to r_{max} is expressed as [74]

$$F_x(x) = \sum_{n,i} h_n(t)\left[{}_n F_i^{x,\varphi}\varphi_i(x) + \sum_{r=0}^{r_{\max}} \sum_{p=0}^{2^r-1} {}_n F_{i,r,p}^{x,\Psi} \Psi_{i,p}^{r}(x) \right] \tag{3.10}$$

where ${}_n F_i^{x,\varphi}$ and ${}_n F_{i,r,p}^{x,\psi}$ are the expansion coefficient which represents the magnitudes of the scaling and wavelet functions and i indicate the position in space along x-direction. It is obvious that the discretisation is carried out together in space and in time. In order to ensure the causality, pulse functions $h_n(t)$ are employed in time. These functions in actual fact, do not overlaps in representing a given time step and therefore a new event is independent of a past one.

For any wavelet basis utilised, the number of expansion coefficients for a given maximum resolution can be determined using the following formula [74]

$$\text{Number of coefficients} = 2^{D + \sum_{i=x,y,z} r_{\max,\, i}} \tag{3.11}$$

where D stands for the dimensionality of the system under investigation.

Once the number of basis functions has been determined using the above formula, the number of grid points can be also calculated [19]. Similar to Yee-FDTD scheme, the filed coefficients in [68] are misplaced by a half cell to construct a system in space.

Similar to FDTD, the new generated equations in MRTD are entirely explicit. Although the simplicity of implementation, time steps have to be selected under a stability limit, which is described in full detail in Appendix D. Particularly, discretisation in time relied on pulse functions brings to a leapfrog arrangement like the one in FDTD with *E* and *H* fields that are offset of half a time step. Once the field offset is chosen and by means of method of moments, the MRTD update scheme (covered in more details in Appendix C) is then obtained.

3.4 MRTD Based on Scaling Function

The accuracy and efficiency of the MRTD method and its ability to simulate a wide variety of devices for a large of frequency, from microwave to optical regime, have made this method one of the most popular in the research environment. MRTD is suggested as a good solution to the numerical dispersion and multi-grid problems associated with other numerical technique such as FDTD. The MRTD is employed by discretising the differential Maxwell's equation through method of moments, with the field expanded in terms of a family of wavelet and scaling functions. The employ of

variety levels of wavelet functions in addition to scaling function lead to a natural method of describing different levels of resolutions. Thus, the choices of the field expansion that produce a good approximation of the field play a crucial role in reducing the numerical dispersion error of the algorithm for a given grid discretisation.

This section is devoted to review the wavelet expansion and motivate the choice of the basic functions then details on the MRTD formulation will be presented.

3.4.1 Cohen-Daubechies-Feauveau based MRTD

The MRTD method has been demonstrated as an alternative solution to minimise the number of grid points without deteriorating the accuracy of the results. In other word, producing a better approximation of the field by means of accurate wavelet expansion can provides a good solution to the numerical dispersion error of the logarithm for a specified grid discretisation.

In terms of wavelet basis functions, a smooth one dimensional signal f can be approximated by [98]

$$f = \sum_{m=-\infty}^{\infty} \langle f, \phi_m \rangle \tilde{\phi}_m + \sum_{l=0}^{\infty} \sum_{m=-\infty}^{\infty} \langle f, \psi_{l,m} \rangle \tilde{\psi}_{l,m} \tag{3.12}$$

where ϕ_m , $\tilde{\phi}_m$ are the scaling function and its dual respectively, $\psi_{l,m}$, $\tilde{\psi}_{l,m}$ are the wavelet function and its dual respectively, m is the index representing the shift of scaling/wavelet function, and l is the index representing the scale of the wavelet function with shifts performed in increments of $1/2^l$.

To obtain an approximation for function *f*, the wavelet basis function has to satisfy the following properties:-

- Orthogonality, the scaling/wavelet functions satisfy the following relationships:

$$\begin{aligned} \left\langle \psi_{l,m}, \tilde{\psi}_{l',m'} \right\rangle &= \delta(l - l')\,\delta(m - m') \\ \left\langle \phi_m, \tilde{\phi}_{m'} \right\rangle &= \delta(m - m') \\ \left\langle \psi_{l,m}, \tilde{\phi}_{m'} \right\rangle &= \left\langle \phi_m, \tilde{\psi}_{l',m'} \right\rangle = 0 \end{aligned} \tag{3.13}$$

  If $\phi_m = \tilde{\phi}_{m'}$ and $\psi_{l,m} = \tilde{\psi}_{l',m'}$ the expansion will be orthonormal, otherwise it will be biorthogonal.

- Regularity (smoothness) which is the degree of the differentiability of the basis functions.

- Maximise number of vanishing moments where the k^{th} moment define by

$$m_1(k) = \int x^k \psi(x)\,dx \tag{3.14}$$

- Minimal support: the smaller the support of the wavelet is the less of the signal it picks up in a certain wavelet coefficient. For a certain number of vanishing moments, there is a minimum, nonzero period *(b−a)* of the support *(a, b)* of the mother wavelet.

The choice of any family of wavelet/scaling functions depends on fulfilling the above properties. The conventional Haar basis functions are one of the most popular scaling/wavelet family applied to MRTD scheme where algorithms comparable to Yee FDTD scheme can be created [31]. This kind of function holds the advantages of not only to preventing the overlap between the one cell and its neighbour due to their finite domain, but also the simplicity of carrying out derivative and integral calculations

owing to their pulse nature. However, their main drawback is the lack of smoothness that poses problems in terms of numerical dispersion contrasted to other existing wavelet families.

The MRTD technique that is based on Battle-Lemarie scaling/wavelet functions and derived from B-spline functions is proposed in [68]. Although they possess good regularity properties, they suffer from having unbounded support. This gives, theoretically, rise to an infinite number of MRTD terms in the update equations. Consequently, truncating of the sequence of MRTD coefficients to a rational number (more often than not 8-12 on each side) generates problems in terms of arithmetic precision that could vitiate the properties of the wavelet functions imposed by design [39].

By means of maximising the number of vanishing moments, compactly supported orthonormal wavelets have been achieved by Daubechies [106, 61]. Through this work, MRTD analysis based on Cohen-Daubechies-Feauveau (CDF) biorthogonal scaling functions is presented. It was found in literature that the use of this family of functions can fulfil well the requirements of MRTD scheme. Since for a given support, it demonstrates maximum number of vanishing moments.

Moreover, a good regularity, and compact support leading to an update equation involving a small number of proximate field components [98]. The notation CDF $(p, \bar{p})$ is adopted to indicate the lengths of the reconstruction and decomposition filters of the family. In this work, φ for the field expansions, has been selected of order (2, 4) from the CDF family. This order of functions is dependent on a total number of coefficients

equal to 5 (compact support) and demonstrates a good compromise between higher-order accuracy and increased number of operations needed.

An extensive investigation of numerical dispersion characteristics of CDF-MRTD contrasted to other wavelet families is carried out in [98]. Dogaru and Carin demonstrate that numerical dispersion relies on many factors for instance the Courant number, the spatial resolution, the number of level of wavelets used to expand the fields and the angle of electromagnetic propagation. On the other hand, it is found in general that MRTD technique permits a grid resolution at least twice coarser than FDTD when the same level of accuracy is needed.

Another significant aspect underscore is that dispersion performances are heavily influenced by the adopted Courant number. The selection for a Courant number smaller than the required limit for stability means better results in terms of numerical dispersion. As a result of this, when the same Courant number is taken, the low-order CDF(2,4) family can attain better accuracy than the case in which both scaling and first level of wavelet are included that implies a stricter stability limit on the time step size.

3.4.2 Derivation of scaling MRTD scheme

Starting from Maxwell's equations and for the two-dimensional problems in *x*-*z* plane, the transverse electric (TE) mode with components E_y, $H_x$and H_z is derived under assumption that *y*-axis is the homogenous direction and *x*-axis as propagation direction.

$$\frac{\partial H_x}{\partial t} = \frac{1}{\mu_0}\frac{\partial E_y}{\partial z} \tag{3.15}$$

$$\frac{\partial H_z}{\partial t} = -\frac{1}{\mu_0}\frac{\partial E_y}{\partial x} \tag{3.16}$$

$$\frac{\partial E_y}{\partial t} = \frac{1}{\varepsilon_0 \varepsilon_r}\left(\frac{\partial H_x}{\partial z} - \frac{\partial H_z}{\partial x}\right) \tag{3.17}$$

where μ0 is the permeability of the free space, and ε_r is the relative dielectric constant of the medium.

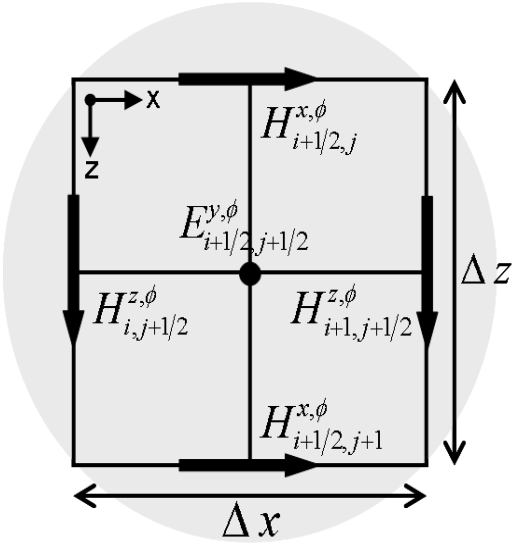

Figure 3.1 Electric and magnetic expansion coefficients as placed inside 2-D MRTD unit cell in the case of scaling functions (S-MRTD)

With respect to the unit cell shown in figure 3.1, the electromagnetic fields are expanded in terms of scaling functions in space and Haar functions in time as following:-

$$H_x(x,z,t) = \sum_{n,i,j=-\infty}^{+\infty} {}_nH^{x,\varphi}_{i+\frac{1}{2},j}\,\varphi_{i+\frac{1}{2}}(x)\varphi_j(z)h_n(t) \tag{3.18}$$

$$H_z(x,z,t) = \sum_{n,i,j=-\infty}^{+\infty} {}_nH^{z,\varphi}_{i,j+\frac{1}{2}}\,\varphi_i(x)\varphi_{j+\frac{1}{2}}(z)h_n(t) \tag{3.19}$$

$$E_y(x,z,t) = \sum_{n,i,j=-\infty}^{+\infty} {}_{n+\frac{1}{2}}E^{y,\varphi}_{i+\frac{1}{2},j+\frac{1}{2}}\varphi_{i+\frac{1}{2}}(x)\varphi_{j+\frac{1}{2}}(z)h_{n+\frac{1}{2}}(t) \tag{3.20}$$

where *n, i, j*, are the discrete indexes in time and in space respectively, φ is the scaling function chosen from the CDF(2,4) family, *h* is the Haar function and represents the sampling in time, and ${}_{n+\frac{1}{2}}E^{y,\varphi}_{i+\frac{1}{2},j+\frac{1}{2}}$, ${}_{n}H^{x,\varphi}_{i+\frac{1}{2},j}$, ${}_{n}H^{z,\varphi}_{i,j+\frac{1}{2}}$ are the expansion coefficients.

The discretisation in space follows a scheme that is very comparable to the Yee's system. As shown in figure 3.1, the components located in a cell, on which the update iteration takes place, are expansion coefficients. At the time step t_0 in a point (x_0, z_0), the actual field can be determined using

$$E_y(x_0, z_0, t_0) = \sum_{i',j'=-\infty}^{+\infty} {}_{n'}E^{y,\phi}_{i',j'}\varphi_{i'}(x_0)\varphi_{j'}(y_0) \tag{3.21}$$

where *i'*,*j'* and *n'* are the indexes in space and time respectively.

With recognition of the finite support of CDF scaling functions, only a few terms of the previous summation have to be considered.

Substituting the field expansion in the form of equations (3.18- 3.20) into the scalar Maxwell's equations and testing them with pulse functions in time and the dual of the biorthogonal scaling functions $\tilde{\varphi}_m$ (with *m*=*i, j*) in space, by applying the MoM, lead to the discretised update equation [82]

$${}_{n+1}H^{x,\varphi}_{i+\frac{1}{2},j} = {}_{n}H^{x,\varphi}_{i+\frac{1}{2},j} - \frac{\Delta t}{\mu_0 \Delta z}\left(\sum_{l=-L_s}^{L_s-1} a(l)\,{}_{n+\frac{1}{2}}E^{y,\varphi}_{i+\frac{1}{2},j-l-\frac{1}{2}}\right) \tag{3.22}$$

$${}_{n+1}H^{z,\varphi}_{i,j+\frac{1}{2}} = {}_{n}H^{z,\varphi}_{i,j+\frac{1}{2}} + \frac{\Delta t}{\mu_0 \Delta x}\left(\sum_{l=-L_s}^{L_s-1} a(l)\,{}_{n+\frac{1}{2}}E^{y,\varphi}_{i-l-\frac{1}{2},j+\frac{1}{2}}\right) \tag{3.23}$$

$$ {}_{n+\frac{1}{2}}E^{y,\varphi}_{i+\frac{1}{2},j+\frac{1}{2}} = {}_{n-\frac{1}{2}}E^{y,\varphi}_{i+\frac{1}{2},j+\frac{1}{2}} + \frac{\Delta t}{\varepsilon_0 \varepsilon_{i+\frac{1}{2},j+\frac{1}{2}}} \left(\sum_{l=-L_s}^{L_s-1} a(l) \left(-\frac{1}{\Delta z} {}_n H^{x,\varphi}_{i+\frac{1}{2},j+l+1} + \frac{1}{\Delta x} {}_n H^{z,\varphi}_{i+l+1,j+\frac{1}{2}} \right) \right) \tag{3.24} $$

where $\mu_{0,} \varepsilon_0$ are the permeability and permittivity of the free space respectively, ε is the relative dielectric constant of the medium, Δ_t is time step, and Δx , Δz are the spatial increments in the direction of *x* and *y* respectively.

The 'stencil size' L_s stand for the effective support of the basis function that determines the number of expansion coefficients in the summation and it is equal to 5 for CDF (2, 4), while *a(l)* represent the connection coefficients that can be numerically calculated using [98]

$$ \int_{-\infty}^{+\infty} \varphi_i(x) \frac{\partial \varphi_{i'+\frac{1}{2}}(x)}{\partial x} dx = \sum_{l=-L_s}^{L_s-1} a(l) \delta_{i+l,i'} \tag{3.25} $$

The value of the connection coefficients *a(l)* for the case of CDF (2, 4) are given in Table 3.1 [98].

Table 3.1 Connection Coefficients and Courant Number at the Stability Limit in Two Dimensions

l	**CDF(2,2)**	**CDF(2,4)**
1	1.2291667	1.2918134
2	-0.0937500	-0.1371348
3	0.0287617	0.0287617
4	0	-0.0034701
5	0	0.0000080
s	0.5300	0.4839

The CDF functions have the virtue of making use of finite number of nonzero coefficients in MRTD scheme (compact support), thus

$$a(l) = 0 \qquad \forall \quad l < -L_s \; and \quad l > L_s - 1 \tag{3.26}$$

$$a(-l) = -a(l-1) \qquad \forall \quad l < 0 \quad \text{(symmetry relation)} \tag{3.27}$$

Because of their Interpolation attribute as biorthogonal wavelets, the expansion coefficients for CDF families on which the updating take place can be considered as physical field value with insignificant error [98]. For example, at arbitrary point in space $(x_0 = i\Delta x, z_0 = j\Delta z)$ at time $t_0 = n\Delta t$, the field E_y is given by:-

$$E_y(x_0, z_0, t_0) = \iint E_y(x, z, t)\delta(x - x_0)\delta(z - z_0)\delta(t - t_0)dxdzdt = {}_nE_{i,j}^{y,\varphi} \tag{3.28}$$

Thus, this permits the field coefficients to be taken as actual field value and allows a simple simulation algorithm to be built in which the computational overhead of the whole reconstruction is saved.

A sketch of the update process in a 1D space is illustrated in Fig. 3.2. The component ${}_nE^{\varphi}$ at position i is computed from a number of components ${}_{n-\frac{1}{2}}H^{\varphi}$ in a range $[i+1/2-L_s; i-1/2+L_s]$ that is carried out by the stencil size L_s and are weighted by the connection coefficients $a(l)$.

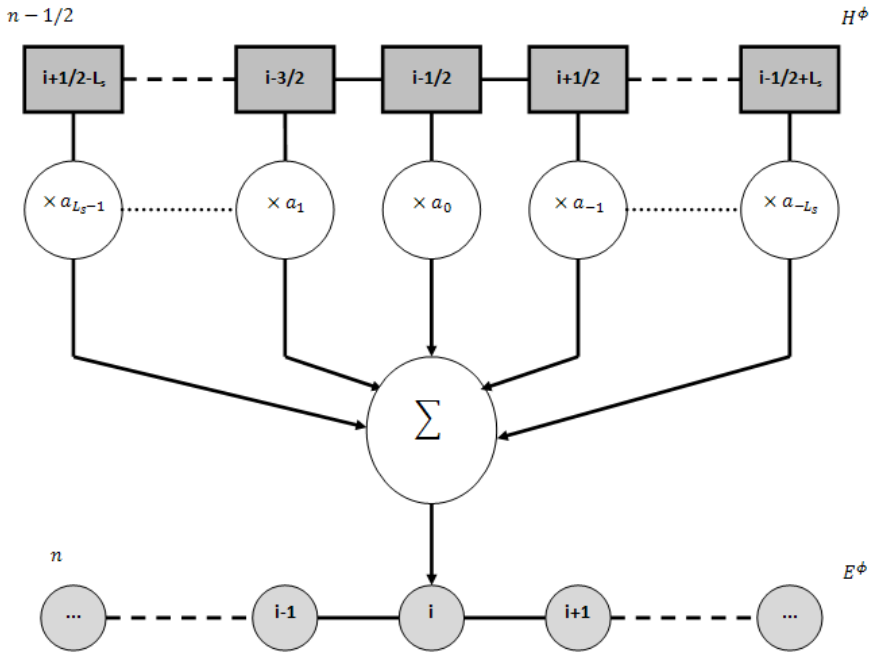

Figure 3.2 Scheme of the update process in a 1D space for S-MRTD with compact basis functions determined by the stencil size Ls

With the purpose of ensuring the numerical stability of the MRTD method (covered in more details in Appendix D), the time interval Δt has to be smaller than a certain limit as follows:-

$$\Delta t \leq s \frac{\Delta_r}{c_0}, \quad r = x \text{ or } y \tag{3.29}$$

$$s = \frac{1}{\sqrt{2}\sum_{l=0}^{L_s-1} |a(l)|} \tag{3.30}$$

where Δ is spatial step size in a uniform mesh, c_0 is the speed of the light.

The Courant number s represents the stability factor in two dimensions and is equal to 0.4839 for S-MRTD with CDF (2, 4), (Table 3.1). Numerical experiments revealed that

even though this value is enough to ensure the stability of the algorithm, it cannot guarantee a good accuracy of the results with coarser meshes. Smaller value of s, typically 5 times less the stability limit, can significantly improve the accuracy of the scheme even for coarser spatial step size.

In the spirit of the numerical comparison performed in [68], it has been found that the value s=0.1 is the most suitable to ensure not only numerical stability but also high level of accuracy.

3.4.3 UPML boundary condition in S-MRTD

The two dimensional S-MRTD scheme has been used in conjunction with the UPML scheme, first introduced by Gedney in 1996 [87], that rigorously truncates the computational domain. Starting from the traditional scalar equations of UPML reported in literature for FDTD [10, 87], they are now (see Appendix E), discretised by means of testing them with the scaling functions in space domain through Galerkin's method. Second-order central difference is adopted in time domain. It leads to a two-steps update scheme for each field component.

Considering the TE propagation and geometry of the grid (figure 3.2), the following discretised equations are obtained

$$ {}_{n}B^{x,\varphi}_{i+\frac{1}{2},j} = {}_{n-1}B^{x,\varphi}_{i+\frac{1}{2},j} - \Delta t \sum_{l=-L_s}^{L_s-1} a(l) \left(\frac{E^{y,\varphi}_{i+\frac{1}{2},j+l+\frac{1}{2}}}{\Delta z} \right)_{n-\frac{1}{2}} \tag{3.31} $$

$$ {}_{n}H^{x,\varphi}_{i+\frac{1}{2},j} = \left(\frac{2\varepsilon_0 - \sigma_z \Delta t}{2\varepsilon_0 + \sigma_z \Delta t} \right) {}_{n-1}H^{x,\varphi}_{i+\frac{1}{2},j} + \left(\frac{2\varepsilon_0 + \sigma_x \Delta t}{2\varepsilon_0 + \sigma_z \Delta t} \right) \frac{1}{\mu_0} {}_{n}B^{x,\varphi}_{i+\frac{1}{2},j} - \left(\frac{2\varepsilon_0 - \sigma_x \Delta t}{2\varepsilon_0 + \sigma_z \Delta t} \right) \frac{1}{\mu_0} {}_{n-1}B^{x,\varphi}_{i+\frac{1}{2},j} \tag{3.32} $$

$$ {}_{n}B^{z,\varphi}_{i,j+\frac{1}{2}} = \left(\frac{2\varepsilon_0 - \sigma_x \Delta t}{2\varepsilon_0 + \sigma_x \Delta t}\right) {}_{n-1}B^{z,\varphi}_{i,j+\frac{1}{2}} + \left(\frac{2\varepsilon_0 \Delta t}{2\varepsilon_0 + \sigma_x \Delta t}\right) \sum_{l=-L_s}^{L_s-1} a(l) \left(\frac{ {}_{n-\frac{1}{2}}E^{y,\varphi}_{i+l+\frac{1}{2},j+\frac{1}{2}}}{\Delta x} \right) \tag{3.33} $$

$$ {}_{n}H^{z,\varphi}_{i,j+\frac{1}{2}} = {}_{n-1}H^{z,\varphi}_{i,j+\frac{1}{2}} + \left(\frac{2\varepsilon_0 + \sigma_z \Delta t}{2\varepsilon_0}\right) \frac{1}{\mu_0} {}_{n}B^{z,\varphi}_{i,j+\frac{1}{2}} - \left(\frac{2\varepsilon_0 - \sigma_z \Delta t}{2\varepsilon_0}\right) \frac{1}{\mu_0} {}_{n-1}B^{z,\varphi}_{i,j+\frac{1}{2}} \tag{3.34} $$

$$ {}_{n+\frac{1}{2}}D^{y,\varphi}_{i+\frac{1}{2},j+\frac{1}{2}} = \left(\frac{2\varepsilon_0 - \sigma_z \Delta t}{2\varepsilon_0 + \sigma_z \Delta t}\right) {}_{n}D^{y,\varphi}_{i+\frac{1}{2},j+\frac{1}{2}} + \left(\frac{2\varepsilon_0 \Delta t}{2\varepsilon_0 + \sigma_z \Delta t}\right) \sum_{l=-L_s}^{L_s-1} a(l) \left(- \frac{ {}_{n}H^{x,\varphi}_{i+\frac{1}{2},j-l-1}}{\Delta z} + \frac{ {}_{n}H^{z,\varphi}_{i-l-1,j+\frac{1}{2}}}{\Delta x} \right) \tag{3.35} $$

$$ {}_{n+\frac{1}{2}}E^{y,\varphi}_{i+\frac{1}{2},j+\frac{1}{2}} = \left(\frac{2\varepsilon_0 - \sigma_x \Delta t}{2\varepsilon_0 + \sigma_x \Delta t}\right) {}_{n}E^{y,\varphi}_{i+\frac{1}{2},j+\frac{1}{2}} + \left(\frac{2\varepsilon_0}{\varepsilon_0 \varepsilon_{i+\frac{1}{2},j+\frac{1}{2}} (2\varepsilon_0 + \sigma_x \Delta t)} \right) \left({}_{n+\frac{1}{2}}D^{y,\varphi}_{i+\frac{1}{2},j+\frac{1}{2}} - {}_{n-\frac{1}{2}}D^{y,\varphi}_{i+\frac{1}{2},j+\frac{1}{2}} \right) \tag{3.36} $$

where ε is the permittivity of the medium, σ_x , σ_z are the electric conductivity of the UPML layers whose geometric grading profile takes the following form.

$$ \sigma_i(i) = \frac{\sigma_{\max} i^m}{d^m} \tag{3.37} $$

where i = *x, y,* d is the depth of the UPML, and *m* stands for the order of the polynomial variation. The selection of σ_{max} that minimises the reflection from boundaries is [99]

$$ \sigma_{\max} \approx \frac{(m+1)}{150 \pi \Delta \sqrt{\varepsilon_r}} \tag{3.38} $$

where Δ is the uniform spatial discretisation adopted.

3.5 Excitation Methods

3.5.1 Hard source and soft source

Two types of internal sources can be used with MRTD to excite the electromagnetic propagation inside the simulated structure: *hard source* and *soft source*. Setting up a

hard source means simply to assign the value of the *E*- or *H*- field at one or more MRTD grid points in space equal to a desired function of time. It becomes like the initial condition of an electromagnetic problem in which the *E*- or *H*- field is known at a point and the values of the radiated fields at the other grid points need to be calculated. Depending on how many points values are assigned in space, the source can be point wise or a plane wave. As an example, in a 1D system, with propagation in *x*-direction, a point wise hard source can be imposed as follows

$$E_z\big|_{i_{source}}^{n} = E_0 \sin\left(2\pi f_0 n \Delta t\right) \tag{3.39}$$

where a sinusoidal hard source (continuous wave, CW) E_z is assigned at the grid point i_{source} and it starts at the time step $n = 0$. As a result, the wave will propagate in both the directions back, $-x$, and forward, $+x$, from the starting point.

Another commonly used wave source is the low-pass Gaussian pulse that is centred in time at the step n_0 and has $1/e$ characteristic decay of a number n_{decay} of time steps

$$E_z\big|_{i_{source}}^{n} = E_0 e^{-\left(\frac{n-n_0}{n_{decay}}\right)^2} \sin\left(2\pi f_0 n \Delta t\right) \tag{3.40}$$

This function presents a finite direct current component and its Fast Fourier Transform (FFT) is centred at frequency f_0.

An important aspect of hard source condition is that for a source like the Gaussian, after a total simulation time greater than ($n_0 + n_{decay}$), the hard source acts as an electric mirror or Perfect Electric Conductor (PEC); the total tangential E-field is equal to zero.

Therefore, it cannot take into account the movement of reflected waves through the input section i_{source}. Also, in the case of a CW, when the tangential E-field value at the

excitation does not come to zero at a certain time, it is demonstrated that a spurious and nonphysical back-reflection of the waves toward the $+x$ direction of propagation is caused. This happens in any kind of imposed time function because at the source section a particular value of E-field is specified without considering in any way the effect of an incident field eventually occurring at the same section.

A way to avoid this effect can be to switch off the hard source after its time function has decayed to zero by replacing the equation at i_{source} with the standard FDTD update equations. However, this strategy can be adopted only in case of pulse wave forms that evolve in time only for a certain interval and not for continuous interacting sources such as a sinusoidal wave.

Alternatively, a soft source consists in the introduction of an electric current. It adds the value of the source time function at the FDTD current value of the field at the point i_{source}. As a result, the effect of the radiated propagating fields at the source interface will be considered and spurious reflections avoided. The soft source is imposed through the following

$$E_z\Big|_{i_{source}}^{n} = E_z\Big|_{i_{source}}^{n-1} + source\ \Big|^{n}, \quad \text{for every } n, \tag{3.41}$$

An existing problem with soft source is that it generates a nonzero DC component in the solution. This variation on the amplitude of the fields has to be considered in order to achieve correct results. A solution of this problem has been proposed by Furse *et al*., in 2000, [17]. It consists in applying a modified source function as

$$r(t)\sin(\omega t) \tag{3.42}$$

where *r(t)* represents a turn-on function defined by

$$r(t)=\begin{cases}0 & 0\le t\le \alpha T\\ 0.5\left[1-\cos\left(\dfrac{\omega t}{2\alpha}\right)\right] & t>\alpha T\\ 1 & \end{cases} \tag{3.43}$$

The soft-source technique has been utilized to deploy the source in the computational domain [66]. The soft-source technique relies on adding the value of the source at each computational domain point to the value of the electric filed at the same point; this is repeated for every time step. The effective index method was used to obtain the mode profile of the waveguide. In the TE-modes for guided modes the formulas are:-

$$E_y = E_c \exp\left[-\gamma_c(x-h)\right], h < x \quad \text{(cover)} \tag{3.44}$$

$$E_y = E_f \cos\left(k_{fx} - \phi_s\right), 0 < x < h \quad \text{(film)} \tag{3.45}$$

$$E_y = E_s \exp\left(\gamma_s x\right), x < 0 \quad \text{(substrate)} \tag{3.46}$$

where h is the core thickness[100]

3.6 Summary

This chapter has covered the essential numerical technique with its derivations, starting from the Maxwell's equations, looking at the multiresolution analysis, and the MRTD. Numerical dispersion and numerical stability constraints were discussed, and the appropriate choice of basic function in the form of the S-MRTD. Since this numerical method is applied to electromagnetic wave interaction in optical waveguides with infinitely extended computational domains, it is important to apply boundary conditions surrounding the computational domain to emulate free space in computer simulations. Ultimately, the source excitation techniques were categorised as hard and soft sources, and these sources were discussed.

In order to assess the performance of the suggested MRTD technique, optical slab waveguide and microcavity ring resonator are presented in chapter four as examples for numerical assessment of the developed technique.

Chapter 4

Numerical Assessment of Suggested MRTD

4.1 Introduction

This chapter makes extensive use of the literature review covered in the previous chapters. This is by applying the review and suggested technique in new designs and simulating these new designs. In order to demonstrate the ability of any numerical technique on modelling optical devices, it is of utmost importance to validate its accuracy. This chapter presents the work accomplished in studying the reflection coefficients from the UPML boundary in optical planar waveguide using MRTD. Also, the results of the simulations that study numerical convergence in the case of MRR based on high-index-contrast are presented.

All numerical simulations have been carried out using self built Compaq Visual Fortran code, Appendix F, in conjunction with MATLAB code, Appendix G, which is used to construct the structure and post-process the temporal data. Moreover, commercial software Full-Wave based on FDTD is used with a view to validate and test the accuracy of the developed MRTD.

4.2 Assessment of UPML-MRTD: test and code validation

4.2.1 Planar waveguide: As Numerical Assessment Example

The first model analysed is a two-dimension slab waveguide depicted in figure 4.1, with core and cladding refractive indices of n_{core} = 3.6, n_{clad} = 3.42 respectively. In order to ensure the single-mode propagation at 860 nm wavelength, the core width is selected to be w = 450nm. The structure is discretised into a uniform mesh with cell size $\Delta_x = \Delta_z = \Delta$ = 30 nm. In order to demonstrate the robustness of the UPML boundary condition incorporated into S-MRTD the structure is excited with a Gaussian pulse modulated in

time by a sinusoidal function with the shape of the fundamental mode profile of the waveguide as [82]

$$E_y(z,t) = E_0(z)\, e^{-((t-t_0)/T_0)^2} \sin(2\pi ft) \tag{4.1}$$

where $E_0(z)$ represents the fundamental mode profile of the waveguide, t_0 and T_0 are the time delay and the time width of the Gaussian pulse fixed at 60*fs* and 15*fs* respectively.

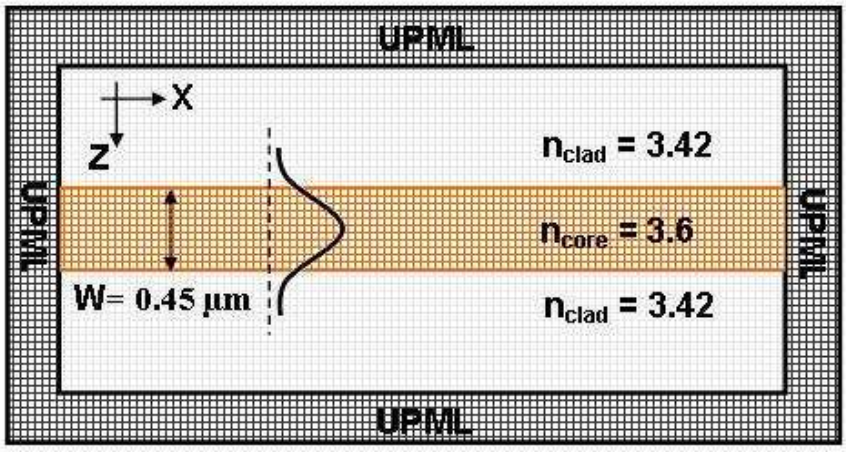

Figure 4.1 Configuration of planar waveguide of w = 0.45µm, n_{core} = 3.6, and n_{clad} = 3.42

As shown in figure 4.2, the filed profile represents a Gaussian pulse which is given by equation (4.1) and thus a stable field profile will propagate inside the waveguide and the time domain variation of incident, and reflected fields are recorded at the reference point.

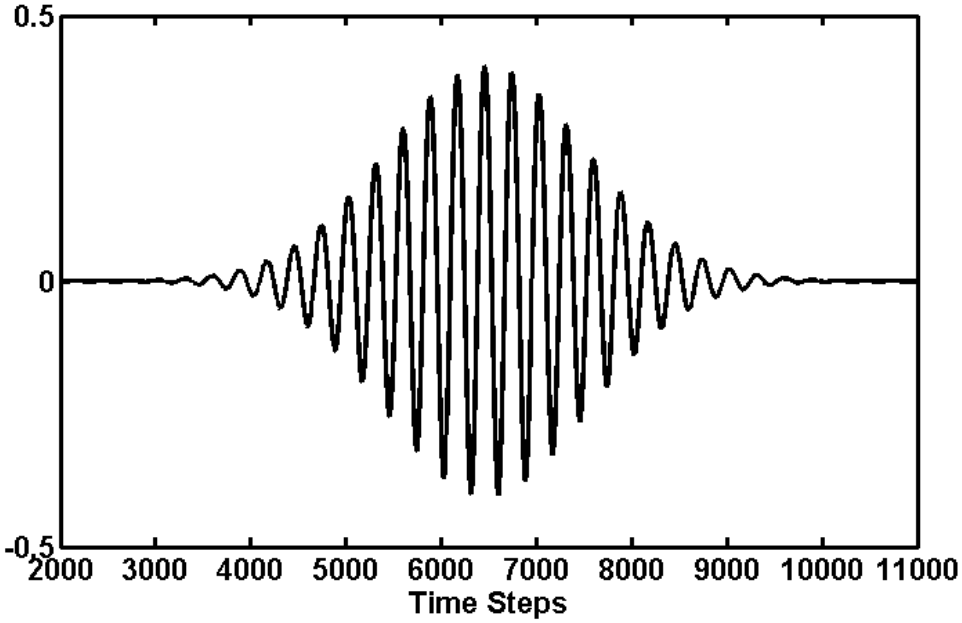

Figure 4.2 Field profile inside the planar waveguide shown in figure 4.1

By means of Fast Fourier transform (FFT) of the transmitted and reflected recorded time-dependent fields, the reflection coefficient was calculated. The study was carried out by surrounding the computational domain with five different numbers of total UPML cells, 2, 5, 10, 15 and 20 respectively. The obtained reflection coefficients are illustrated in figure 4.3.

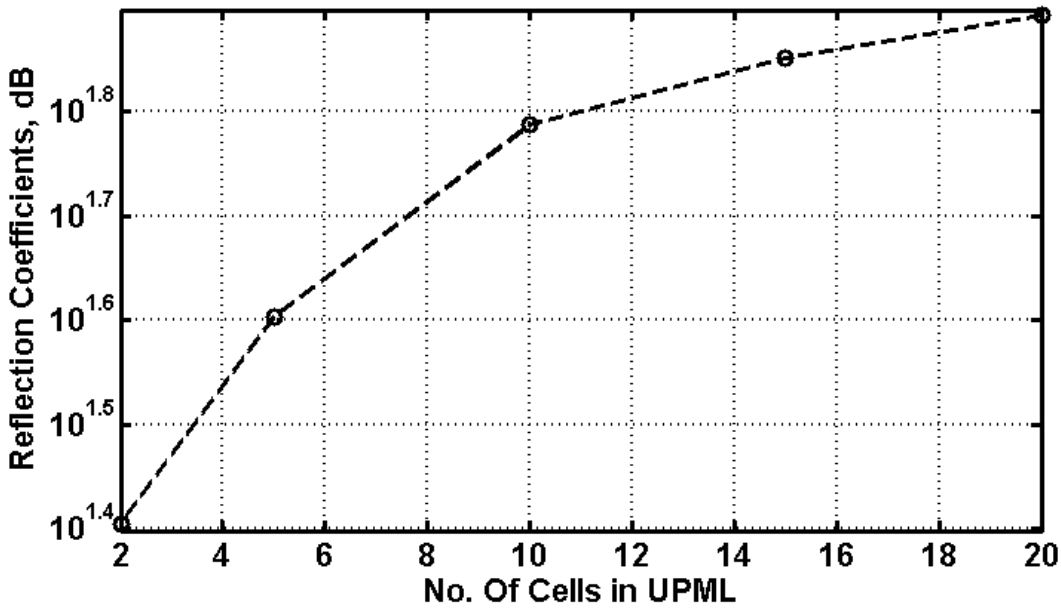

Figure 4.3 Effect of no. of UPML cells on the reflection coefficient

As may be observed from figure 4.3, the reflection coefficients obtained are about -25dB, -40dB, -61dB, -71dB, and -78 dB respectively. It can be noted from obtained results that the UPML is affected mainly by the cell size and the minimum reflection is achieved when the number of UPML cells is equal to 20 and therefore is considered for the rest of the simulations in this research study.

4.3 Study the Numerical Convergence of MRTD

Having established the effectiveness in terms of absorptions of the proposed UPML scheme, this UPML scheme is then employed in conjunction with the MRTD technique for analysis of optical microcavity ring to study the numerical convergence of MRTD method which in turn emphasis the validation of this technique. The single MRR whose schematic diagram is shown if figure 4.4, with core width w = 0.3 µm, ring diameter d =

5 µm, gap size g = 218 nm, and core and cladding refractive indices of n_{core} = 3.2 and n_{clad} = 1 respectively.

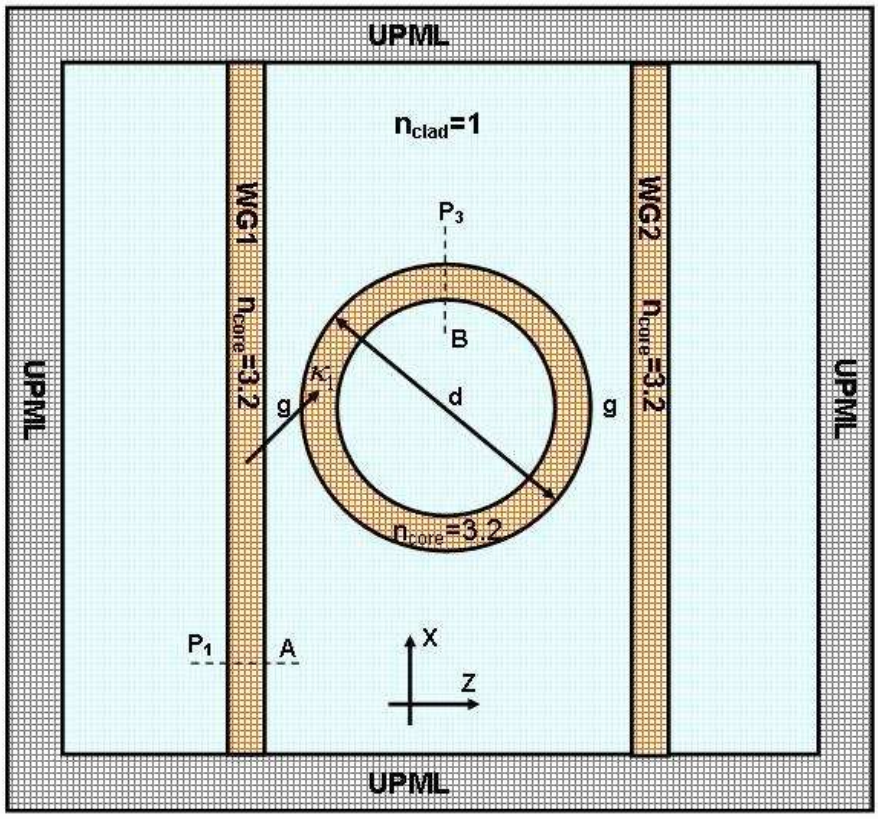

Figure 4.4 Schematic diagram of a microcavity ring resonator excited with a Gaussian pulse at 1.5 µm in order to study the convergence of MRTD scheme

In order to cover the frequency range of interest, a TE Gaussian pulse with parameter fixed to t_0 = 80 *fs* and T_0 = 20 *fs* with central frequency of 200THz ($\lambda_0 = c_0 / f_0 = 1.5\mu m$) has been injected in the input waveguide.

As shown in figure 4.4, a different cross-section detector is placed at the source section of the input waveguide (A) in order to record the time-domain variation of the incident field; another one is located inside the ring resonator (C), one-quarter of the way around from the input waveguide, in order to investigate the coupling efficiency. By means of

fast Fourier Transform (FFT) of the time-dependent fields, the poynting vectors densities along cross-section A, and B have been calculated and used to evaluate the coupling coefficient, κ_1 between input waveguide and ring as:-

$$\kappa_1 = \frac{P_3}{P_1} \tag{4.2}$$

The coupling efficiency provides an estimation of how much power is coupled into and from the cavity. In order to estimate about 99% of the full modal power, the integration for the power densities is carried out along a region that is three times bigger that the core width of the waveguide. In figure 4.5, the numerical convergence of MRTD method is studied for calculating the coupling efficiency from WG1 and the ring resonator κ_1, for four values of Δ, equal to 13.60nm, 21.8nm, 27.25nm, and 30nm respectively.

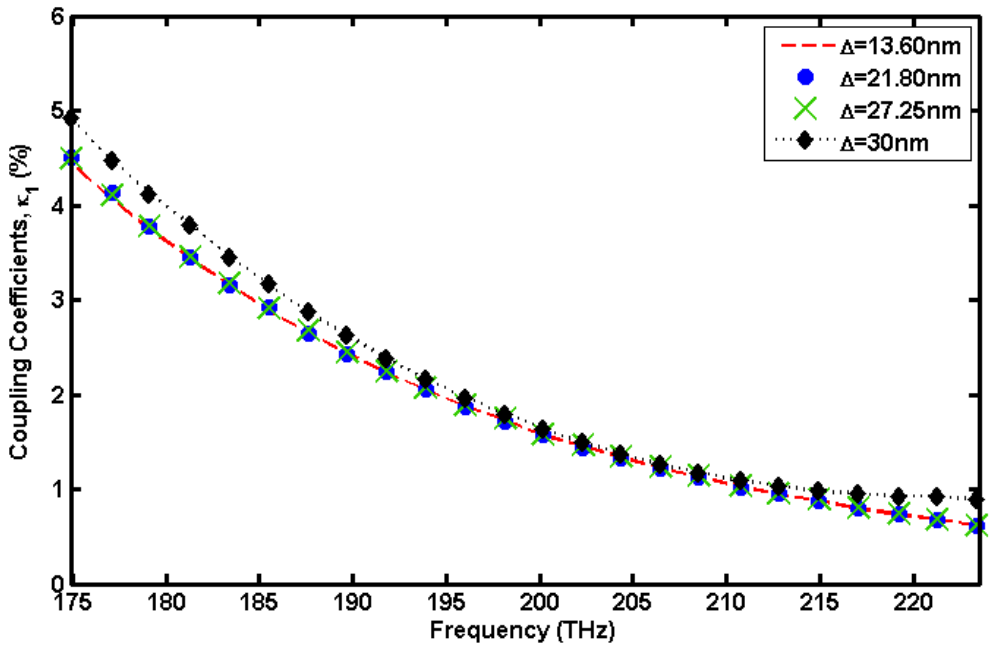

Figure 4.5 Coupling Efficiency κ_1 as a function of frequency with different meshes for g = 218 nm and 5μm-diameter ring of Fig. 4.4

In order to determine the coupling efficiency of the MRR, the simulation needs to be terminated before the field inside the ring completes its first round-trip. As it can be seen from figure 4.5, due to very small deviation for the three cases and thus are hard to be distinguished. This simulation results reveal the main property of the MRTD technique and its ability to reduce the expense in the computational domain by allowing the use of coarser grid resolution. Therefore, for the rest of the simulations in this research study, using Δ = 27.25 nm is considered to be the best choice in terms of low computational burden and saving CPU running time. Figure 4.6 shows the electric field pattern in different time intervals, once the pulse has been totally inserted, the frequencies that can resonate inside the ring are coupled to WG2 (*on*-resonance) via the ring, while the others (*off*-resonance) will carry on propagating along WG1 until reaches the UPML edge in the longitudinal direction (*x*). At this point, it rapidly reduces to negligible values showing that the UPML boundary condition performance stably and rigorously.

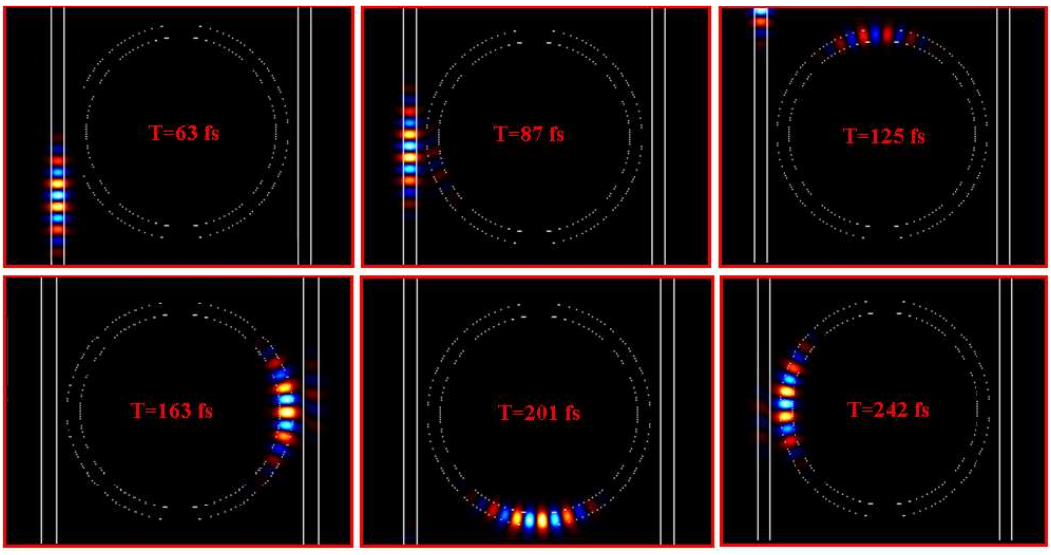

Figure 4.6 Visualization of snapshots in time of MRTD-computed Ey field of a pulse circulating around a 5 µm-diameter ring of Fig. 4.4 with Δ = 27.25 nm and g = 218nm

4.4 Assessment of MRTD against FDTD Method

The coupling efficiency between the input/output straight bus waveguide and the ring resonator plays a very important role in determination of the MRR performance [10], and can be controlled by several parameters such as gap width g, coupling length, diameter of the ring d, and waveguide width w [86]. For further assessment of MRTD scheme, the same MRR presented in figure 4.4 is used.

The variation of coupling coefficient from WG1 and the ring resonator, κ_1 with frequency when f = 200THz and d = 5µm is calculated for three different values of g, equal to 0.191µm, 0.218µm, and 0.245 µm respectively. The results are shown and compared in figure 4.7 to those obtained on the same structure when the FDTD is used.

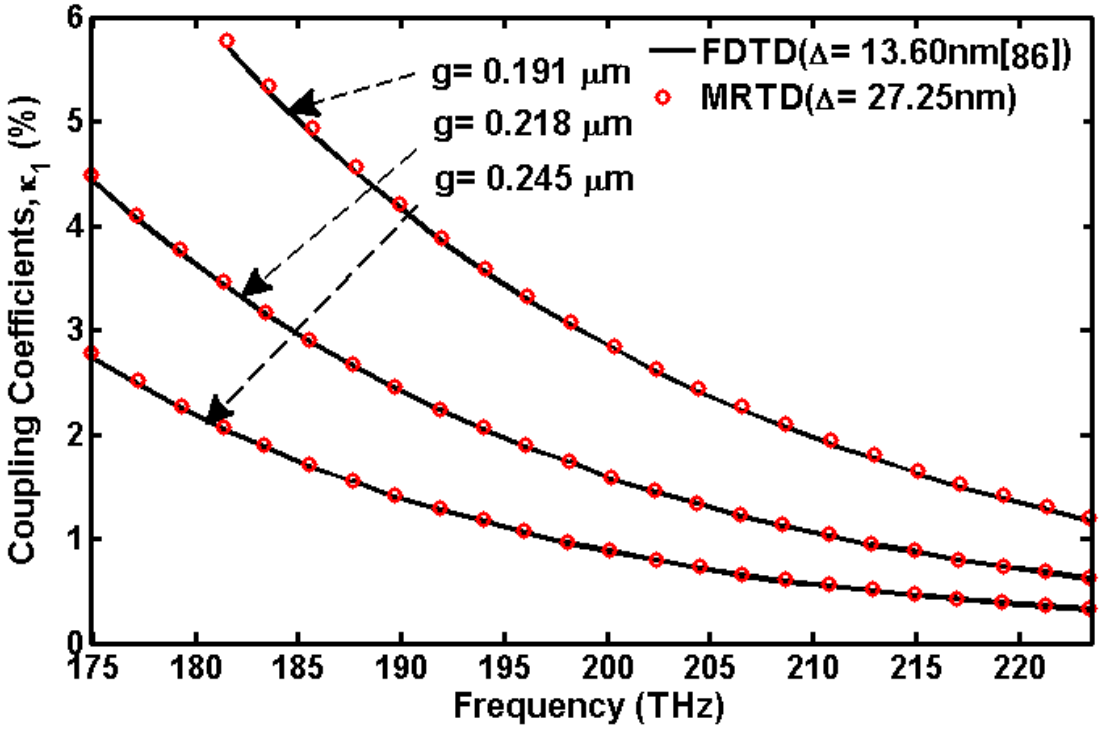

Figure 4.7 Variation of the coupling coefficients with frequency and gap size, g, using both MRTD and FDTD methods for straight waveguide coupled to 5 µm-diameter ring microcavity.

It can be observed the excellent agreement between the results reported here using MRTD and their counterparts reported in [86] using FDTD approach. As noted from this figure, MRTD is accurate for the analysis of this class of devices. With the intention of emphasis the validation of the suggested technique, the execution times of developed MRTD is compared with the one obtained with the commercial software Full-Wave based on FDTD for the same structure. The execution times of MRTD and conventional FDTD are then compared in Table 4.1.

Table 4.1 comparisons between MRTD and FDTD in terms of computational time

Method	Δ (nm)	Run Time (mints)
MRTD	27.25	77
FDTD	13.60	129

From table 4.1, it is evident that, allowing the mesh size to be about half the one adopted by FDTD, MRTD scheme can achieve same level of accuracy while the overall smaller execution time (by factor of approximately 2) is required. The possibility of saving CPU running time makes the MRTD an efficient alternative numerical scheme to the commonly used FDTD for the design of MRR structures.

4.5 Summary

This chapter has presented a detailed numerical assessment of MRTD scheme in conjunction with UPML boundary condition. The assessment was firstly performed on a planar waveguide with emphasis on investigating the effect of the number of cells used

for the UPML structure. Since the suggested UPML has been assessed on optical waveguide, it will be used in the design and analysis of MRRs. Next, the developed MRTD code has been tested for MRR. A number of simulations have been carried out with a variety of mesh size in order to investigate the numerical convergence of MRTD. From this simulation results, MRTD provides high numerical precision without the strict limitation on the space discretisation. After that, a comparison was made between conventional FDTD and the newly suggested MRTD in terms of coupling coefficient. It was found that the newly suggested MRTD outperforms the conventional FDTD by allowing bigger mesh size. Since the newly developed MRTD has been assessed on different optical devices, it will be used in the design and analysis of MRRs in more detail in the following chapters, where in chapter five single microcavity ring resonator devices are presented, and in chapter six double microcavity ring resonators are investigated.

Chapter 5

MRTD Modelling of MRR Based on High-Index Contrast Waveguide

5.1 Introduction

In the recent years, the research has dedicated great attention to develop optical fibre networks to support the increasing bandwidth demands of many applications. Wavelength division multiplexing is found to be very attractive and promising for increasing the bandwidth of installed and future optical fibre system in point-to-point transmission links. Since optical filters are key devices for WDM systems, this chapter proposes to investigate a compact optical filter with add/drop ability without changing the signal quality using semiconductor optical MRRs.

In this chapter, the developed MRTD code has been used to analyse the MRRs, exploring the effect of different structural parameters on both coupled and transmitted power.

5.2 Design Considerations of Optical Microcavity Ring Resonators

5.2.1 Introduction

Recently, optical MRRs based on high-index-contrast waveguides gained increasing attention because of their potential as building blocks for optical wavelength filters [15, 22, 35, 81 77], optical switches [105], optical routers [20], all the way to optical sensors [21], and optical logic gates [101, 89]. The conventional low-index-contrast waveguides have the advantages of showing low propagation loss [12]. On the other hand, since a very large bend radius is required to achieve a high efficiency bend, MRRs based on such waveguide involve a very large radius for the design of the circular waveguide which builds the ring.

As a result, the overall size of the ring resonator is increased while the free spectral

range (FSR) which is inversely proportional to the diameter of the ring is limited [12]. Research efforts have been directed towards designing new structures to achieve a wide FSR without decreasing the diameter of the ring.

Different approaches in literature including double-ring resonators and triple-ring resonators [12], [65, 94]. Thanks to the recent advances in material technology and fabrication techniques, MRRs with physical dimensions comparable to optical wavelength have been made possible to be fabricated with negligible bending loss [12].

The requirement of achieving higher performance for future of optical communication devices, as well as computing and signal processing devices to complement or competitively replace their microelectronic counterparts in integrated circuits, make it essential that novel optical microstructures be explored. High FSR, high extinction ratio, small size, and selectivity of coupling to the output ports are considered as figure of merit defining the good performance of this kind of structures [12]. In this chapter, the MRTD scheme is proposed here for the first time, to the best of the author's knowledge for the analysis of MRRs.

In this chapter is to provide a detailed study of MRR geometry parameters as coupling gap size, microring radius of curvature, and waveguide width, in order to predict and optimise the device performance.

5.2.2 Coupling Characteristics of MRRs

The coupling efficiency between input/output straight bus waveguides and the ring resonator plays a very important role in the determination of the MRR performance [7, 12, 13, 88], and can be controlled by several parameters such as gap width g, coupling

length, diameter of the ring *d*, and waveguide width *w* [110, 78].

By means of MRTD technique, the performance of MRRs in terms of coupling efficiency will be discussed in this section. A two-dimensional coupled microcavity ring resonator surrounded by air with diameter *d*, and refractive index contrast $\Delta n = n_c^2 - n_{cl}^2 / 2n_c^2 \cong 0.45$, where n_{core} and n_{clad} are the refractive index of the core and cladding respectively, is coupled to parallel straight waveguides, *WG1* and *WG2* with core width *w*, to represent input and output couplers respectively, as shown in figure 5.1. The structure is discretised with square cells Δ = 27.25 nm while the time step is fixed at $\Delta t = 9.0896\times10^{-18}$ s. All the results for the coupled and transmitted power are obtained by injecting a source-field along the x-direction, modulated at wavelength 1500 nm and 20 fs wide Gaussian pulse. The source-field is given as [82]

$$E_y(z,t) = E_{TE_0}(z) e^{-\frac{(t-4T_0)^2}{T_0^2}} \sin\left(\frac{2\pi c}{\lambda_0} t\right) \tag{5.1}$$

where E_{TE_0} corresponds to the fundamental *TE0* mode profile of the input waveguide, T_0 is the width of the Gaussian pulse and T_0 is chosen to be 20 fs and $\lambda_0 = 1.5\mu m$ is the central wavelength. Reference points are chosen at different locations in the structure at which the time variation of the field at each point is recorded.

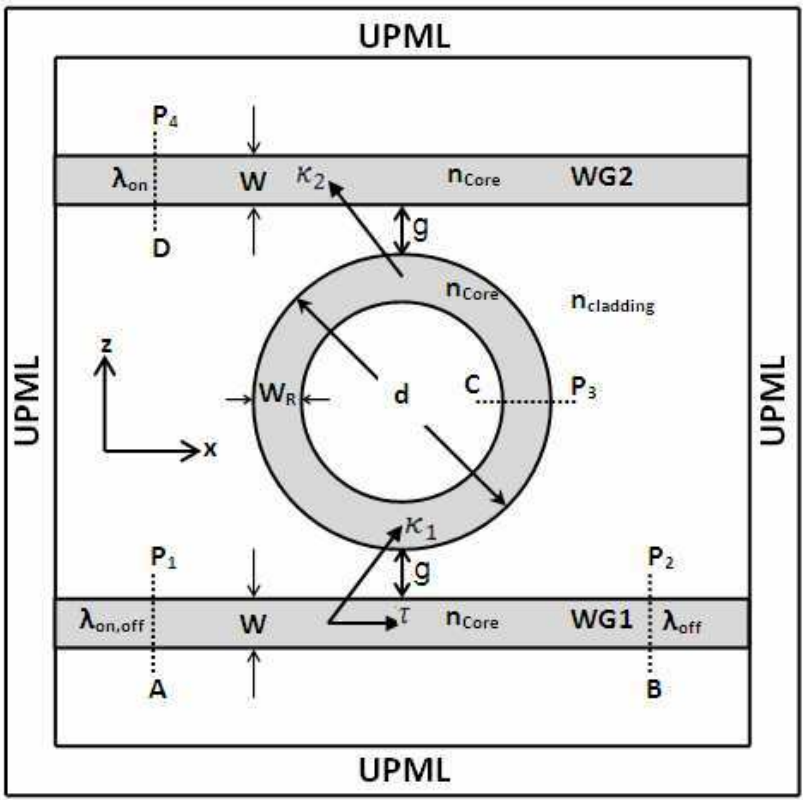

Figure 5.1 Schematic diagram of the MRR of diameter d = 5µm and width, w = 0.3µm.

As shown in figure 5.1, different cross-section detectors are strategically placed in the structure: the first cross-section detector is placed at the source section of the input waveguide (A) in order to record the time-domain variation of the incident field, a second detector is inserted at the output section (B) so as to record the time-domain variation of the transmitted field, another one is located inside the ring resonator (C), one-quarter of the way around from the input waveguide, in order to investigate the resonance process around the ring and evaluate the coupling efficiency.

The last cross section detector is placed at the output section of the second waveguide (D) to record the time-domain of the dropped field. By means of Fast Fourier Transform (FFT) of the time-dependent fields, the Poynting vector densities along cross-section A,

C, and D have been calculated and used to evaluate the coupling coefficient, κ_i , between input/output waveguide and the ring as:-

$$\kappa_i = \frac{The\ \ Coupling\ \ \ Power\ \ \ from\ \ each\ \ coupler\ \ \ (P_{coupld}\ )}{The\ \ Input\ \ \ Power\ \ \ to\ the\ \ same\ \ coupler\ \ \ (P_{input}\ )} \tag{5.2}$$

The coupling efficiency provides an estimation of how much power is coupled into and from the cavity. In order to estimate about 99% of the full modal power, the integration for the power densities is carried out along a region that is three times bigger than the core width of the waveguide. The structure in figure 5.1 is designed to drop an optical signal to port D if proper phase matching condition exist [21]

$$n_{\ eff}\ \ \pi\, d\ \ =\ \ m\ \ \lambda \tag{5.3}$$

where λ represents the signal wavelength inside the medium, n_{eff} is the effective refractive index of the medium.

When a defined spectral range is injected as a source, the frequencies that can resonate inside the ring are coupled to WG2 (on-resonance case) via the ring, while the others, for which the relation (5.3) is not satisfied, carry on propagating inside WG1 and can be found in output at port B (off-resonance case).

5.2.2.1 Influence of separation distance on the coupling and transmission efficiency

The idea in this section is to investigate the effect of change in the separation distance, g on the coupling performance using MRTD. The variation of coupling coefficient from WG1 and the ring resonator, κ_1, with frequency when f_0 = 200THz, $w = w_R$ = 0.3μm and d = 5μm is calculated for three different values of g, equal to 0.191μm, 0.218μm, and 0.245μm respectively. In order to calculate the coupling efficiency of the MRR, the

simulation needs to be terminated before the field inside the ring completes its first round-trip. The results are shown and compared in figure 5.2 to the coupling coefficients from the ring to WG2, κ_2 on the same structure.

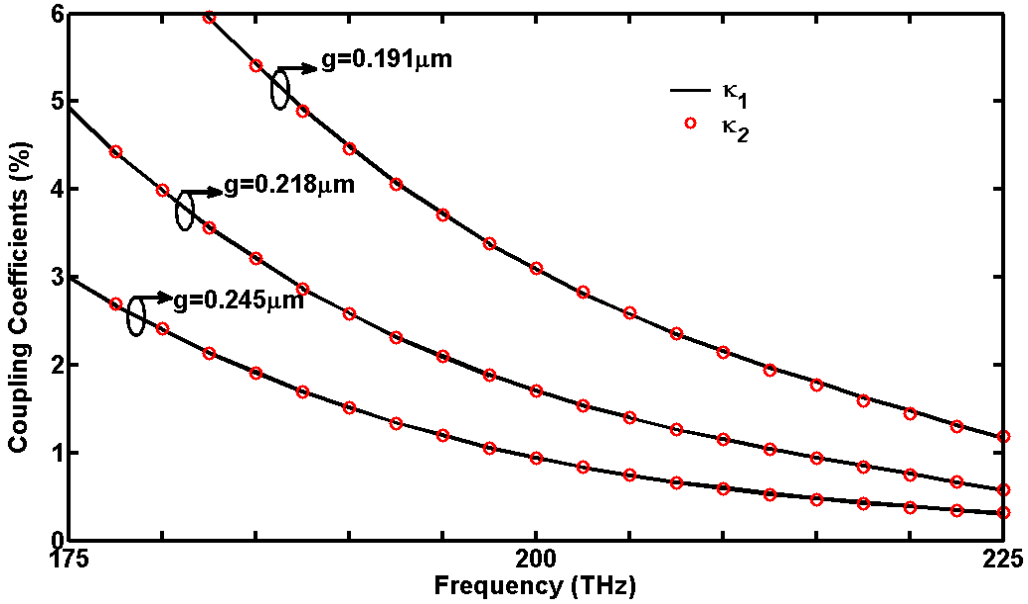

Figure 5.2 Variation of the coupling coefficients with frequency and gap size, g, in both side of 5 μm-MRR ($w = w_R = 0.3$ μm)

The results from this figure is summarised for f = 200 THz (λ = 1.5μm) in Table 5.1.

Table 5.1 Summery of coupling coefficients for input/output couplers at λ=1.5μm for different gap size

MRTD		
g (μm)	κ_1 (%)	κ_2 (%)
0.191	2.85	2.807
0.218	1.58	1.470
0.245	0.894	0.859

The comparison between κ_1 and κ_2 demonstrates that the symmetry property of the input/output coupling process is satisfied. This property will play an essential role in achieving both good transmission and large extinction ratio. Next, figure 5.3 presents coupling and the transmission coefficients variation with the gap widths for λ = 1.5μm.

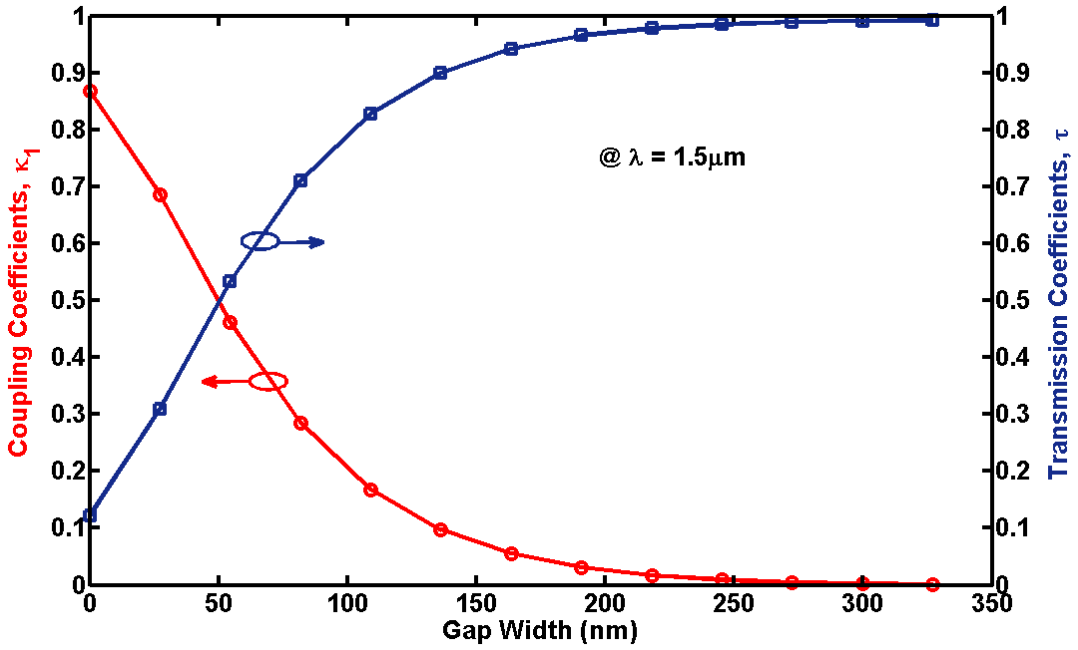

Figure 5.3 MRTD-computed coupling and transmission coefficients as function of the gap width for ring diameter *d* = 5μm at λ=1.5μm (w = w_R = 0.3μm).

As figure 5.2 and figure 5.3 suggest that when the gap size is increased, the amount of power coupled to the ring resonator rapidly decreases while the transmitted power increases. At fixed gap size, the coupling efficiency also significantly decreases towards higher frequencies as a result of the correspondent increased effective gap size.

5.2.2.2 Influence of the waveguide width on the coupling efficiency

Following, the influence of waveguide width on coupling efficiency is considered here. In this case, the variation of coupling coefficient from WG1 and the ring resonator, κ_1, with frequency when f_0 = 200THz, g = 191 nm and d = 5μm is calculated for five different values of w, equal to 0.20μm, 0.21μm, 0.24μm, 0.27μm, and 0.30μm respectively. Figure 5.4 shows the variation of coupling efficiency with the waveguide width.

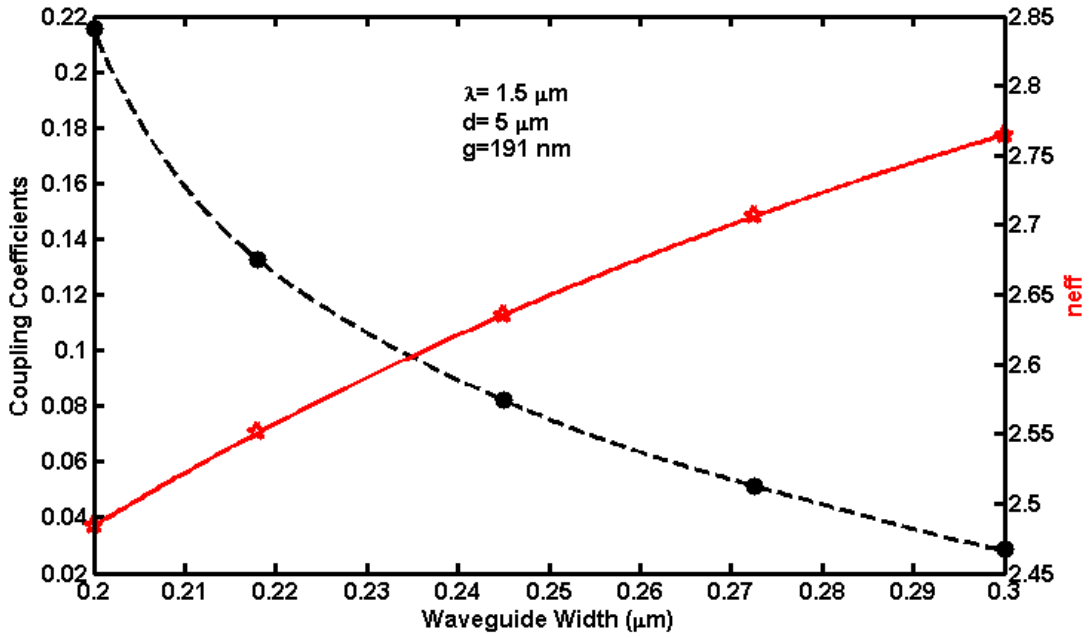

Figure 5.4 Variation of coupling coefficients and effective refractive index as function of waveguide width for ring diameter d = 5μm, g = 191nm at λ = 1.5μm

It is clear that the increase of waveguide width will lead in turn to increase in the effective refractive index Thus, the modes in the straight waveguide and the curved waveguide which form the ring are not well phase-matched. Therefore, the coupled power decreases.

Figure 5.5 shows the effect of symmetrical changes of both ring and straight waveguide width on the coupling efficiency. As evident from figure 5.4, the effective refractive index is a function of the waveguide width. Thus, as the waveguide width w and w_R are increased, the cross coupling between the straight waveguide and the bent waveguide which builds the ring decreases. Moreover, the phase mismatch between the straight waveguide and the ring resonator can be improved by reducing the width of the waveguide which in turn lead to increasing the coupling coefficients.

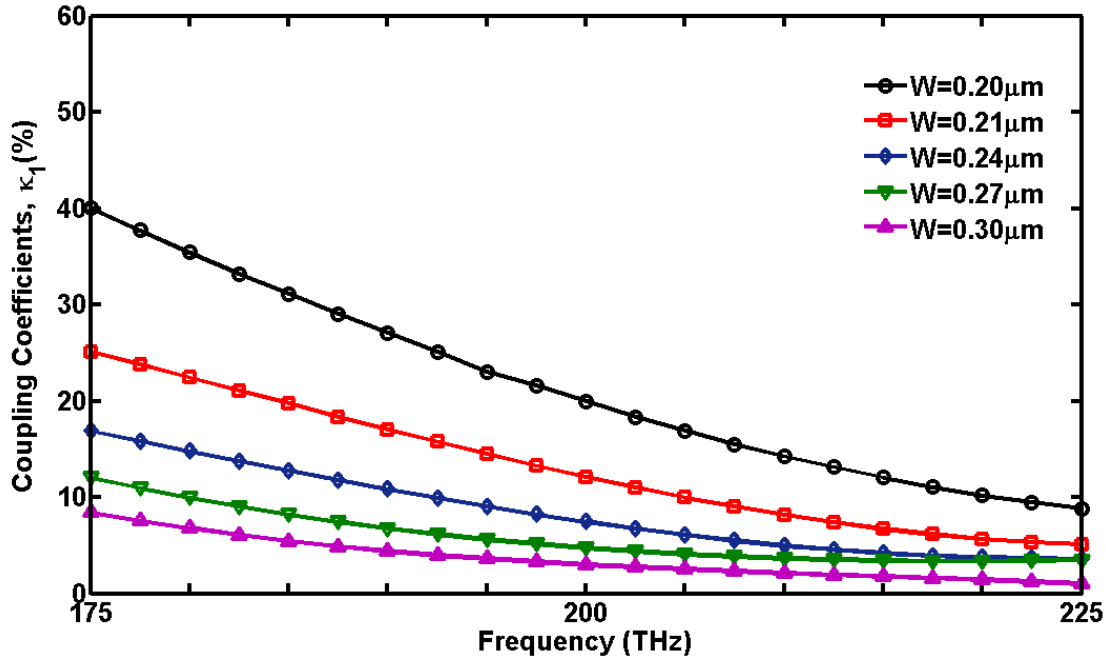

Figure 5.5 MRTD-computed coupling coefficients as function of frequency and waveguide width ($w = w_R$) for ring diameter d = 5μm, g = 191nm at λ = 1.5μm

Due to strong optical confinement of the waveguide, the separation distance between the input/output straight waveguide and the cavity needs to be very narrow in order to accomplish the required level of coupling strength. A key step in the direction of practical production and commercialisation of these devices is the development of a new design that is probably capable of alleviating the requirement for such narrow gap. Following, the structure is modified to improve the phase matching condition and eliminates high-order mode components that can deform the field in the cavity. This is assumed to be achieved by reducing the width of the straight waveguide while keeping the ring waveguide. A comprehensive study of coupling coefficients variations with frequency and gap size is presented in figure 5.6 when the width of the straight waveguides and the ring waveguide are 0.2 and 0.3μm, respectively.

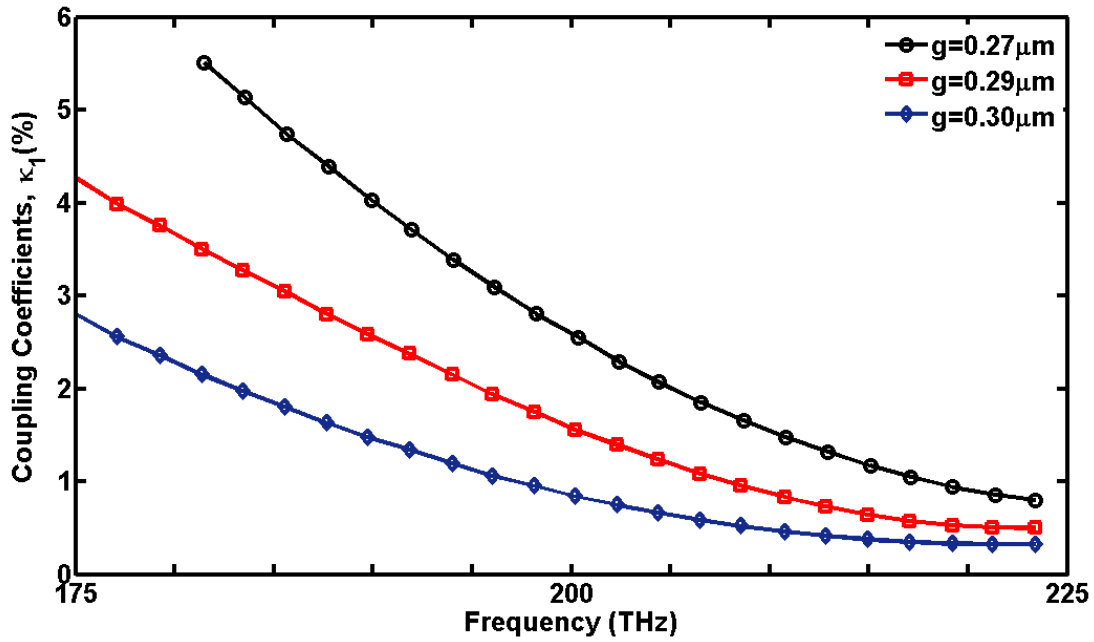

Figure5.6 MRTD-computed coupling coefficients as function of frequency and gap size g for 5μm- diameter ring (w = 0.2 μm, w_R = 0.3 μm)

The results from these simulations prove the potential advantage in allowing wider air gap while providing the desired coupling level.

5.2.2.3 Influence of the ring size on the coupling efficiency

For further study, the consequence of the ring size on the coupling efficiency is examined in figure 5.7. The variation of coupling coefficient from WG1 and the ring resonator, κ_1, with ring diameter is computed at λ = 1.5 μm for three different values of g, equal to 0.191μm, 0.218μm, and 0.245μm respectively. In this case, the value of both straight and bent waveguide width is chosen to be 0.3 μm.

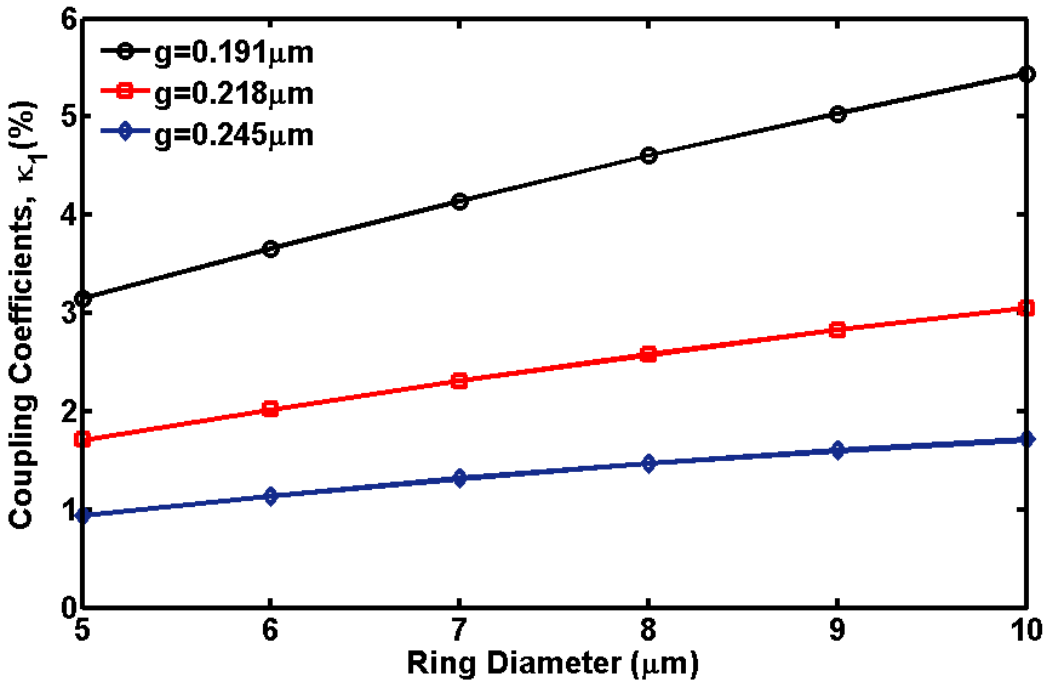

Figure5.7 MRTD-computed coupling coefficients as function of ring diameter *d*, and gap size g at λ = 1.5 μm ($w = w_R$ = 0.3 μm)

It can be seen that the coupling coefficients critically depends on the ring diameter. The amount of power coupled to the ring resonator rapidly increases when the ring diameter is increased. This can be explained as a result of the corresponding increased effective gap size. Although the coupling coefficients increase while increasing the ring diameter, the interaction length for the larger diameter ring is still short to avoid the back coupling from the ring to straight waveguide.

5.2.3 Transmission Characteristics of MRRs

The transmission at port B for a 5μm-diameter MRR is considered. The results are obtained using developed MRTD scheme and compared with FDTD results for the same ring as presented in [86]. In this case the cavity and the straight waveguides have a core of width $w = w_R = 0.3$ μm, and the separation distance is $g = 0.245$ μm. The single mode of the input waveguide is lunched with a source-field along the *x*-direction, modulated at wavelength 1500 nm and 20 fs wide Gaussian pulse. The response of this resonator is scanned over frequency range 185 - 211 THz.

5.2.3.1 Extraction of the Resonance Wavelengths

The power density calculated at port B and normalised to the one at the input port A is shown in figure 5.8. In order to calculate the transmittance of the MRR, the simulation needs to be run until the energy in the cavity has adequately died down.

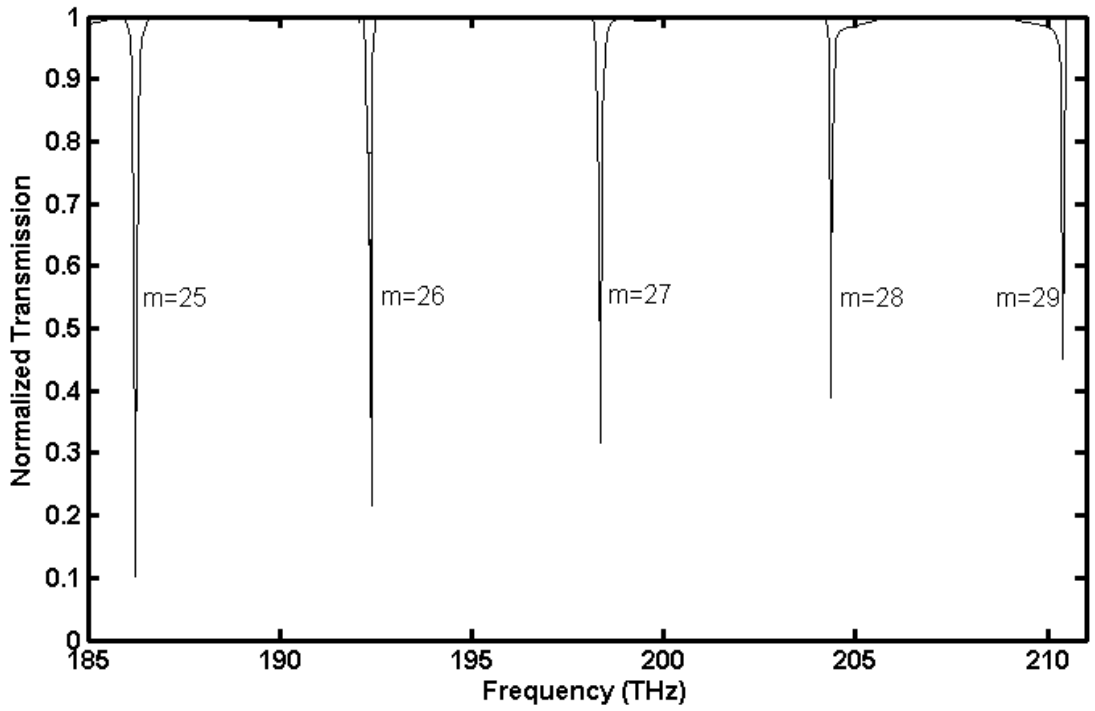

Figure 5.8 MRTD-computed transmittance of 5μm-diameter microcavity ring resonator ($w = w_R$ = 0.3μm).

From this figure, the localised resonance peaks of the MRR are derived. In Table 5.2, a comparison between these results and once obtained through FDTD analysis in [86] is shown.

Table 5.2 Numerical values for selected resonance wavelengths of MMR. The calculations with MRTD and FDTD (as taken from Table 1 in [86]) are for the MRR with Parameters d = 5 μm and w = 0.3 μm.

	Resonance wavelengths, λ_{res} (μm)				
Present	1.42585	1.46771	1.51209	1.55925	1.61030
Ref [86]	1.42798	1.47015	1.51488	1.56244	1.61310

It is found that results are in good agreement with deviation below 1%. Following, the *on*-resonance case of a continuous wave injected at wavelength of λ_{res} = 1611.17 nm is computed. The resulting sinusoidal steady-state field profile is shown in figure 5.9. As it can be seen, the most of the energy has switched to WG2 by means of the resonance coupling process and is collected in output at port D.

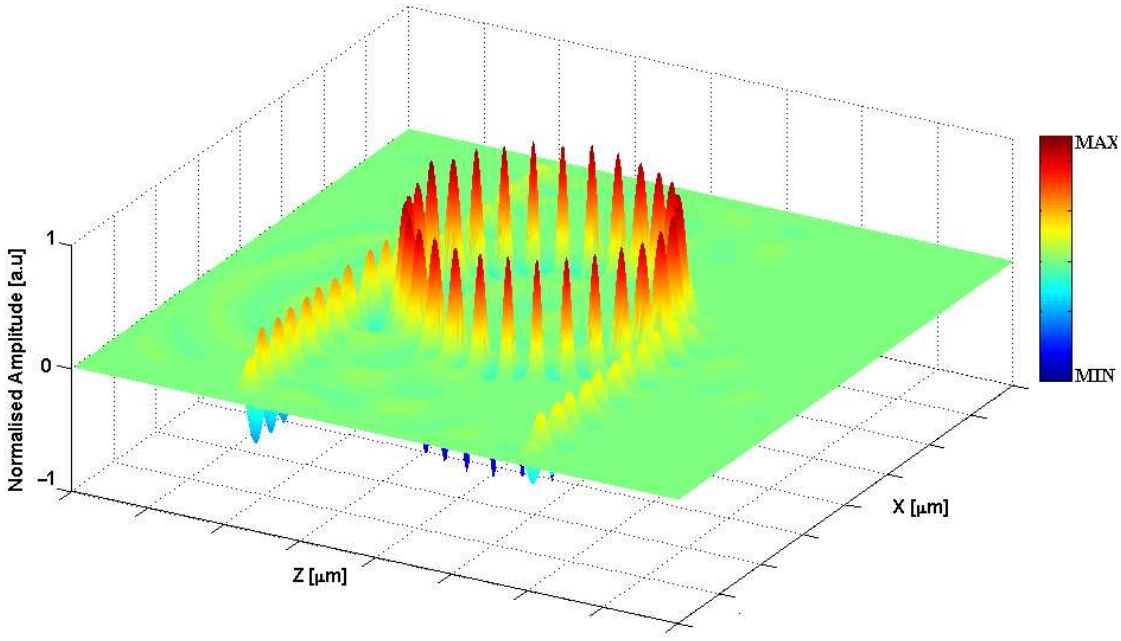

Figure 5.9 Sinusoidal steady-state of the field distribution in 5μm-diameter microcavity ring resonator on-resonance case at 186.3THz.

Similarly, the *off*-resonance case for a continuous wave at wavelength of λ_{res} = 1597.44 nm is carried out and shown in figure 5.10. In this case, the figure shows that no coupling between WG1 and the ring has occurred and thus nearly 100% of the signal is transmitted at output in port B.

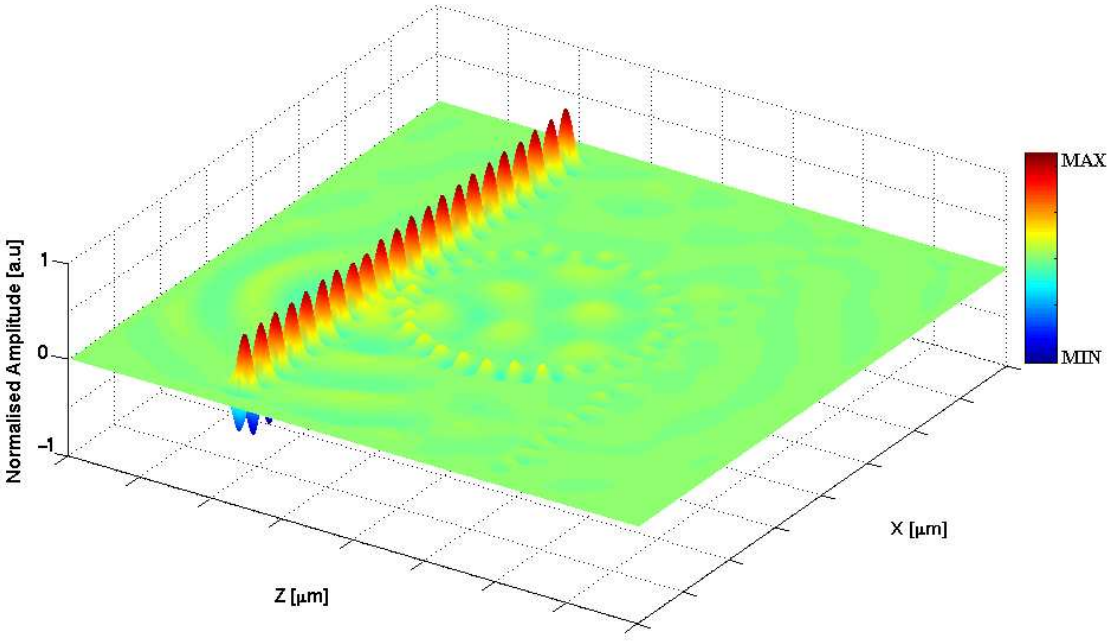

Figure 5.10 Sinusoidal steady-state of the field distribution in 5μm-diameter microcavity ring resonator off-resonance case at 187.8THz.

5.2.3.2 Calculation of Free Spectral Range

A micrometric size waveguides exhibit significant dispersion and due to the localised resonance wavelengths that are spaced far apart, the effective index will be varied at each resonance wavelength. In the vicinity of 1550 nm, a typical result is revealed in figure 5.11.

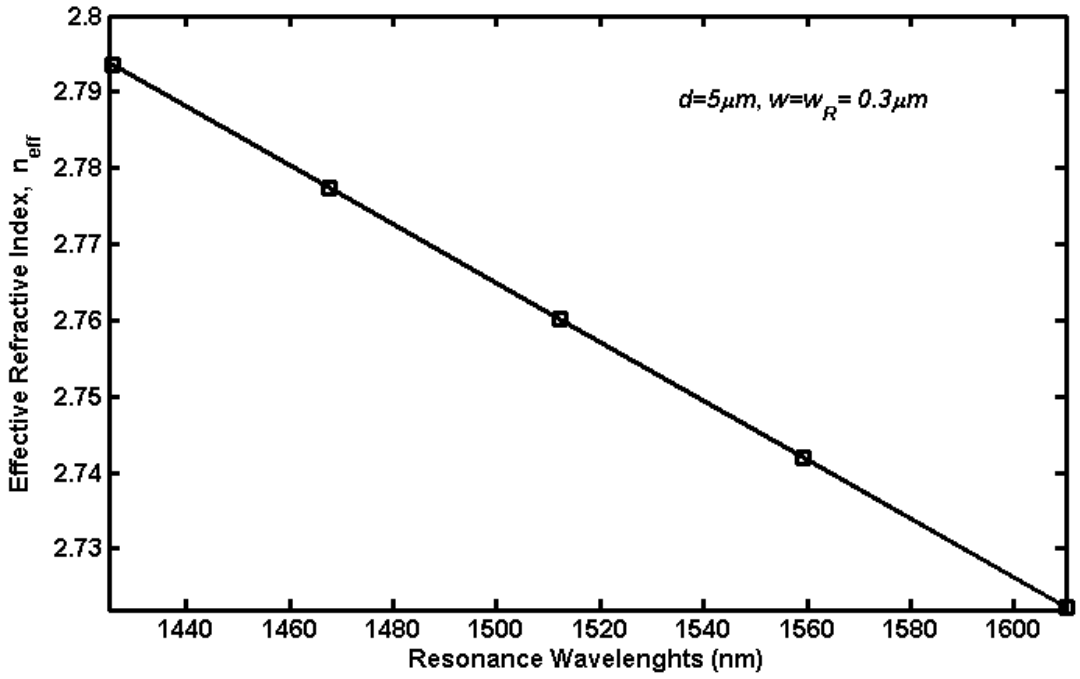

Figure 5.11 Effective index of 5μm-diameter microcavity ring resonator as a function of wavelength ($w = w_R = 0.3\mu m$).

From this figure, it is obvious that the effective refractive index is basically a linear, decreasing function of resonance wavelength. The variation of resonance wavelength with corresponding wave number is illustrated in figure 5.12.

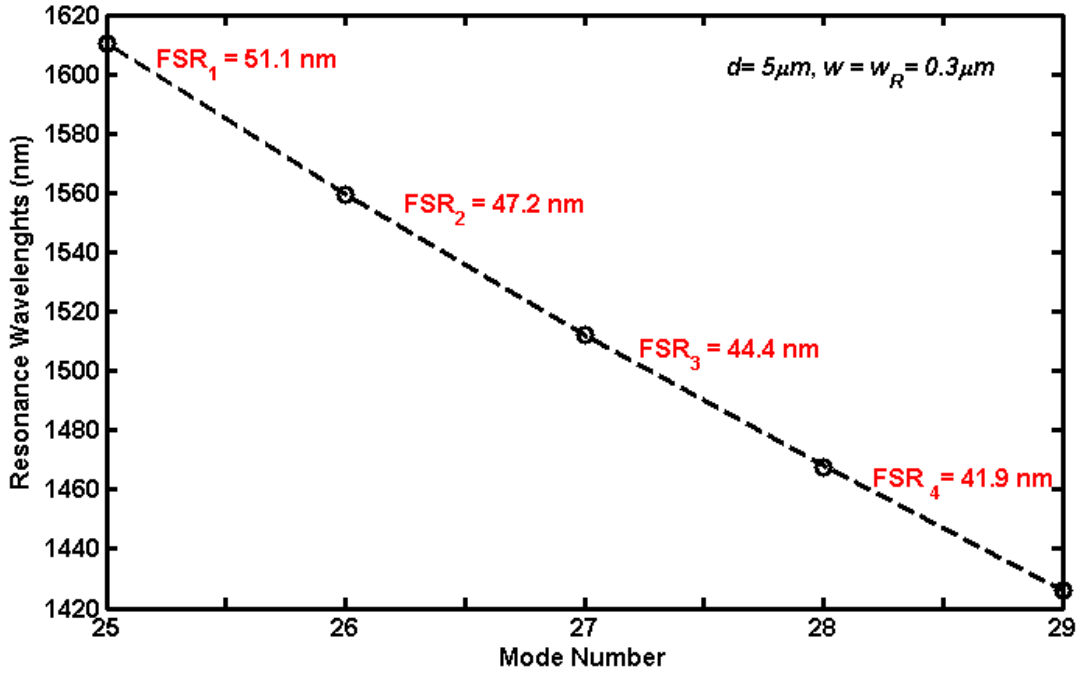

Figure 5.12 Free spectral range of 5μm-diameter microcavity ring resonator as a function of mode number ($w = w_R = 0.3\mu m$).

It may be observed that the entity of FSR decreases as the wavelength decreases due to the large dispersion effect of the waveguide. This behaviour agrees with results obtained in [86]. The finesses is calculating by forming the ratio of free spectral range, FSR, to the width of the resonance, Δ_λ, at the half-power points and is found to be ranges between 117 and 162.

5.2.3.3 Calculation of Q-Factor

The quality factor (Q) of the m^{th} resonance is calculated straight from the power spectrum presented in figure 5.5 and shown in figure 5.13.

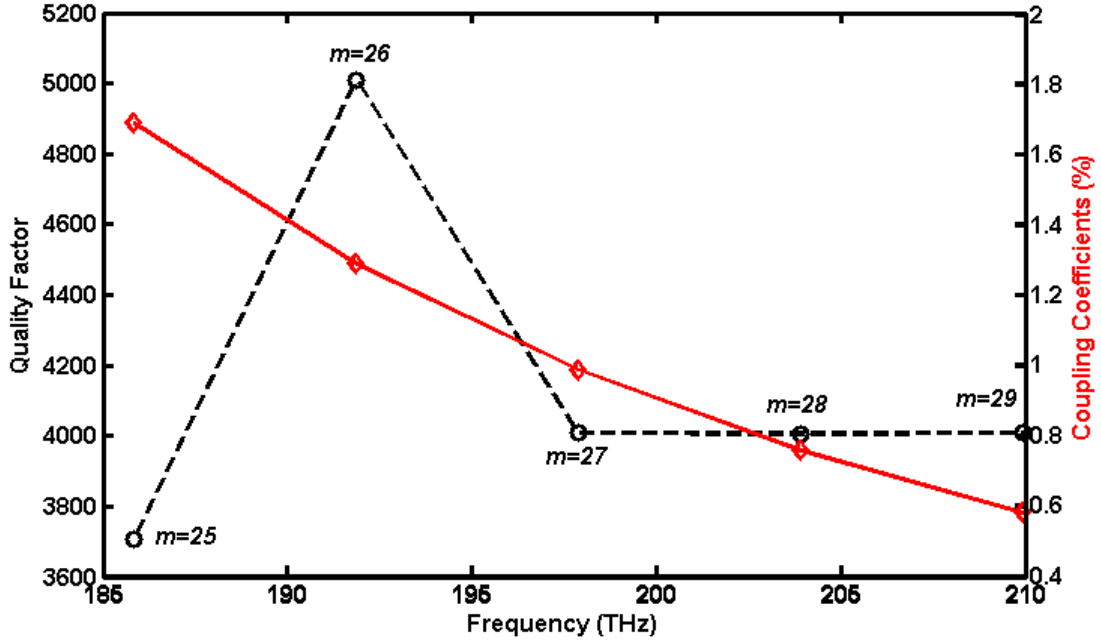

Figure 5.13 Variation of Quality factor and coupling coefficients with resonance frequency of 5µm-diameter microcavity ring resonator ($w = w_R = 0.3\mu m$)

These rely on only the coupling efficiency which decreases significantly at higher frequencies, the quality factor conversely should increase [12], it is clearly observed for the first two resonance (m=25,26). However, then the Q falls at the higher frequency resonances duo to side walls roughness that cause strong scattering at high frequencies.

5.3 Summary

In this chapter, the MRTD scheme, based on scaling functions from CDF family of order (2, 4) is successfully applied to the numerical analysis of microcavity ring resonator coupled to single-mode waveguides. Applied in conjunction with UPML scheme for the rigorous truncation of the computational window, the technique has proven good level of accuracy in determining the coupling coefficients and resonance behaviour of this device. While a coarse grid resolution compared to FDTD technique is allowed. Numerical simulation performed on a high-index-contrast microcavity ring resonator showed improved computational efficiency of the presented approach by allowing the mesh size to be about half that of FDTD. Being suitable accurate and efficient numerical analysis of this kind of device, MRTD has been adopted to investigate how to optimise structure parameters, such as gap width, waveguide width, and ring diameter, in order to obtain the desired coupling coefficients.

Microcavity ring resonator devices have proven to live up to expectations with high potential, especially in optical regime. Here, they were used to design and implement WDM devices and in order to achieve high performance; double-ring resonator configuration will be discussed in the next chapter.

Chapter 6

MRTD Analysis of PDMRR Based on High-Index Contrast Waveguide

6.1 Introduction

In this chapter, the MRTD approach based on the expansion in terms of only scaling function (S-MRTD) is extended for modelling double ring resonator based on high-index-contrast. In the passive microring resonators, the coupling coefficients, and the resonant-mode quality factor and the rejection ratio depend very much on the characteristics of the coupled microring. The analysis is mainly focused on the extraction of resonance modes where the effect of different parameters of the structure on transmitted and coupled power is investigated. The aim of this chapter is to explore the feasibility of employing a parallel-cascaded double-microcavity ring resonator (PDMRR) to realise high performance in terms of rejection ratio without compromising the quality factor. Parameters such as gap size and distance between the rings have been varied and useful concepts for the design of MRR are derived.

6.2 Simulation Results

The first structure analysed is the single MRR whose schematic diagram is shown in figure 6.1, with ring diameter d = 3.4µm, and core and cladding refractive indices of n_{core} = 3.2 and n_{cl} = 1, respectively. The structure is discretised into a uniform mesh with cell size 0.02725 µm and is terminated by 545 nm UPML to absorb the reflected power. So as to ensure the single-mode propagation at 1550 nm wavelength the width of the waveguide, w is chosen to be 0.3µm.

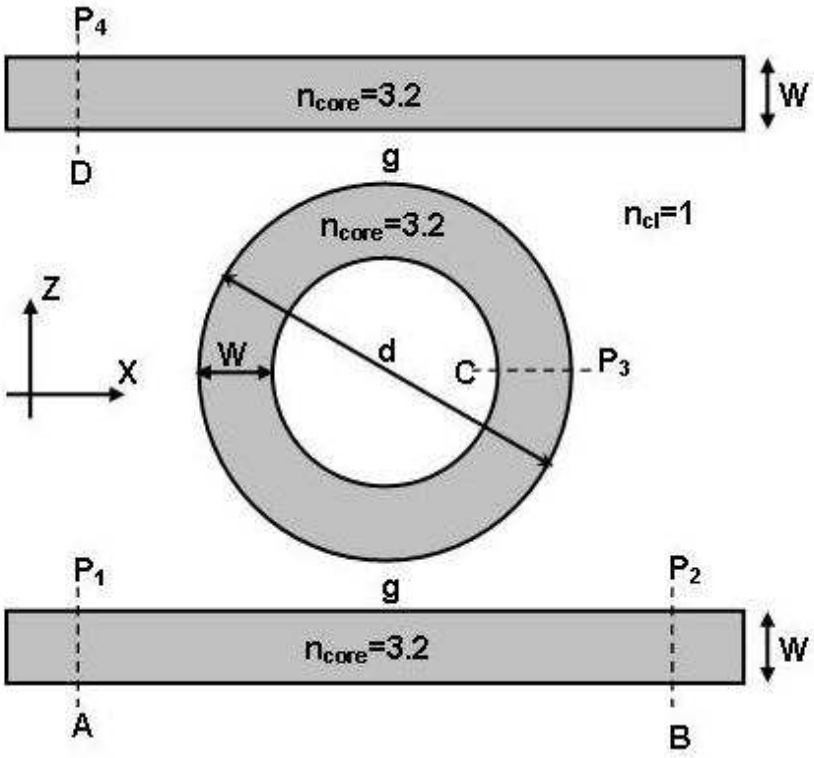

Figure 6.1 Schematic diagram of the 2-D single MRR of diameter d = 3.4µm coupled to two straight waveguides where n_{core} = 3.2, n_{cl} = 1 and width, w = 0.3µm.

As shown in figure 6.1, the reference points are labelled as A, B, and C in order to record the time domain variation of incident, transmitted, and reflected fields. By means of Fast Fourier Transform (FFT) of the recorded time-dependent fields, the coupled power at port C and the transmitted power at port B are calculated by dividing the coupled and transmitted spectra by incident power at port A. in order to cover the frequency range of interest, all the results for the transmitted and reflected power are performed by lunching the structure with a Gaussian pulse modulated in time by a sinusoidal function with the shape of the fundamental mode profile of the waveguide as [82]

$$E_y(z,t) = E_0(z)\, e^{-\frac{(t-t_0)^2}{T_0^2}} \sin(2\pi f t) \tag{6.1}$$

where $E_0(z)$ represent the fundamental mode profile of the waveguide, t_0 and T_0 are the time delay and time width of the Gaussian pulse fixed at 80fs and 20fs respectively, and f is the central frequency which is set to be 200THz ($\lambda_0 = 1.5\mu m$).

6.2.1 Influence of air gap width on the coupling and Quality factor

The effect of the gap size, g on coupled power, κ, and Q is shown in figure 6.2.

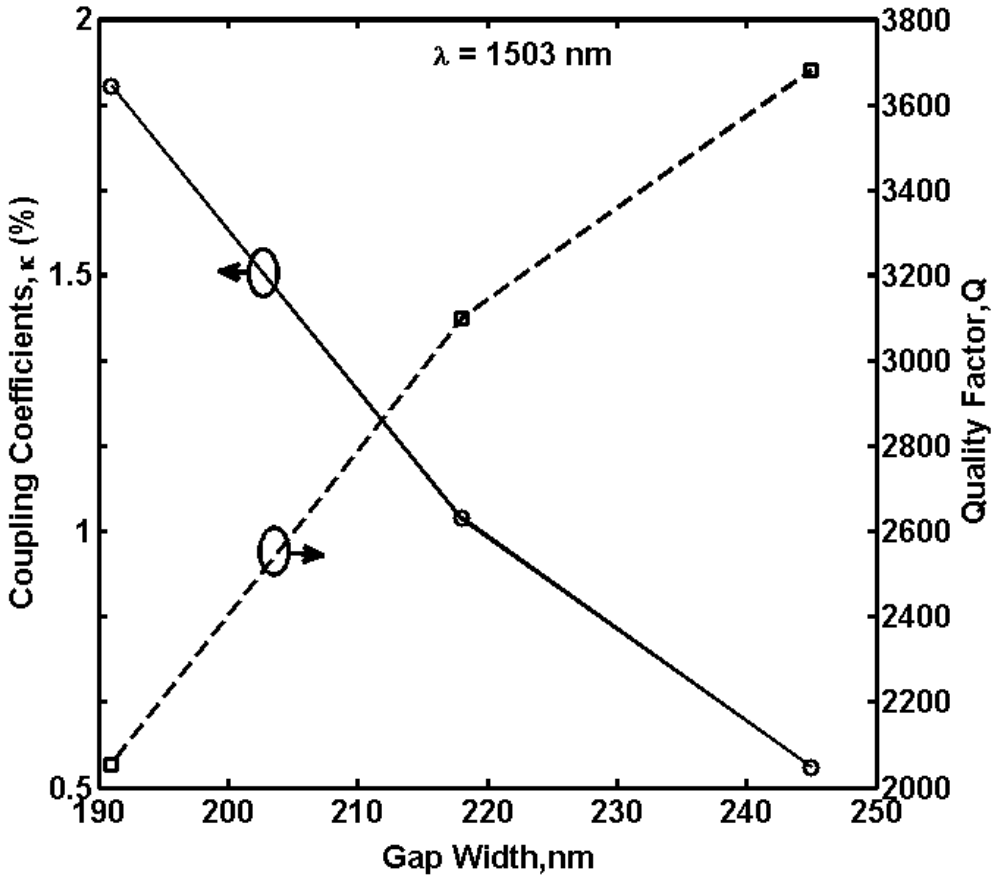

Figure 6.2 Variation of coupling coefficients κ and Quality factor Q with gap width g at 1503 nm

It is apparent that the variation of g has significant effect on both the values of Q and κ. In particular, when the gap size increase, the coupling coefficient of the different resonance modes decreases as a smaller fraction of power is exchanged between ring and waveguide, whereas the value of Q increases.

The results in figure 6.2 suggest that by using smaller gap size, the coupling coefficient can be enhanced in order to reduce the losses in the cavity and improve the performance in terms of transmission. However, at smaller values of gap size, the confinement of field inside the ring is also affected and as a result the quality factor is lowered. For this reason, an optimum value of a gap size need to be carefully chosen in order to achieve both reasonable high quality factor and coupling coefficients within the desirable range. According to figure 6.2, a good compromise can be achieved when choosing g = 218nm when the values of κ and Q are 1.024 % and 3098 respectively.

6.2.2 Transmission characteristics of 3.4 µm-diameters MRR

The transmission at port B for a 3.4µm-diameter MRR is considered. The results are obtained using developed MRTD scheme. In this case the cavity and the straight waveguides have a core of width w = 0.3 µm, and the separation distance is g = 218 nm. The response of this resonator is scanned over frequency range 180 - 220 THz.

6.2.2.1 Extraction of the Resonance Wavelengths and corresponding Q-factor

The transmission at port B for 3.4 µm-diameter ring and g = 218 nm is considered. The measured transmission spectrum of the single-ring resonator around 1550 nm is presented in figure 6.3.

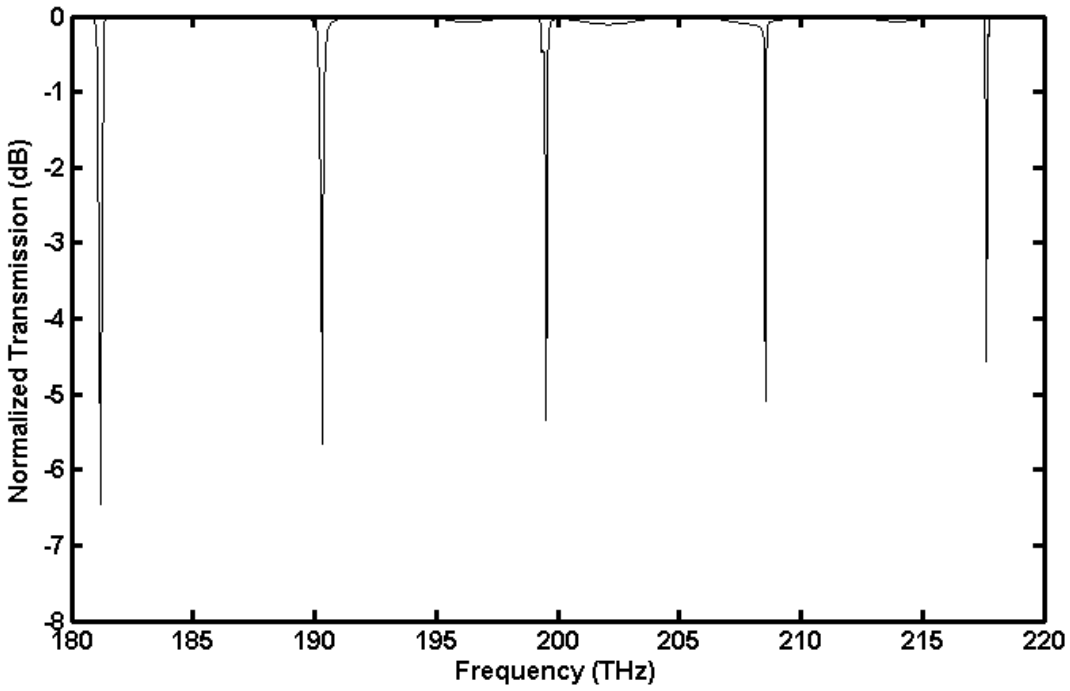

Figure 6.3 Transmission for 1.7-μm-radius single MRR coupled to straight 0.3-μm-wide waveguides

From this figure, the localised resonance wavelengths, and corresponding quality factor are listed in Table 6.1

Table 6.1 Resonance data from figure 6.3 for 3.4 μm-diameter MRR and w = 0.3 μm

m	F (THz)	λ_{res}(nm)	Q
18	181.2	1655.62	1295
19	190.3	1576.45	1455
20	199.4	1504.51	3098
21	208.5	1438.84	2937
22	217.6	1378.67	3680

The quality factor of the m^{th} resonance is calculated directly from the spectrum as the

ratio of the resonance wavelength (λ_{res}) to the width of the resonance peak ($\Delta\lambda_{res}$) at half-power.

6.2.2.2 Calculation of Free Spectral Range

The variation of resonance wavelength with corresponding coupling coefficients and wave number is illustrated in figure 6.4.

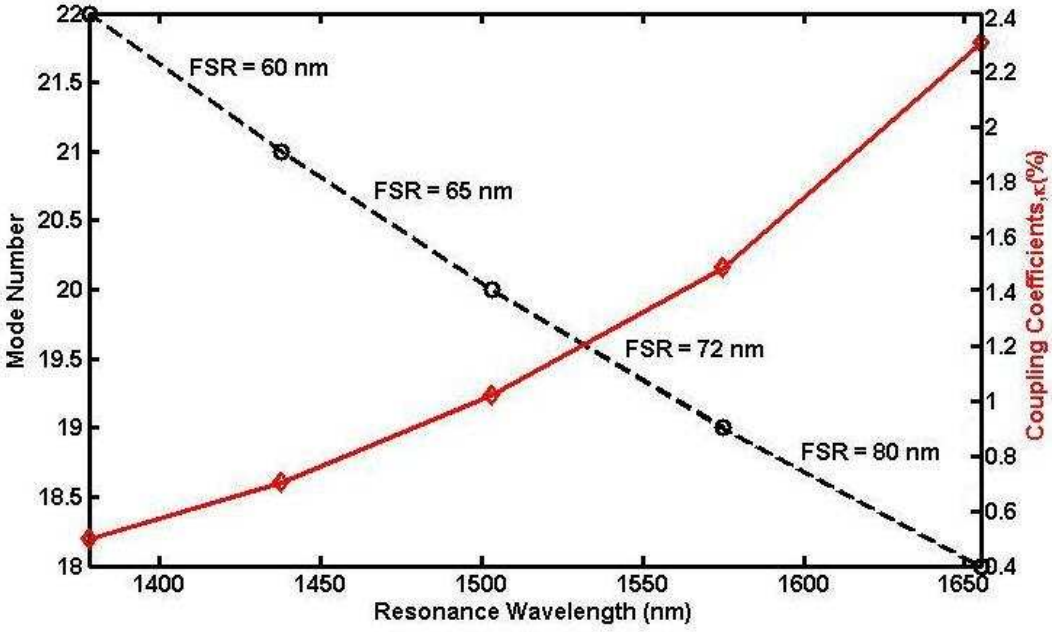

Figure 6.4 Variation of mode number and coupling coefficients with resonance wavelength of 3.4-μm-diameter MRR (w = 0.3μm)

It may be observed that the coupling coefficients significantly increase towards higher wavelength as a result of the corresponding decrease the effective refractive index. The free spectral range which is defined as the spacing between two adjacent resonant wavelengths ranges from 60 nm to 80 nm. Due to strong demand of WDM applications

requiring single-channel selectivity and a high number of channels in the transparency range of optical fibre, the FSR needs to be larger than 30nm.

6.2.2.3 Influence of air gap width on Extinction ratio

The extinction ratio, also called on/off ratio, represent the ratio of the transmitted power to the not transmitted power. As can be seen from figure 6.5, the rejection ratio can be altered by varying the gap size.

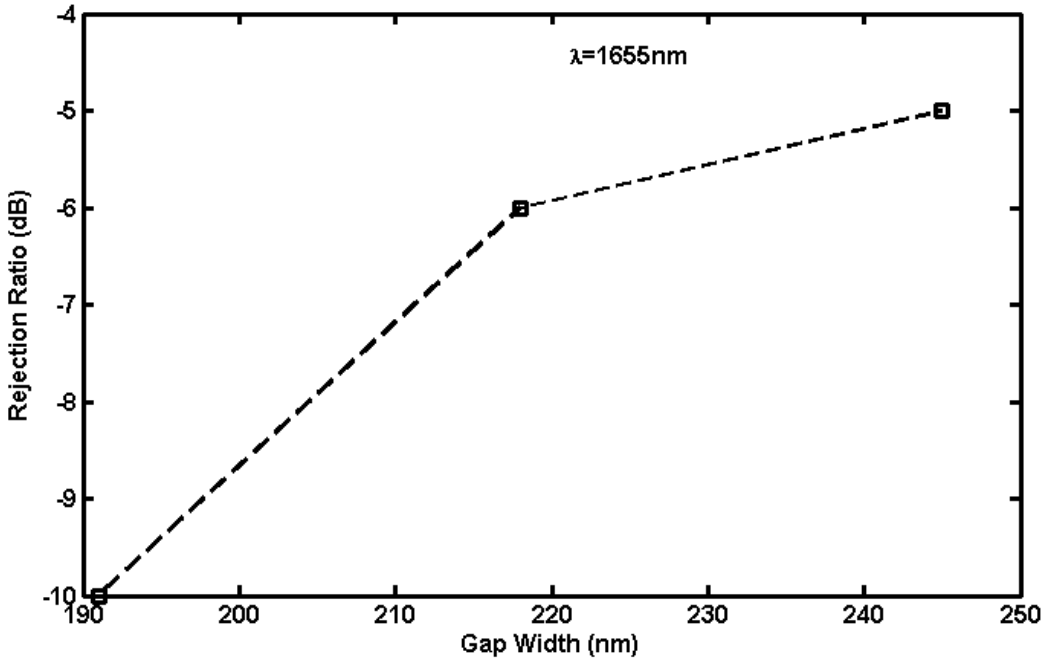

Figure 6.5 Variation of rejection ratio with gap width at λ_{res} = 1566 nm of 3.4-μm-diameter MRR (w = 0.3μm)

Adopting a smaller gap size could improve the rejection ratio related to a specific resonance mode and minimise the cross talk [10]. However, a small gap size brings also the resonance field to be less strongly confined inside the Ring, decreasing the quality factor. In some applications such as biomedical sensors where extremely narrow dips of

transmitted intensity in the frequency spectrum is required, the quality factor of the cavity needs to be high enough [21]. Therefore, in order to increase the rejection ratio, without compromising the performance in terms of quality factor, a double parallel MRR (PDMRR) is suggested.

6.3 Simulation Results of PDMRR

The structure, shown in figure 6.6, consists of two ring resonators centred between two straight waveguides. The structure parameters are chosen as following: the diameter of the two rings is d = 3.4µm, core and cladding have refractive indices of n_{core} = 3.2 and n_{cl} = 1, respectively, the width of the ring and straight waveguides is w = 0.3µm, and gap width (g_1 = g2) between the outer ring and straight waveguides is set to be 218nm.

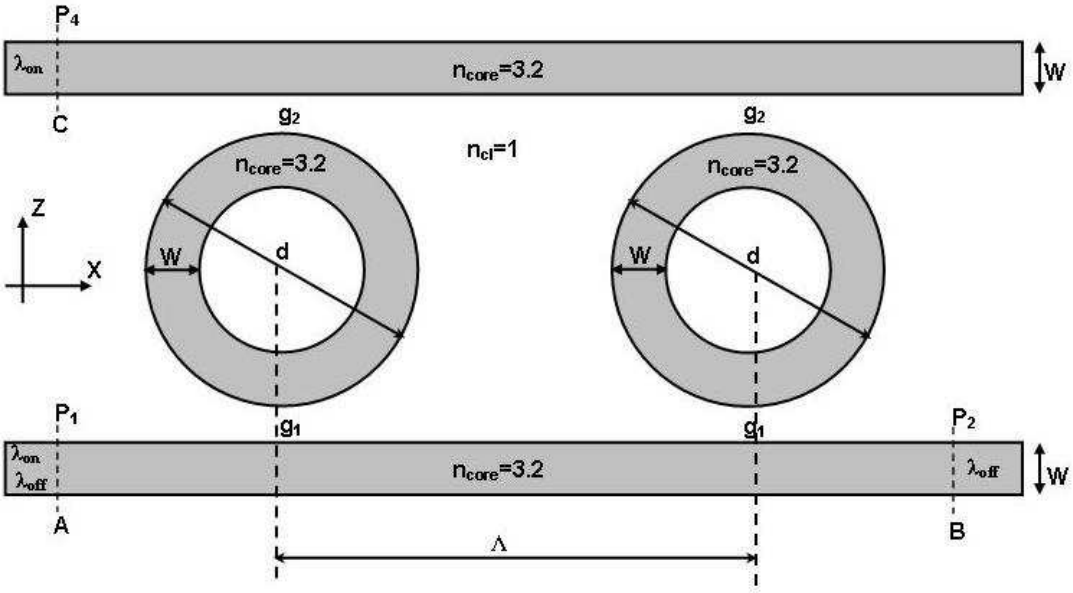

Figure 6.6 Schematic diagram of the 2-D PDMRR of diameter d = 3.4µm coupled to two straight waveguides where n_{core} = 3.2, n_{cl} = 1 and width, w = 0.3µm (Λ = 10µm).

The structure is excited in the same manner as in the single ring case. The distance from centre to centre of the two rings Λ is set to 10 µm. The transmission characteristics obtained from the analysed PDMRR is shown in figure 6.7.

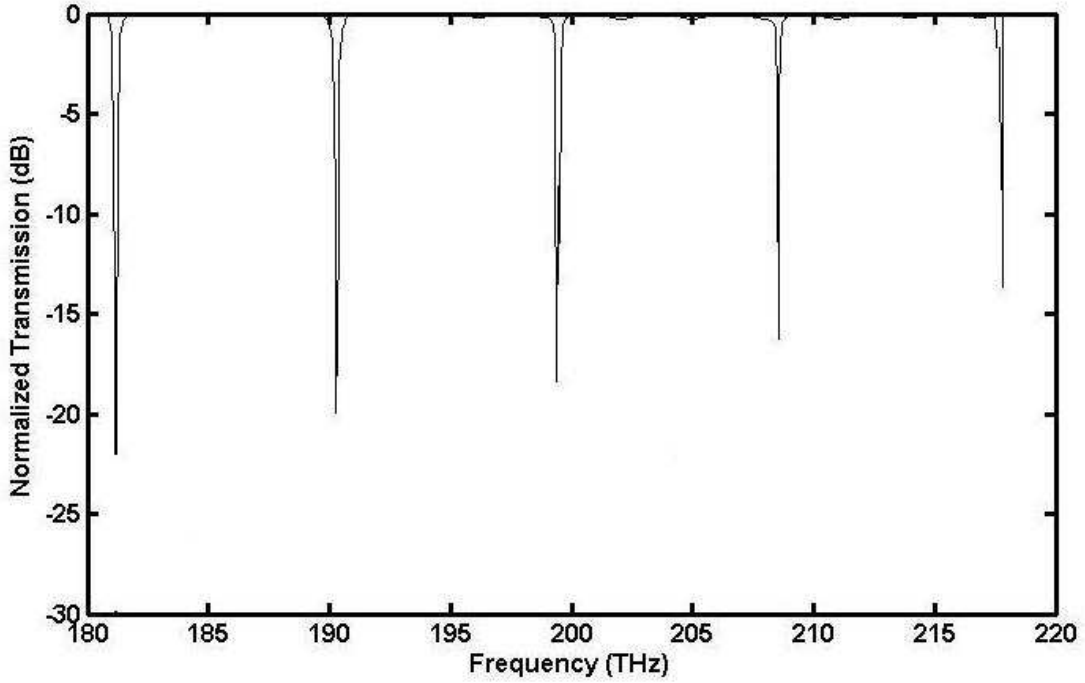

Figure 6.7 Transmission for 1.7-µm-radius PDMRR coupled to straight 0.3-µm-wide waveguides with Λ = 10 µm

The localised resonance wavelength is extracted and the quality factor of the m^{th} resonance is calculated directly from the spectrum following the same procedure as in the single ring case. The numerical results are listed in Table 6.2.

Table 6.2 resonance data from figure 6.7 for 3.4 μm-diameter PDMRR and w = 0.3 μm

m	F (THz)	λ_{res}(nm)	Q
18	181.2	1655.62	1242
19	190.3	1576.45	1312
20	199.4	1504.51	2819
21	208.5	1438.84	3284
22	217.6	1378.67	3666

As shown in this table, if compared to the single MRR case, no significant change is revealed in terms of quality factor, whereas the extinction ratio at the resonant wavelengths is approximately 20 dB.

Figure 6.8 shows the electric field pattern recorded as results of the simulation. The PDMRR is excited with a sinusoidal continuous wave at wavelength 1655.62 nm (180.2 THz) until the steady state is reached.

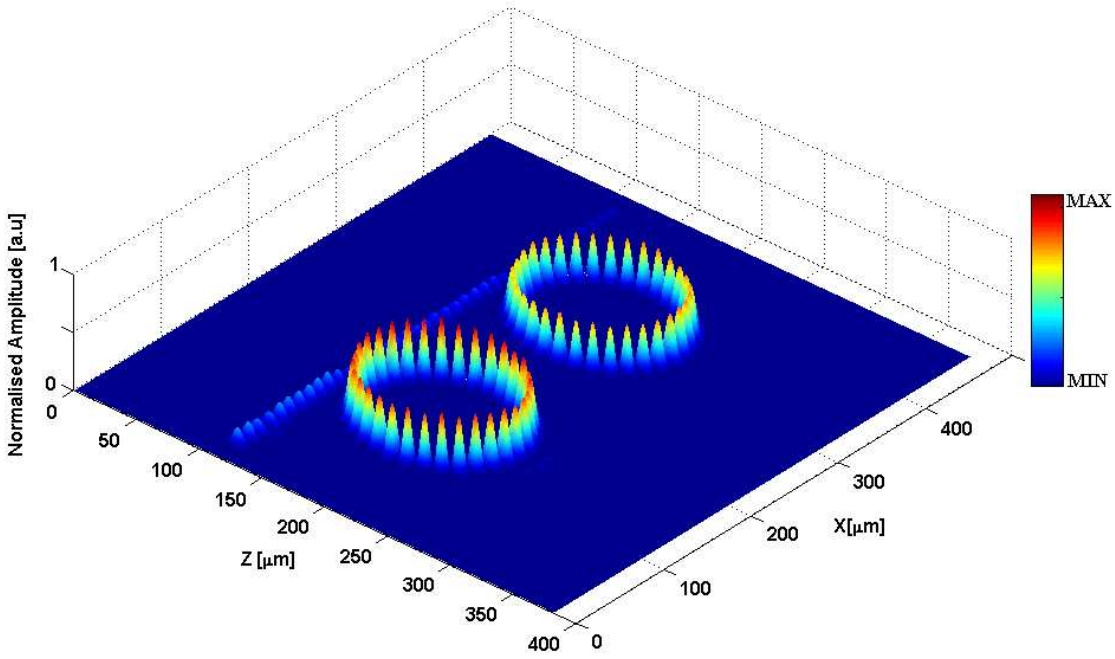

Figure 6.8 Sinusoidal steady-state amplitude distributed in 1.7-μm-radius PDMRR coupled to straight 0.3-μm-wide waveguides with Λ = 10 μm: on-resonance case at 1655.62nm

As it can be seen in this figure, being the source frequency one of the resonance modes of the structure, nearly 100% of the power is switched to the cavities and from them coupled to the other waveguide (on-resonance case).

In the same manner, the steady state E-field is computed for the case off-resonance at wavelength 1615.50 nm (185.7THz) and the resulting field pattern is illustrated in figure 6.9.

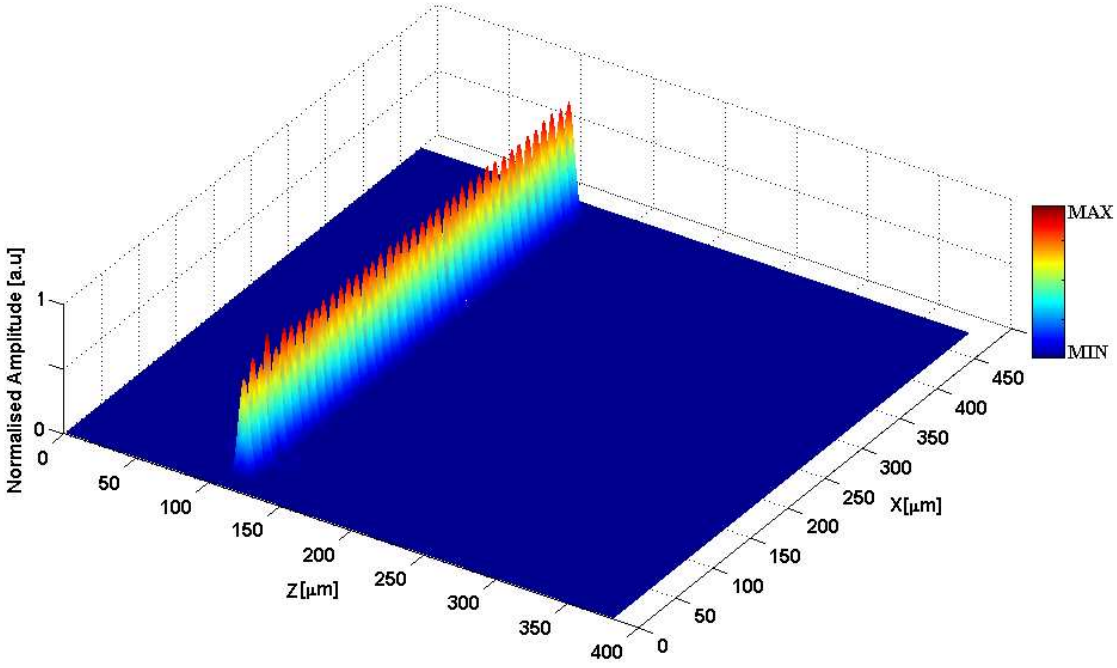

Figure 6.9 Sinusoidal steady-state amplitude distributed in 1.7-µm-radius PDMRR coupled to straight 0.3-µm-wide waveguides with Λ = 10 µm: off-resonance case at 1615.50 nm

As shown in this figure, no coupling occurred between the input waveguide and the cavities and nearly 100% of the signal is transmitted at port B.

6.3.1 Influence of air gap width on the coupling and Quality factor

The effect of changes in the gap size between input/output waveguides and the ring is considered focusing in particular on quality factor. Two types of changes of g_1 and g_2 are discussed. In the first case, both gap sizes are identically changed (g_1 = g2 = 245nm), while in the second one they are asymmetrically varied (g_1 = 245nm and g_2 = 191 nm). The distance between two rings is set to Λ = 10 µm in both simulations. Figure 6.10 show the numerical result obtained from the two cases of symmetrical gaps and

asymmetrical gaps on quality factor.

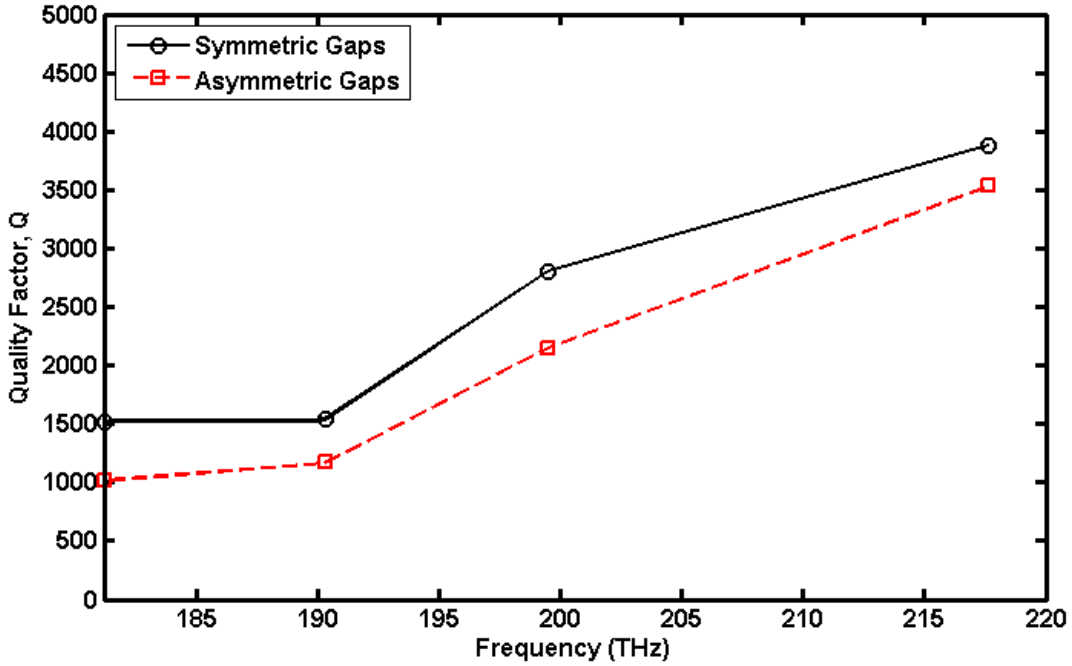

Figure 6.10 Variation of Quality factor Q with frequency for symmetric and asymmetric gap size g_1 and g_2 for 1.7-µm-radius PDMRR coupled to straight 0.3-µm-wide waveguides with Λ = 10 µm

From figure 6.10, it can be noted that as expected, in both cases, the Quality factor increases at the highest frequencies where the coupling coefficients is lower. However, comparing the two curves obtained, it can be understood that by allowing a smaller gap size g_1, the amount of power coupled to and from the rings is varying compared to the symmetric gap case, and thus, the quality factor in this case has degraded. While the increase of quality factor towards high frequencies is not as much dramatic as for g_2 = 245nm.

6.3.2 Influence of air gap width on the coupling and rejection ratio

The consequence of alters in the gap size between input/output waveguides and the ring is considered spotlighting in particular on rejection ratio. Two kinds of changes of g_1 and g_2 are discussed. In the first case, both gap sizes are identically changed (g_1 = g2 = 245nm), while in the second one they are asymmetrically varied (g_1 = 245nm and g_2 = 191 nm). The distance between two rings from centre to centre is set to Λ = 10 µm in both simulations. The comparison between these two structures in terms of rejection ratio is reported in figure 6.11.

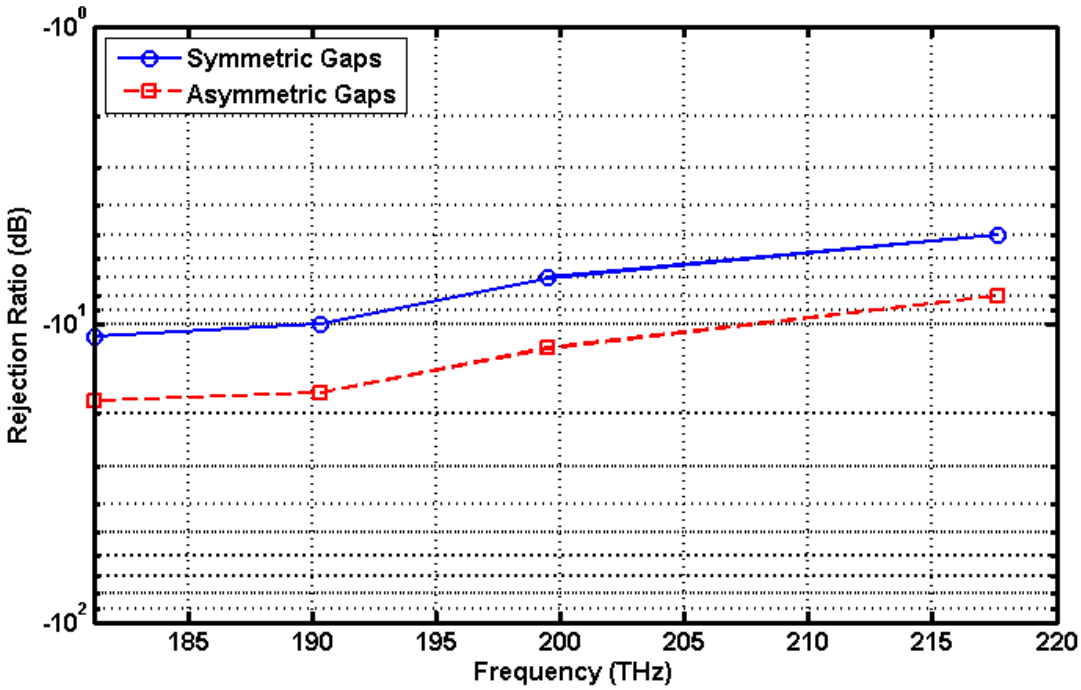

Figure 6.11 Variation of rejection ratio with frequency for symmetric and asymmetric gap size g_1 and g_2 for 1.7-µm-radius PDMRR coupled to straight 0.3-µm-wide waveguides with Λ = 10 µm

Figure 6.11 shows the numerical result obtained from the two cases of symmetrical gaps and asymmetrical gaps on rejection ratio. From this figure, it is clear that the choice of

asymmetrical gap size leads to an improved rejection ratio over all the resonance modes in the considered range. It can also be noted that this improvement is particularly significant for the lowest frequencies with an increase of about 60% compared to the symmetrical gap size case.

6.4 Summary

In this chapter, optical microcavity ring resonator based on high-index-contrast waveguide has been analysed by using MRTD formulation based on CDF (2, 4) scaling function and rigorous UPML boundary conditions. The approach has proved a good level of accuracy in extracting and studying the resonance behaviour of this structure. The optimisation of a number of important parameters, including coupling coefficients, quality factor, and rejection ratio has been discussed. A high-order structure consisting of a two ring resonators in parallel with centre distance of 10 μm has shown interesting potential in increasing the on-off ratio where it is desirable to minimise the cross talk of the device. Furthermore, by using asymmetric gap sizes, the rejection ratio of the device has significantly increased of about 60 %, compared to the best result as in the symmetric gap size case.

Chapter 7

Slotted Microcavity Ring Resonators

(SMRRs)

7.1 Introduction

In recent years, a great deal of research has been dedicated to optical slotted waveguides as they were found to be very attractive and promising for future of modern photonic devices. The devices include optical microring resonators separating two waveguides such that input signals propagate along the input waveguide, couple into the ring resonator and then sent to output waveguide, for certain wavelengths, at selected output port. The improved numerical accuracy provided by MRTD scheme is successfully applied to the analysis of slotted ring resonators. In this type of structures, coupling coefficients and resonant mode quality factor depend very much on the geometrical characteristics of the coupled microring. The effect of different parameters such as slot position, slot width, and slot filling material on the resonance modes and transmitted/coupled power is thoroughly investigated.

7.2 Background

The single microring resonator is one of the most important building blocks for more complicated nano-waveguide based structures which can support slow light operations, [26, 40, 49, 59, 69, 85]. These structures consist of periodic spaced resonators with or without inter-coupling, such as single-channel side-coupled integrated spaced sequence of resonators (SCISSOR), double channel SCISSORs and inter-coupled resonators [6, 21, 22, 35, 41 50]. Thanks to the recent advances in material technology and fabrication techniques, MRRs with physical dimensions comparable to optical wavelength have been made possible to be fabricated with negligible bending loss [10, 79]. Particularly, MRRs based on high-index-contrast material systems, such as Si/SiO_2 or Si/air, has

enabled the implementation of highly integrated photonic structures [10, 102]. In these structures, the light tends to be strongly confined and guided within the core region by means of total internal reflection [84].

However, despite the high-index contrast between core and cladding, the guiding within the core region can still be problematic for some applications. For instance, two-photon absorption in silicon at very high optical intensities may cause high optical losses [60]. Recently work proposed by Almeida et al. shows that the use of slotted waveguide for all-optical data processing such as all-optical switches is one of the most promising applications of this new design technology [103].

It is known that in a slotted waveguide, the electromagnetic field can be guided and strongly confined inside nanometric-scale region of low refractive index. This property stems from the discontinuity of the normal component of electric field across material interference. Thus, strong field can significantly boost the resonance field enhancement [53].

Thus, slotted waveguide and slotted resonator systems are expected to play vital role in developing a novel platform for high-performance integrated optics. Due to the nature of this research, and the many attributes of slotted waveguides in channelling electromagnetic waves, this slotted waveguides have been heavily investigated for the purpose of designing, modelling, and simulating switching devices that are highly efficient in transmission and tightly compact in design.

7.3 Slotted Ring Resonator Cavity

7.3.1 SMRR filled with SiO_2

The two-channel ring resonator based on slotted waveguide filled with SiO_2 whose schematic diagram is shown in figure 7.1, with ring diameter d = 5µm and total width w_{total} =709 nm.

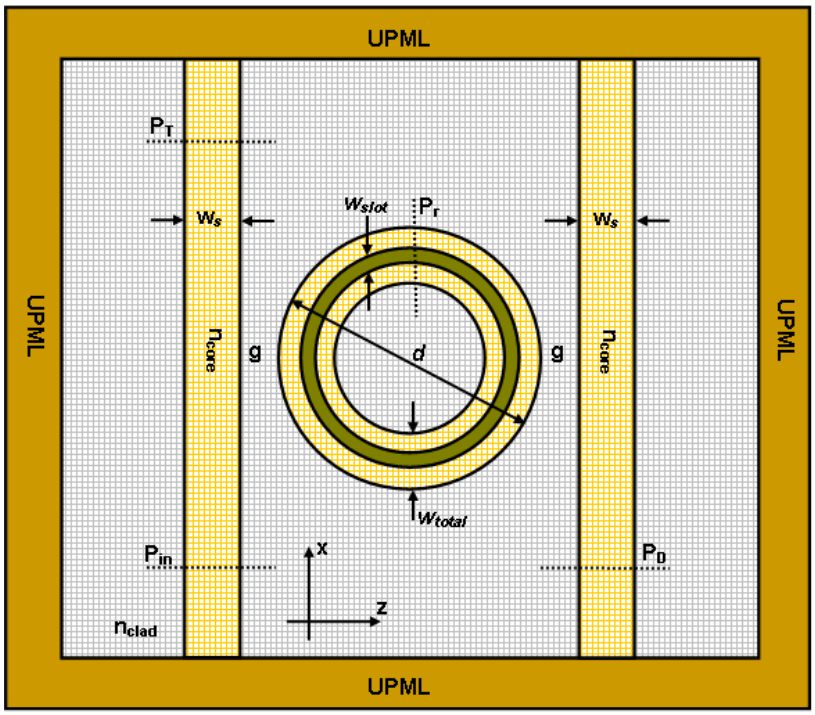

Figure 7.1 Schematic diagram of the 2-D single SMRR of diameter d = 5µm filled with SiO_2 coupled to two straight waveguides where n_{core} = 3.2, n_{clad}=1, and n_{slot} = 1.47

The core is made of silicon with refractive index of n_{core} = 3.2 and is micro-structured to exhibit a slot of width w_{slot} with refractive index n_{slot}=1.47. The SMRR is coupled to two identical straight silicon waveguides that are w_s = 0.3 µm wide. The minimum separation distance between the two bus waveguides and the ring resonator is g = 0.245 µm. The entire device is placed in an air background. The structure is discretised into a uniform

mesh with cell size $\Delta_x = \Delta_z = \Delta = 27.25$ nm and is terminated by 20-cell UPML to absorb the reflected power. In order to cover the spectrum of interest in just one-go simulation, the structure is excited with a Gaussian pulse modulated in time by a sinusoidal function with the shape of the fundamental mode profile of the waveguide as [82]

$$E_y(z,t) = E_0(z)e^{-((t-t_0)/T_0)^2}\sin(2\pi ft) \tag{7.1}$$

where $E_0(z)$ represents the fundamental mode profile of the waveguide, t_0 and T_0 are the time delay and the time width of the Gaussian pulse fixed at 80 fs and 20 fs respectively, and f is the central frequency which is set at 200 THz ($\lambda = 1.5\mu m$).

As shown in Fig. 7.1, different cross-sections are chosen in order to record the time domain variation of incident, transmitted, and reflected fields. By means of Fast Fourier Transform (FFT) of the recoded time-dependent fields, the coupled power P_r and the transmitted power P_t are calculated by dividing the coupled and transmitted spectra by incident power P_{in}.

7.3.1.1 Influence of slot width and slot position on the coupling efficiency

In this section, the effect of changes in the slot position on the coupling performance of the entire resonator is presented for three types of changes of slot position as shown in figure 7.2.

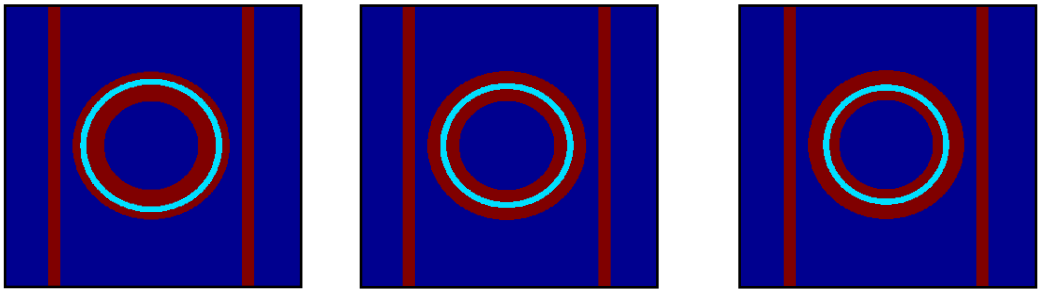

Figure 7.2 From left to right, the slot position corresponding to η=0.7, η=0.5, and η=0.4 respectively filled with SiO_2

The slot's location in the ring is expressed by the asymmetry parameter, η, such that the inner width of high-index ring layer is η*w* and that of outer high-index ring layer is (1-η)*w*, where $w = W_{total} - W_{slot}$.

Firstly, the variation of coupling efficiency, κ, with frequency for different slot positions and widths, w_{slot}, is shown in figure7.3.

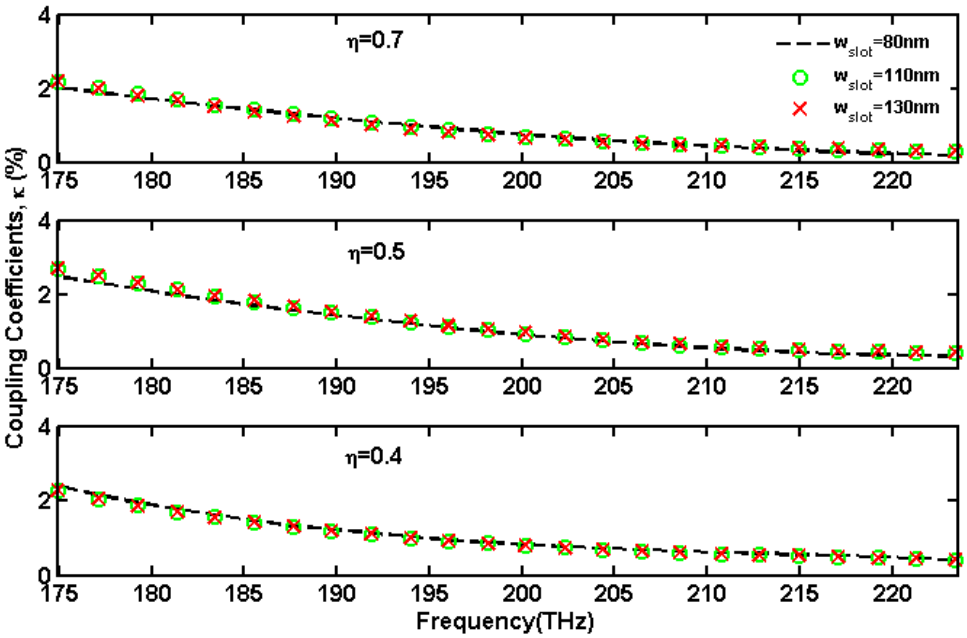

Figure 7.3 Variation of coupling coefficients κ with frequency and slot width for three different SiO_2 slot positions of SMRR.

From figure 7.3, it can be seen that the coupling coefficients which determine the amount of power coupled to/from the ring resonator are quite sensitive to the slot position within the ring. This can be explained as a result of the corresponding increase or decrease of the effective refractive index which is a function in the waveguide width. It can be also noted that the influence of the slot thickness w_{slot} on the coupling efficiency is rather small over wide range from 80 to 130 nm for all studied widths, and therefore, its value has been fixed at 130 nm throughout the rest of the thesis. In addition, at fixed slot position, the coupling efficiency is significantly decreased towards higher frequencies. With the purpose of achieving good transmission characteristics and large extinction ratio, the amount of power coupling form the input waveguide to the slotted ring resonator should be equal to the amount of power coupled form slotted ring to the output waveguide. Therefore, the variation of the coupling coefficients is considered for different slot position as shown in figure 7.4.

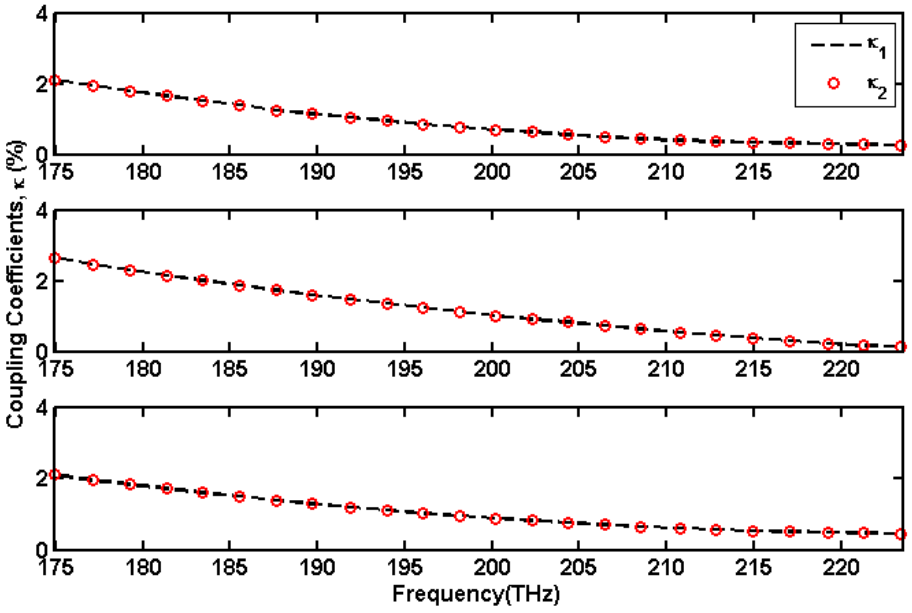

Figure 7.4 Variation of coupling coefficients κ with frequency and slot width for three different SiO_2 slot positions of SMRR.

The result obtained in figure 7.4 reveals that symmetry property of the input/output coupling process is fulfilled. A conventional way to increase the resonance effect inside the conventional MRR is to increase the distance between ring and coupled waveguides towards higher values of g or reducing the ring waveguide width [103]. However, from figure 7.4, it can be seen that the use of a slotted configuration allows varying of the coupling coefficient in the range of interest by merely acting on the slot position η.

7.3.1.2 Influence of slot position on the spectral response

For every MRR-based structure, an increase in the coupling coefficient causes the resonance field to be less strongly confined inside the ring, decreasing the quality factor. Suitable coupling coefficients therefore, can be chosen as a compromise between transmittivity and Q-factor. In order to understand how the dependence of Q on the coupling coefficient differs in the slotted configurations compared to the conventional MRR case, the transmission at throughout port for SiO_2 SMRR for different slot positions is considered here.

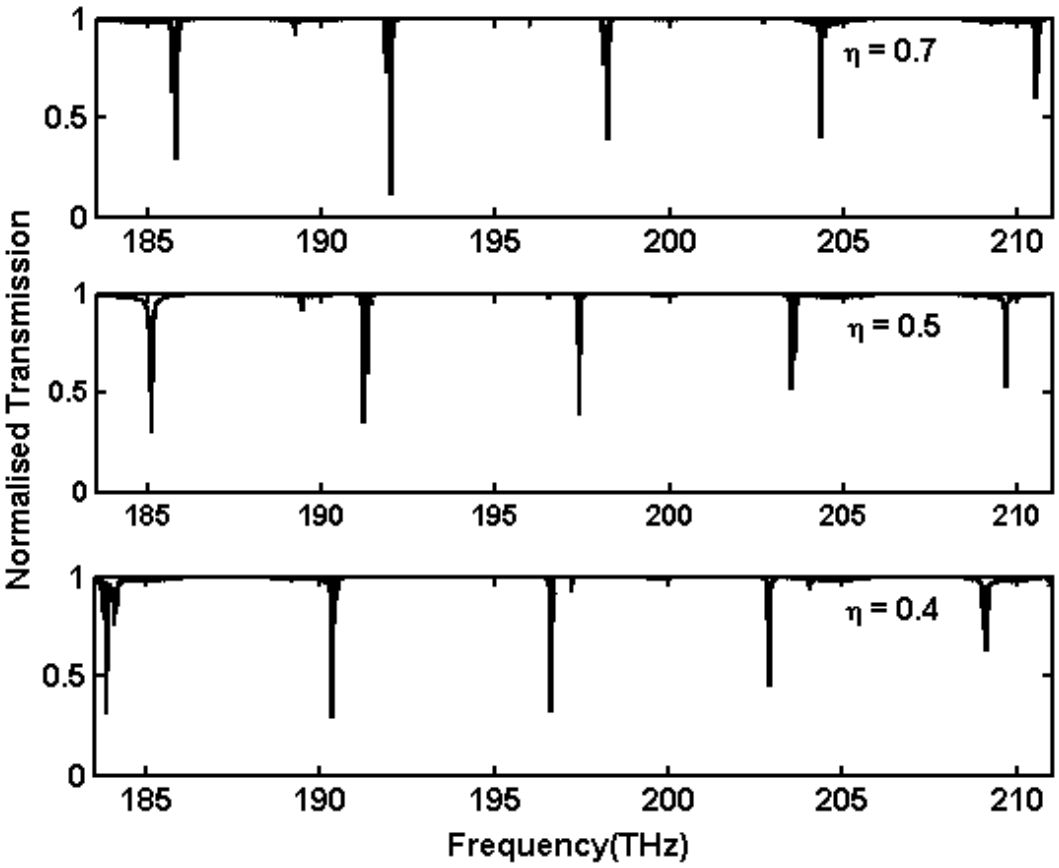

Figure 7.5 Spectral transmission for 5-μm-radius SiO_2 slotted ring resonator for different slot position.

The measured transmission spectrum of the slotted ring resonator filled with SiO2 around $\lambda = 1.55$ μm is presented in figure 7.5. From this Figure, the localised resonance wavelengths, and quality factor Q are calculated and listed in Table 7.1. The quality factor of the m^{th} resonance is calculated directly from the spectrum as the ratio of the resonant wavelength (λ_m) to the width of the resonance peak ($\delta\lambda$) at half-power.

Table 7.1 Resonance data from figure 7.5 for SMRR filled with SiO_2, g = 0.245 μm

η=0.4	λ_{res} (nm)	1629.54	1576.45	1523.61	1478.56	1434.72
	Q	2671	3505	3809	3996	3985
η=0.5	λ_{res} (nm)	1620.74	1569.03	1519.75	1474.20	1430.61
	Q	2133	4241	3897	4914	4335
η=0.7	λ_{res} (nm)	1614.63	1562.50	1513.62	1467.71	1425.17
	Q	4892	5388	5045	4892	5278

As shown in Table 7.1, there is change in the resonance positions, here defined as the wavelengths corresponding to the maxima in the transmitted and dropped power. It can also be seen that the use of a slotted configuration, filled with SiO2, allows varying the coupling coefficient and the quality factor at every resonance frequency in the range of interest by merely acting on the slot position η.

It should be noted that the effective refractive index will be different at each resonance wavelength. This is due to the resonance modes for a small ring cavity which are spaced far apart [65]. These are clearly shown in figure 7.6 where a number of important results can be observed. Firstly, as the slot position changes, each resonance is shifted towards shorter wavelength. Secondly, the wavelength decreases with the effective refractive index and the FSR decreases as the wavelength decreases.

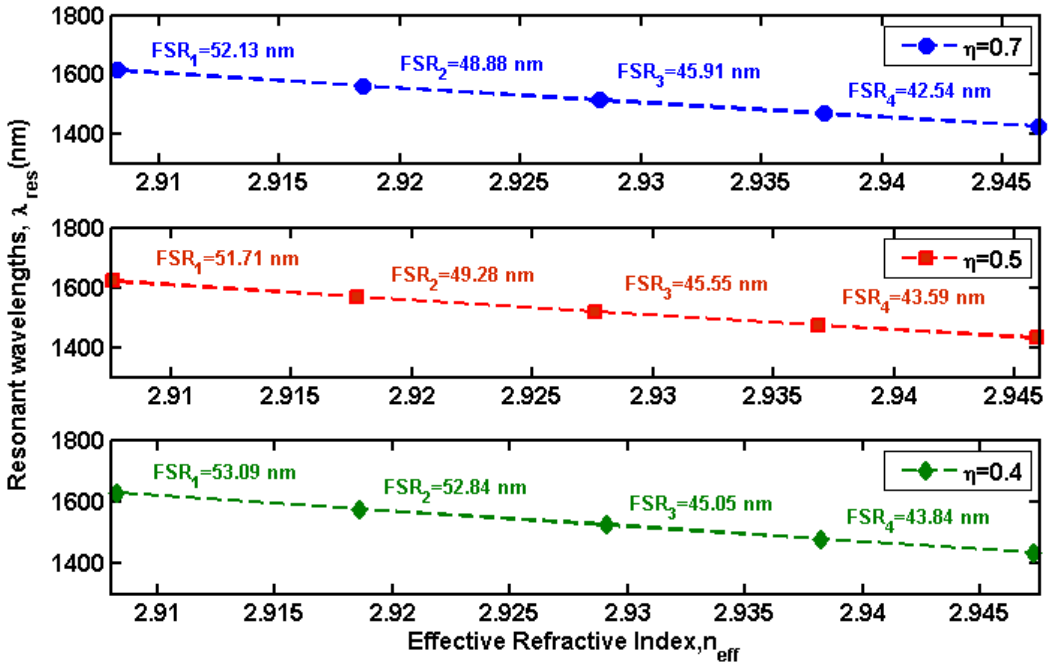

Figure 7.6 Free spectral range of 5μm-diameter SiO_2 slotted microcavity ring resonator as a function of effective refractive index and slot position

7.3.1.3 Influence of slot position on the finesses

The finesse is calculating by forming the ratio of free spectral range, FSR, to the width of the resonance, Δ_λ, at the half-power points. Table 7.2 compare the range of the obtained finesses for each slot position.

Table 7.2 the calculated finesses for different slot position of SMRR filled with SiO_2, g = 0.245 μm

Slot Position	Range of Finesse
η=0.7	142-180
η=0.5	68-152
η=0.4	87-132

It is clear that the finesses can be altered by varying the position of the slot inside the ring and according Table 7.2 high finesses can be achieved for η = 0.7 where the finesses ranges between 142 and 180.

The variation of the finesses with the intensity attenuation coefficients of the ring is illustrated in figure 7.7.

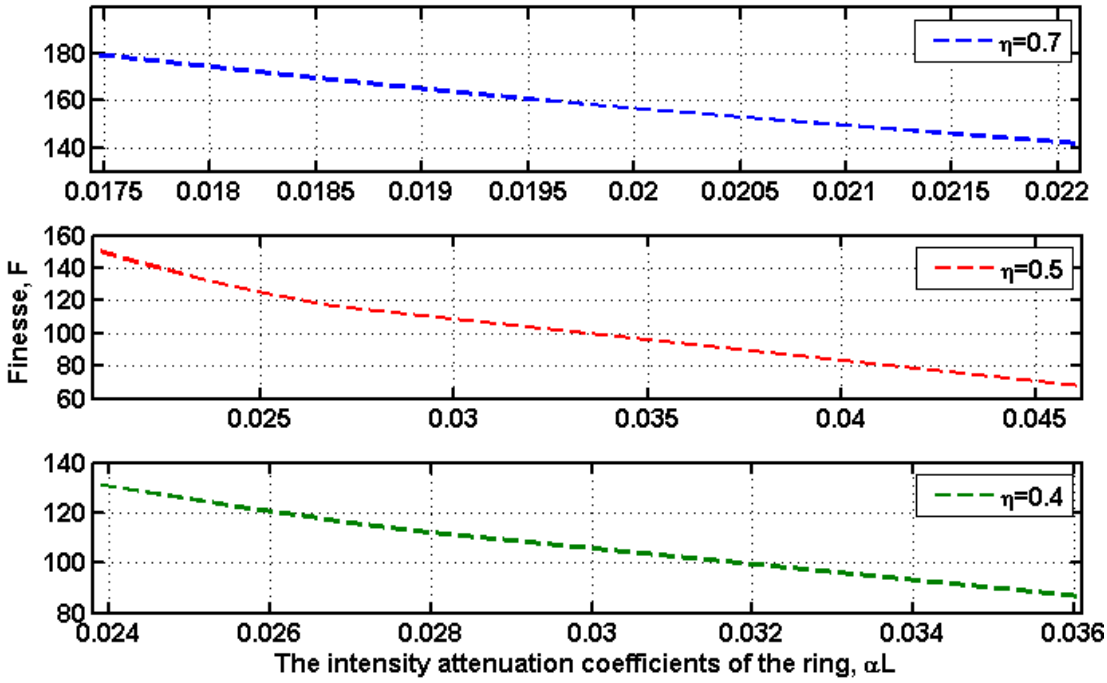

Figure 7.7 Variation of finesses with the intensity attenuation coefficients for three different slot positions of SiO_2 SMRR.

From this figure, it can be seen that the finesse decreases as the intensity attenuation coefficients of the ring increases. This can be explained by the higher internal losses associated with each round trip inside the ring.

7.3.1.4 Influence of slot position on the inner circulation factor

Next, the variation of inner circulation factor with the intensity attenuation coefficients of the ring is considered here. The performance in terms of inner circulation factor, as shown in figure 7.8, clearly indicates that at higher intensity attenuation coefficients, the inner circulation factor rapidly decrease which in turn lead to increase the internal losses inside the ring.

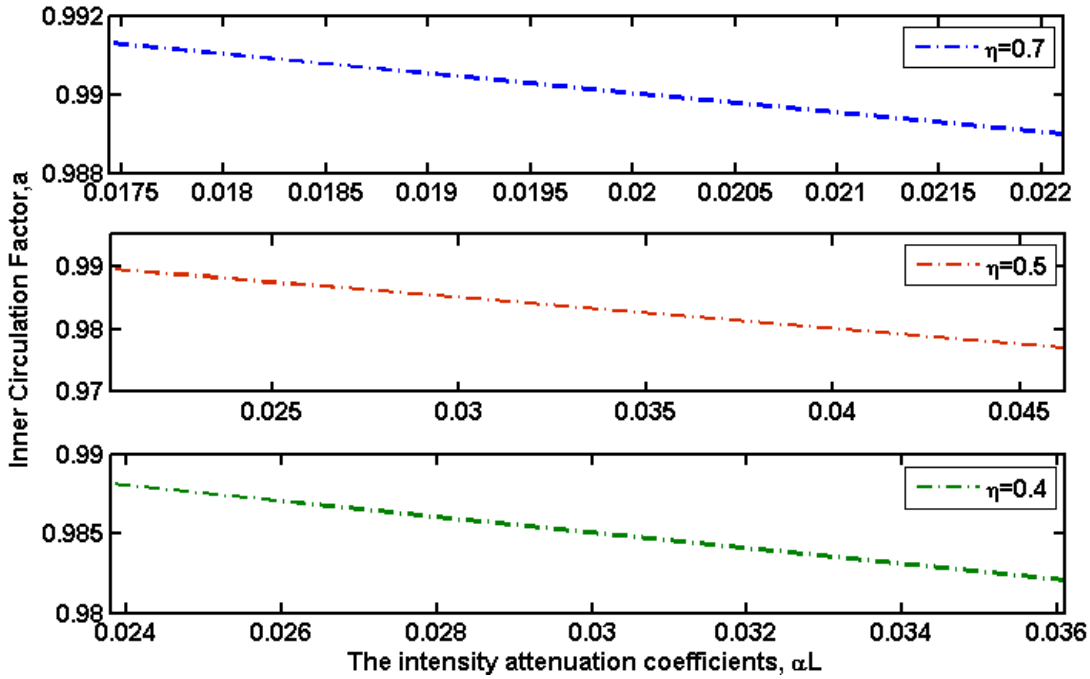

Figure 7.8 Variation of inner circulation factor with the intensity attenuation coefficients for three different slot positions of SMRR filled with SiO_2.

Again, high inner circulation factor can be accomplished for $\eta = 0.7$ which means lower internal losses.

7.3.2 SMRR filled with Air

In the second test, the slot position again varied, but this time, the material filling the slot ring was changed to be air instead of SiO_2 as shown in figure 7.9.

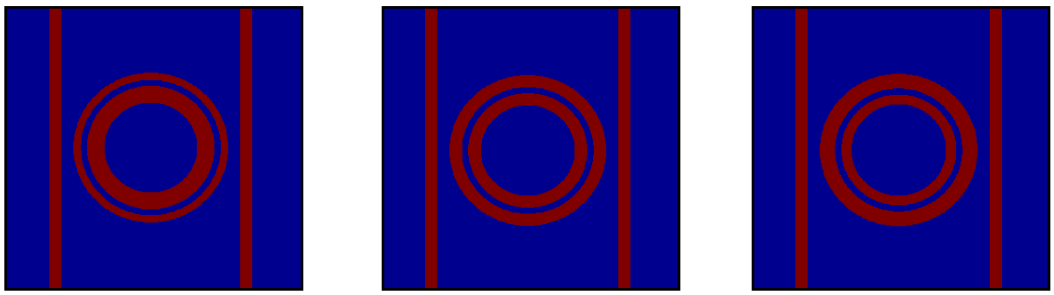

Figure 7.9 From left to right, the slot position corresponding to η=0.7, η=0.5, and η=0.4 respectively filled with air

Again, the ring diameter d = 5µm and total width W_{total} = 0.709 µm. The core is made of silicon with refractive index of n_{core} = 3.2 and is micro-structured to exhibit a slot of width W_{slot} with refractive index n_{slot} = 1. The slotted ring is sandwiched between two identical straight silicon waveguides of w_s = 0.3 µm wide.

The minimum separation distance between the two bus waveguides and the ring resonator is g = 0.245 µm. The entire device is placed in an air background as illustrated in figure 7.10. The structure is discretised in the same manner as explained in the previous section. Then, the same Gaussian pulse modulated in time by a sinusoidal function with the shape of the fundamental mode profile of the waveguide was inserted into structure.

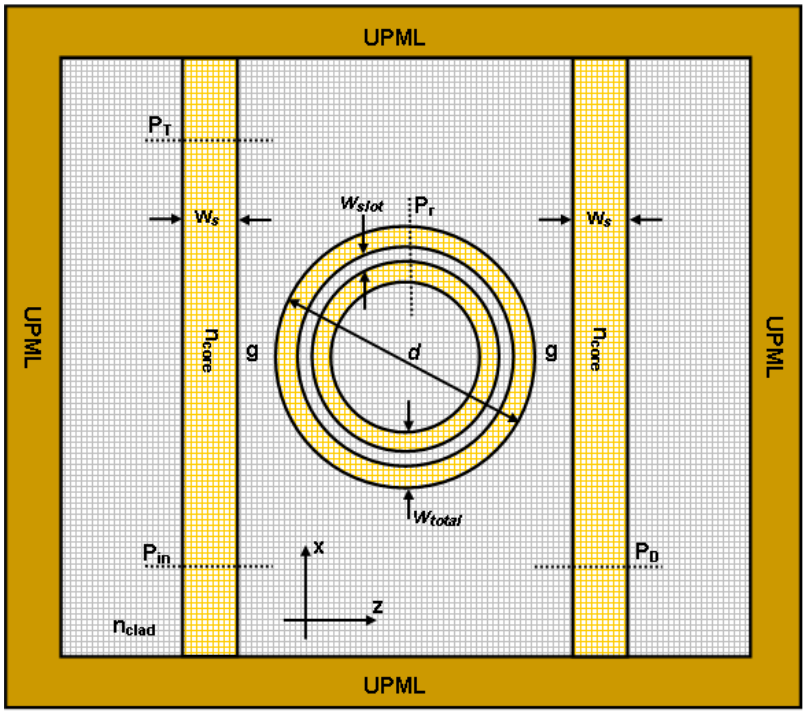

Figure 7.10 Schematic diagram of the 2-D single SMRR of diameter *d*=5µm filled with air coupled to two straight waveguides where $n_{core} = 3.2$, $n_{cladcl} = 1$, and $n_{slot} = 1$

7.3.2.1 Influence of slot position on the coupling and transmission efficiency

In this section, the consequence of altering the slot position on coupled and transmitted power of the entire resonator is presented for different slot position, $\eta = 0.7$, $\eta = 0.5$, and $\eta = 0.4$ respectively.

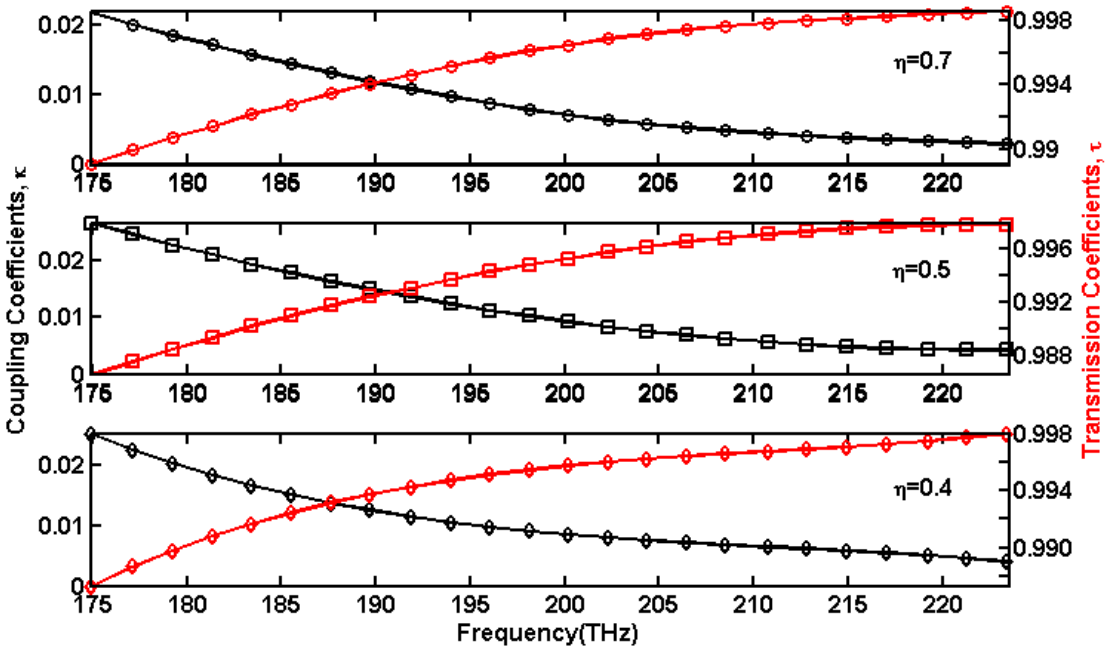

Figure 7.11 Variation of coupling and transmission coefficients with frequency for three different air slot positions of SMRR.

Figure 7.11 shows the performance, which is in terms of coupling and transmission efficiency, clearly indicates that at higher frequencies, the amount of power coupled to the ring resonator rapidly decrease while the transmitted power increases.

7.3.2.2 Influence of slot position on the spectral response

The optimisation approach taken in this study was to fill the slot with a material in order to better trap photons and enhance controlling the lightwave. Air slotted ring resonator was introduced so as to optimise the efficiency of the structure in terms of ratio of the output signal P_T to input signal P_{in}.

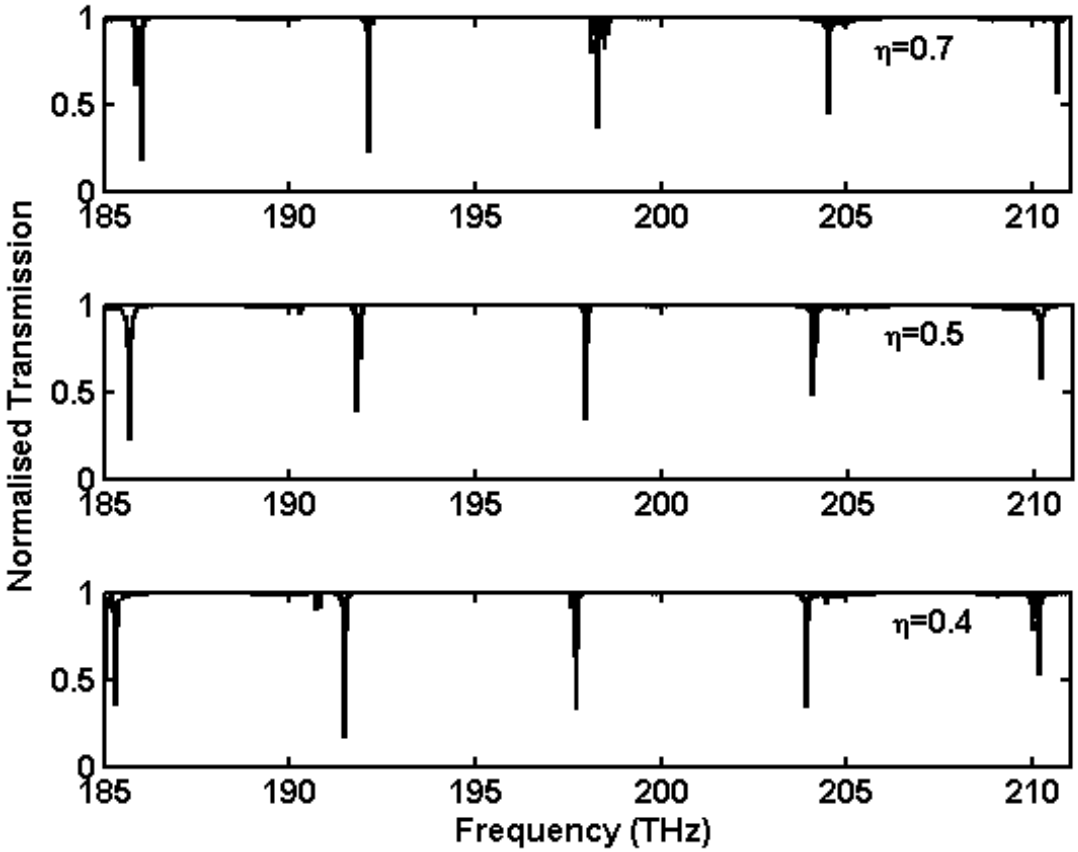

Figure 7.12 Spectral transmission for 5-μm-radius air slotted ring resonator for different slot position.

The measured transmission spectrum of the slotted ring resonator filled with air around λ = 1.55 μm is presented in figure 7.12. From this Figure, the localised resonance wavelengths, and quality factor Q are calculated and listed in Table 7.3. The quality factor of the m^{th} resonance is calculated directly from the spectrum as the ratio of the resonant wavelength (λ_m) to the width of the resonance peak ($\delta\lambda$) at half-power.

Table 7.3 Resonance data from figure 7.12 for SMRR filled with air, g =0.245 μm

η=0.4	λ_{res} (nm)	1620.74	1566.57	1517.45	1471.31	1427.89
	Q	4156	4747	4598	4204	5100
η=0.5	λ_{res} (nm)	1615.50	1563.31	1515.91	1469.86	1427.21
	Q	2785	4343	4890	5069	4904
η=0.7	λ_{res} (nm)	1613.77	1561.68	1513.62	1466.94	1424.50
	Q	5043	5577	5219	5059	6475

As shown in Table 7.3, there is also altering in the resonance positions. In addition, the use of a slotted configuration, filled with air, allows varying the coupling coefficient and the quality factor at every resonance frequency in the range of interest by merely acting on the slot position η.

The variation of resonance wavelength with corresponding effective refractive index is illustrated in figure 7.13.

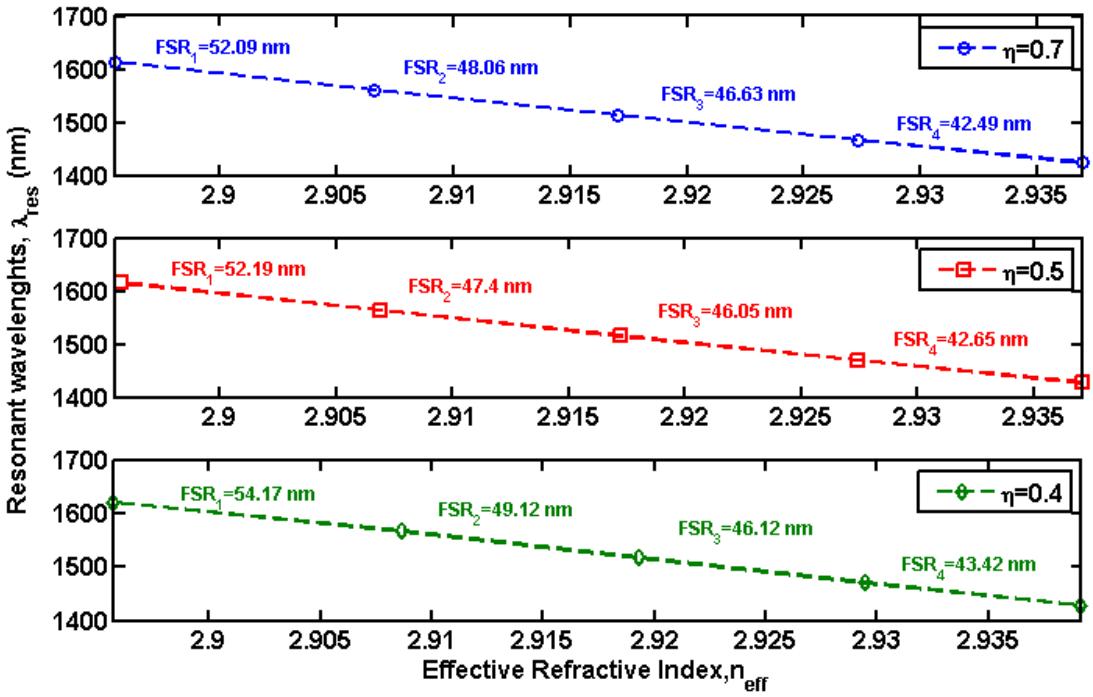

Figure 7.13 Free spectral range of 5µm-diameter air slotted microcavity ring resonator as a function of effective refractive index and slot position

It may be observed that the entity of FSR decreases as the wavelength decreases, the FSR also significantly decreases towards higher effective refractive index.

7.3.2.3 Influence of slot position on the finesses

The ratio of the two preceding quantities and measures the separation between the resonance dips is considered here. Table 7.4 compare the range of the calculated ratio for each position.

Table 7.4 the calculated finesses for different slot position of SMRR filled with air, g = 0.245 μm

Slot Position	Range of Finesse
η=0.7	146-193
η=0.5	90-159
η=0.4	124-164

From Table 7.4, it is observed that at all slot's position there is substantial improvements on finesses and optimum value is achieved for η = 0.7 where the finesses ranges between 146 and 193.

Figure 7.14 shows the variation of the finesses with the intensity attenuation coefficients of the ring.

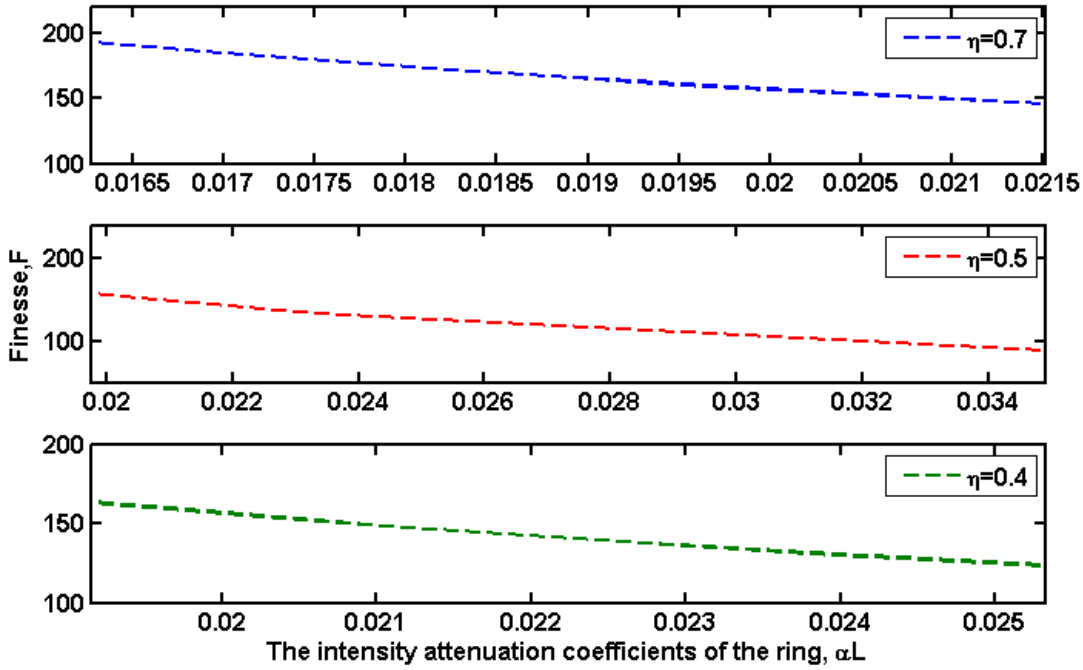

Figure 7.14 Variation of finesses with the intensity attenuation coefficients for three different slot positions of air SMRR.

It can be seen from this figure that the finesse decreases as result of increasing of the intensity attenuation coefficients of the ring due to roundtrip internal losses inside the ring.

7.3.2.4 Influence of slot position on the inner circulation factor

Figure 7.15 demonstrates the performance, which is in terms of inner circulation factor; obviously indicates that at higher intensity attenuation coefficients, the inner circulation factor rapidly decrease which in turn lead to increase the internal losses inside the ring.

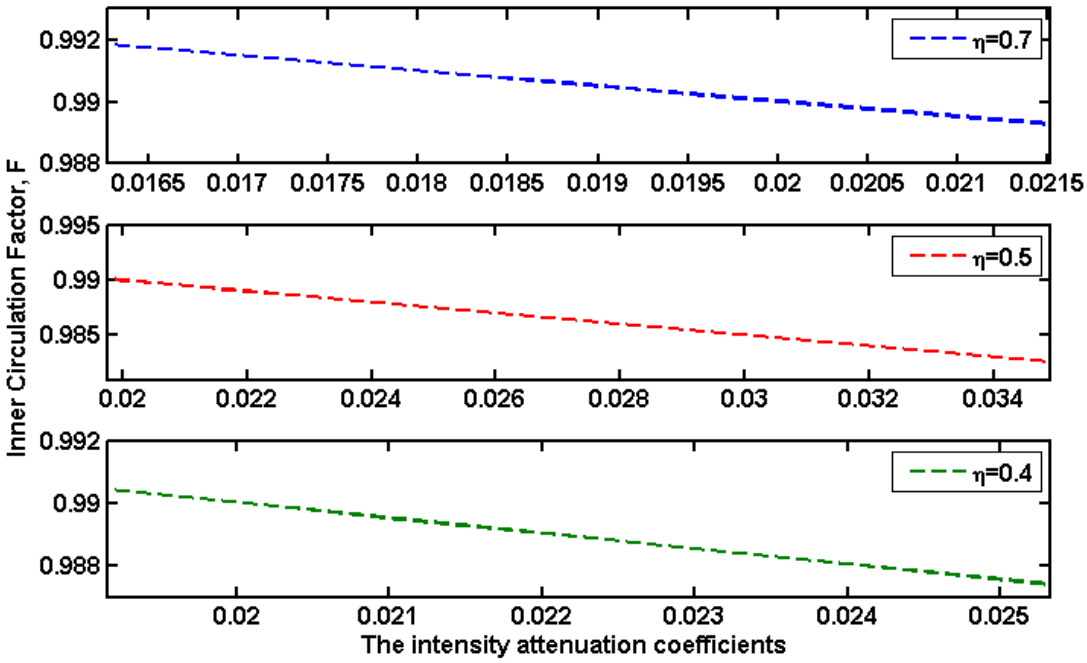

Figure 7.15 Variation of inner circulation factor with the intensity attenuation coefficients for three different slot positions of SMRR filled with air

7.3.2.5 Influence of slot position on the number of stored bits inside the ring

The variation number of stored bits with coupling efficiency for SMMR filled with SiO_2 is shown in figure 7.16 where the number of stored bits in the SMRR is calculated using [1]

$$N = \frac{2 - \kappa^2}{8 \ln(2)} \tag{7.2}$$

where κ is the coupling efficiency between the input waveguide and the ring.

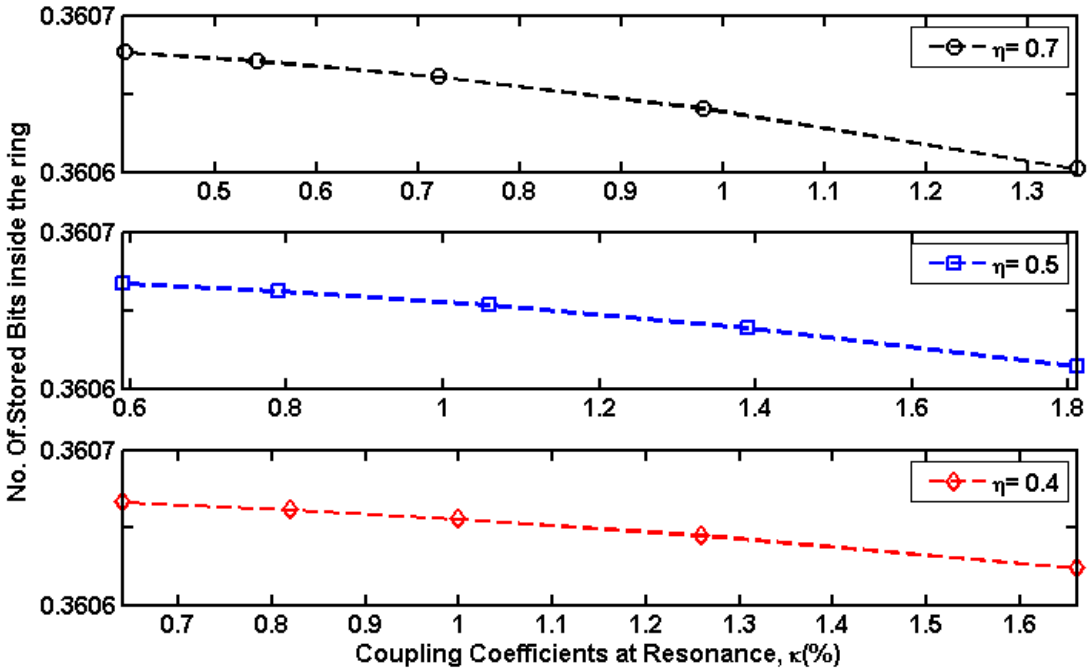

Figure 7.16 Variation of stored bits with coupling coefficients at resonance for three different slot positions of SMRR filled with air.

The variation number of stored bits with coupling efficiency for SMMR filled with air is shown in figure 7.16. It is apparent that for all values of coupling coefficients at resonance, the number of stored bits ranges between 0.3606 and 0.3607 and found to be in excellent agreement with the desired value which typically equal to 0.36 as reported in [1]. This result gives clear indication that delay elements based on this kind of resonators can play a significant role in quantum computing and optical signal processing which call for the need of efficient controlled delay elements with large characteristics storage time.

Table 7.5 below holds direct comparison between all three structures and their performance in terms of finesses and quality factor.

Table 7.5 Microcavity ring resonator structure performance comparison

Structure	Quality Factor at 1425 nm	Range of Finesses
Ring Resonator without slot	4008	117-162
Slotted ring resonator filled with SiO_2 (η=0.7)	5278	142-180
Slotted ring resonator filled with Air (η=0.7)	6475	146-193

From Table 7.5, it is observed that new design, that includes the inserted slot filled with air, is the optimum design, suppressing the other two competitive designs.

7.4 Summary

A new optical microcavity ring resonator with a single slot has been proposed to improve the performance in terms of coupling efficiency, finesses and quality factor. Since the variation of coupling efficiency, finesses, the internal losses, the quality factor, and the number of stored bits inside the ring with the slot design specifications, such as width, position, and material of the slot, has been thoroughly investigated and compared. The S-MRTD has been employed to analyse and optimise the performance of a new ring resonator based on slot waveguides. Results have revealed that the slotted configurations allow for an increased quality factor at fixed gap size between central ring and input/output waveguides. Moreover, the desired compromise between the coupling efficiency and resonance effect inside the ring can be achieved by mere optimisation of the slot geometrical characteristics. It has been demonstrated that higher improved performance can be achieved by introducing sub-wavelength slot to the waveguide constricting the ring.

Chapter 8

Optical Delay Lines Based on Slotted Microcavity Ring Resonators

8.1 Introduction

Having established the effectiveness in terms of coupling efficiency, finesse, and quality factors of the SMRR configuration, this structure is then used as building block for a new optical delay line. Firstly, in this chapter the fundamental principles of slotted-coupled-resonator optical waveguide (SCROW) delay line are investigated, then two different designs for SCROW optical delay lines are presented and their performance is analysed and compared to the case of conventional MRR delay line.

8.2 Overview of Optical Delay Lines

The progress in integrated optical technology may significantly have an effect on the future rate of development of optical networks. Carrying out the process of buffering via electronics can lead to bottlenecks in high-speed optical networks [30, 37]. Thus, optical buffering and storage can open new era in future all optical packet- switched networks and computer systems to prevent traffic contention [30]. Optical delay lines play an essential role in avoiding traffic contention particularly when multiple packets are simultaneously destined for the same output port [29, 37]. Different schemes have been proposed in order to construct on-chip delays: routing the data along waveguides of differing length, and exploiting group-delay effects in microresonators. Recent years have seen spectacular progress in development of optical pulse delays based on integrated optic cavities such as microrings, microdisks, and photonic crystals microcavities.

In this context, Yanik *et al*., have revealed that dynamic tuning procedures are essential to stop light pulses [63-64]. The design they proposed is based on photonic crystal

coupled microcavities. However, it involves the employment of many microcavities which are bulky and can lead to minimise the level of integration of optical devices [42, 43, 63, 64, 91, 92, 111].

Recently published work has shown excellent comparison of three on-chip optical delay devices: an all pass filter (APF) with cascade of 36 ring resonators, a coupled-resonator optical waveguide (CROW) consisting of 100 ring resonators, and a simple non-resonant 4 cm waveguide delay line [30]. In this chapter, slotted miocrocavity ring resonators are employed to propose novel design of optical delay lines. Due to the E-field discontinuity across material interferences, SMRRs are capable of supporting strongly confined light within low-refractive index materials by means of TIR mechanism at a level that cannot be accomplished by using conventional waveguides [103].

8.3 Coupled Resonator Optical Waveguide Structures: Design Principles

The optical resonators are found to be ideal platform for storing light in physical small sizes. In particular, serial coupled microresonators may offer a new scheme for controlling the group velocity of optical pulses in compact way on a chip [45].

The architecture of CROW incorporating an array of directly coupled ring resonators with the same geometrical length place between two bus waveguides as shown in Fig. 8.1.

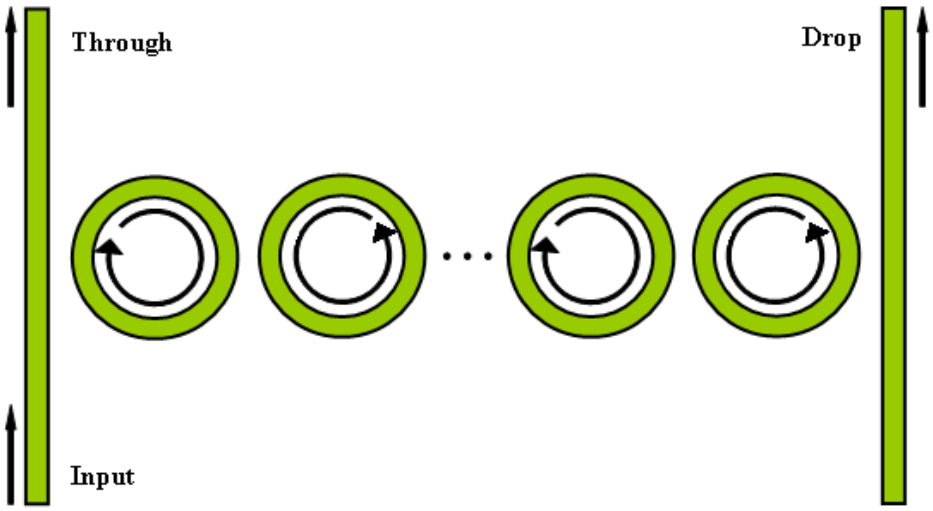

Figure 8.1 Schematic diagram of CROW

Input light pulses propagate in microring CROWs by means of coupling between neighbouring resonators and spend the most of their time circulating within each resonator, consequently large group delay can be achieved. The general characteristics of the CROWs such as dispersion relation and band structure can be described by the coupling between the adjacent resonators and input bus waveguides, the FSR, and the Q-factor. The performance of the CROWs can be affected primly by the parameters that set the resonators [45].

In order to design CROW based on MRRs, it is essential to understand and control the coupling of light between the MRRs and input and output bus waveguides. When a chain of directly coupled ring resonators are coupled to linear waveguides which serve as input/output ports, the system behaves like tunable and frequency dependent time delay. Poon *et al*., successfully presented in [45] theoretical framework model used to analysis coupled resonator optical waveguides using transfer matrix method. These accurate analytical formulas are found to be valid to any kind of resonators. When

looking at this expression from a coupling efficiency point of view, these formulas are function of coupling coefficients which can be calculated numerically by one of accurate existing numerical techniques.

As described in [45], in the limit of weak coupling κ << 1, the dispersion relation can be derived as

$$\omega(K) = \Omega\left[1 \pm \frac{|\kappa|}{m\pi}\cos\left(K\Lambda\right)\right] \tag{8.1}$$

where Ω is the resonance frequency of an uncoupled resonator in radians per second, K is the Bloch wave vector, Λ is the periodicity of the structure, m=(Ω n_{eff} R/c) is the azimuthal modal number, *R* is the ring radius, *c* is the velocity of light in vacuum, n_{eff} is the effective refractive index of the ring. The maximum of group velocity at the centre of the CROW transmission band where ω=Ω and KΛ= $\pi/2$ can be calculated using the following formula [45]

$$\left|v_g(\Omega)\right| = \frac{c|\kappa|\Lambda}{\pi R\, n_{eff}(\Omega)} \tag{8.2}$$

The delay time of a pulse propagate through CROW is determined at the centre of CROW band by distance traversed in the CROW and the group velocity which can be expressed by the following equation [45]

$$\tau_d = \frac{\pi R\, n_{eff}(\Omega)}{c}\sum_{i=1}^{N}\frac{1}{|\kappa_i|} \tag{8.3}$$

where N is the number of the rings.

It is obvious from equation 8.3 that the CROW performs as customary waveguide with group velocity c/n_{eff} but with effective length of [45]

$$L_{eff} = \frac{c\tau}{n_{eff}} = \pi R \sum_{i=1}^{N} \frac{1}{|\kappa_i|} \tag{8.4}$$

The quality that describes the ratio of the group velocity in free space to the group velocity in CROW is the slowing factor, S which can be determined by [45]

$$S_{\Omega} = \frac{\pi \, n_{eff}(\Omega)}{2|\kappa|} \tag{8.5}$$

The total loss from the input to the output of the CROW can be obtained by the following equation [45]

$$\alpha_{tot} = \alpha L \sum_{i=1}^{N} \frac{1}{2|\kappa_i|} \tag{8.6}$$

where αL is the intensity attenuation coefficient of the ring ,L is the ring circumference, $\exp^{(-\alpha_{tot})}$ is the net power attenuation coefficients of CROW, and $\exp^{-\alpha L}$ is the power attenuation in the waveguide of the constituent resonators.

The quantitative benchmark to determine the quality of a delay line is called figure of merit (FOM) and can be expressed as [45]

$$FOM = \frac{2|\kappa|}{\alpha L} \tag{8.7}$$

8.4 Newly Suggested Coupled Resonator Optical Waveguide Structures

To enhance the performance of the suggested structure, a new design is proposed and shown in Fig. 8.2. In order to promote the electrical field confinement and improve the resonance effects, micrometric-scale low-index slot is inserted into the bent waveguide build the ring.

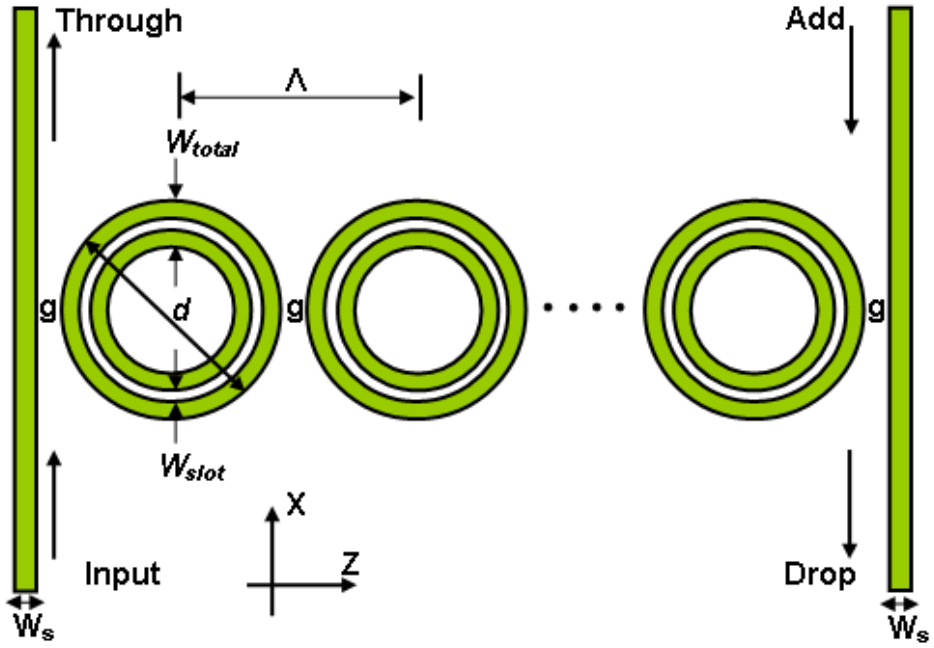

Figure 8.2 Schematic diagram of proposed SCROW

The main advantage of this slotted configuration is that the coupling coefficients can be controlled by simply engineering the slot microring. The slotted microcavity resonating at resonance frequencies is able to trap these frequencies from the primary waveguide where they can take some time propagating within the cavity by means of TIR and then drop them into secondary waveguide. In particular, by chaining a row of side-coupled resonators instead only one, the delay efficiency will be shown to be greatly improved.

A preliminary study of SCROW is carried out in this thesis to investigate numerically the resonance frequency and the coupling efficiency of the wave travelling across the slotted ring waveguide. This work carried out here uses the S-MRTD technique to simulate single stage of SCROW (N = 1). Assuming the coupling coefficients are identical between other rings, the numerically obtained coupling coefficients for the

SMRRs applied to the mathematical derivations described in the previous section to predict the performance of suggested delay lines.

8.5 SCROW Performance

The structure is selected to enable direct comparison between the design results in this work and those in [45]. The frequency range of interest includes wavelengths around λ = 1.55µm. Thus, the SCROW structure that consists of a sequence of directly coupled slotted microcavity ring resonator whose schematic is shown in Fig. 8.2 is considered. Each microring of diameter d = 5 µm and width w_{total} = 709 nm is made of silicon (refractive index n_{core} = 3.2) and is micro-structured to exhibit a slot of width w_{slot} =130 nm. These slotted ring resonators are coupled to two identical straight silicon waveguides (refractive index n_{core} = 3.2) that are w_s = 0.3 µm wide. The minimal separation between the bus waveguides and the rings is set to be g = 245 nm. The entire device is placed in air background (refractive index n_{air} = 1).

Based on the results obtained in chapter 7, it is found that a good compromise between coupling efficiency and quality factor can be fulfilled for SMRR positioned at η = 0.7. Therefore, the design issue of slowing light and building delay lines with SCROWs at η = 0.7 is addressed here for the first time, to the best of the author's knowledge, for two different materials filling the slot which are SiO_2 and air respectively.

8.5.1 SCROW Filled with SiO_2

Figure 8.3 presents the variation of coupling coefficients with the resonance wavelength in the SCROW configuration where SiO_2 is used to fill the slots and $\eta = 0.7$. The work carried out here employs the S-MRTD technique to simulate single stage of SCROW (N = 1).

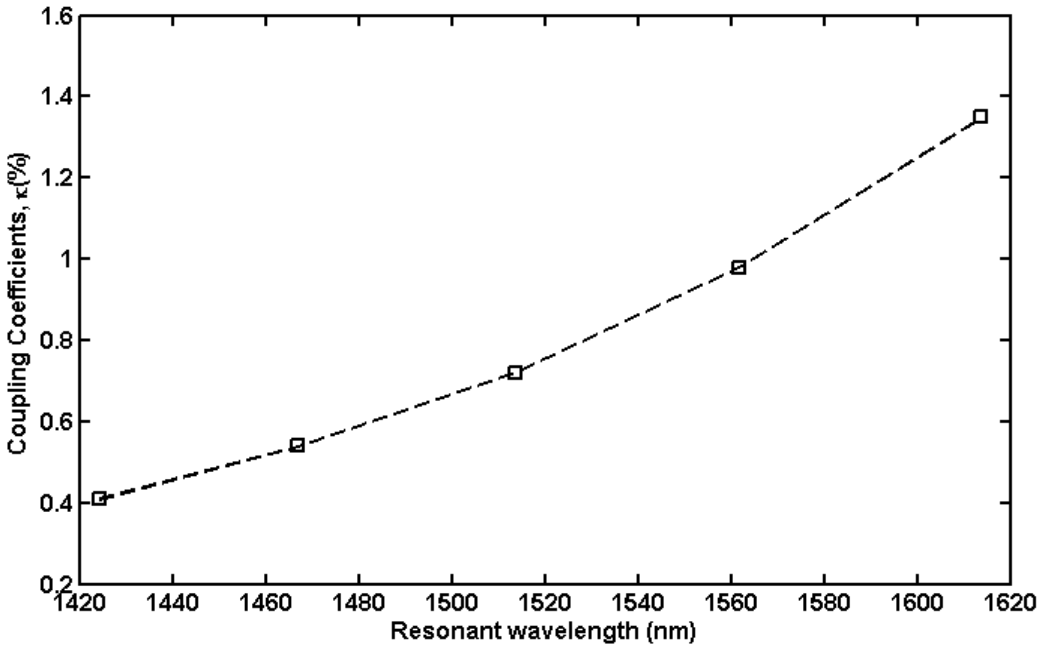

Figure 8.3 Variation of coupling coefficients κ with resonant wavelength λ_{res} at $\eta = 0.7$ for SCROW filled with SiO_2 where N = 1

It is clear that the amount of coupled power at resonance rapidly increases towards higher wavelengths. It can be seen from this figure that the percentage of coupling ranges between 0.54% and 1.38 %.

Next, figure 8.4 shows the variation of maximum group velocity as a function of resonant wavelength. It can be seen that at higher resonant wavelengths, the maximum group velocity is maximised while it decreases at lower resonance, this is due to

increased coupled efficiency occurring at high resonant wavelengths.

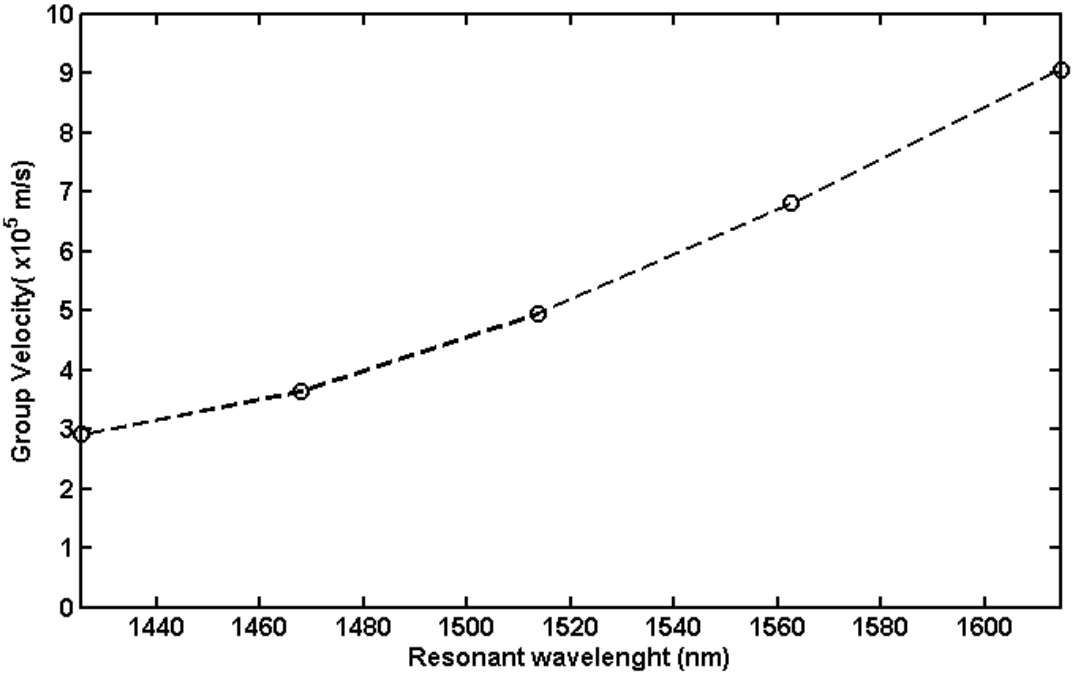

Figure 8.4 Variation of group velocity with resonant wavelength λ_{res} at $\eta = 0.7$ for SCROW filled with SiO_2

From this figure, it can be seen that the maximum group velocity ranges between 2.917×10^5 m/s and 9.062×10^5 m/s.

Inversely, as shown in figure 8.5, the slowing factor decreases rapidly at high resonant wavelengths as it is expected for higher values of coupling efficiency.

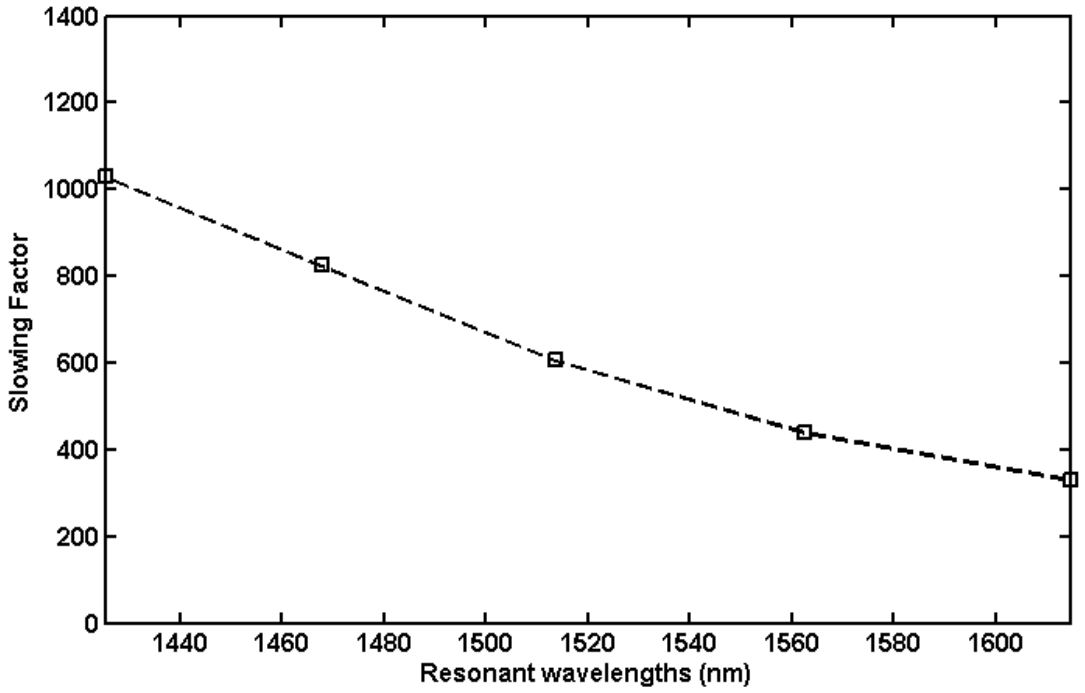

Figure 8.5 Variation of slowing factor with resonant wavelength λ_{res} at $\eta = 0.7$ for SCROW filled with SiO_2

From figure 8.5, the slowing factor is found to be in the ranges from 331 to 1029.

Final results in terms of delay time are given in figure 8.6 where the variation of delay time with required coupling coefficients is considered in different SCROW configurations for which the number of rings is made vary from a minimum of 4 to a maximum of 16.

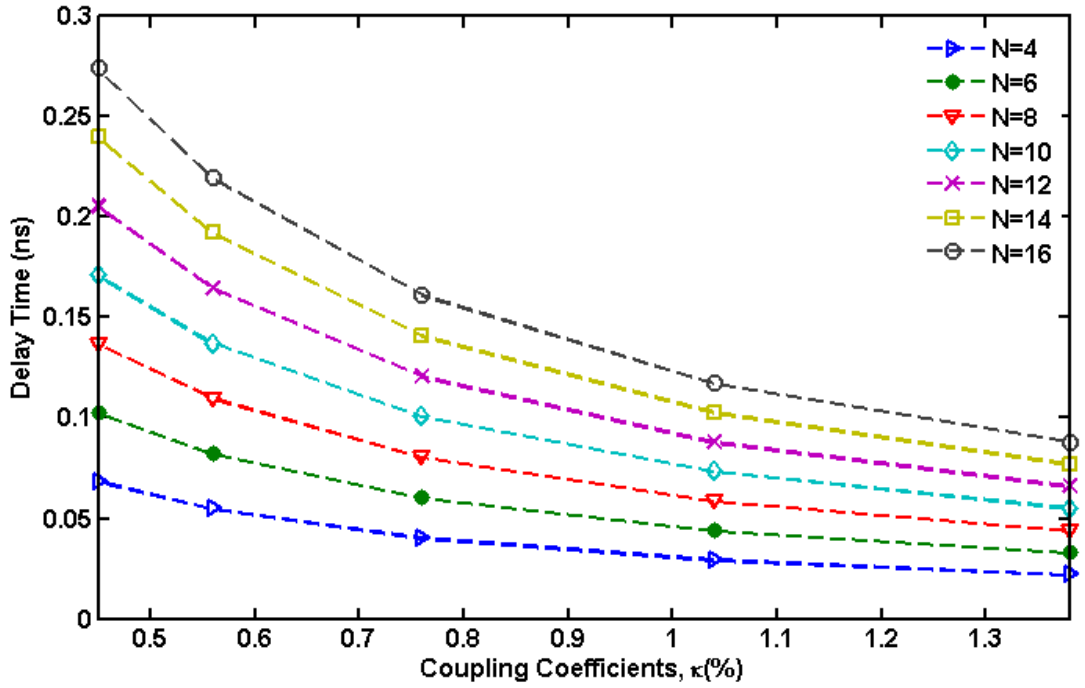

Figure 8.6 Variation of delay time with coupling efficiency for different N at η = 0.7 for SCROW filled with SiO_2

Figure 8.6 suggests that, when the number of rings is increased, the amount of obtained delay time rapidly increases. At fixed number of stages, the delay time also significantly decreases when higher coupling efficiency are allowed.

8.5.2 SCROW filled with Air

Figure 8.7 shows the MRTD results obtained from the 5-µm-diameter slotted microring resonator with the same position investigated in Figure 8.3. At η = 0.7 when the slot is filled with air and N = 1.

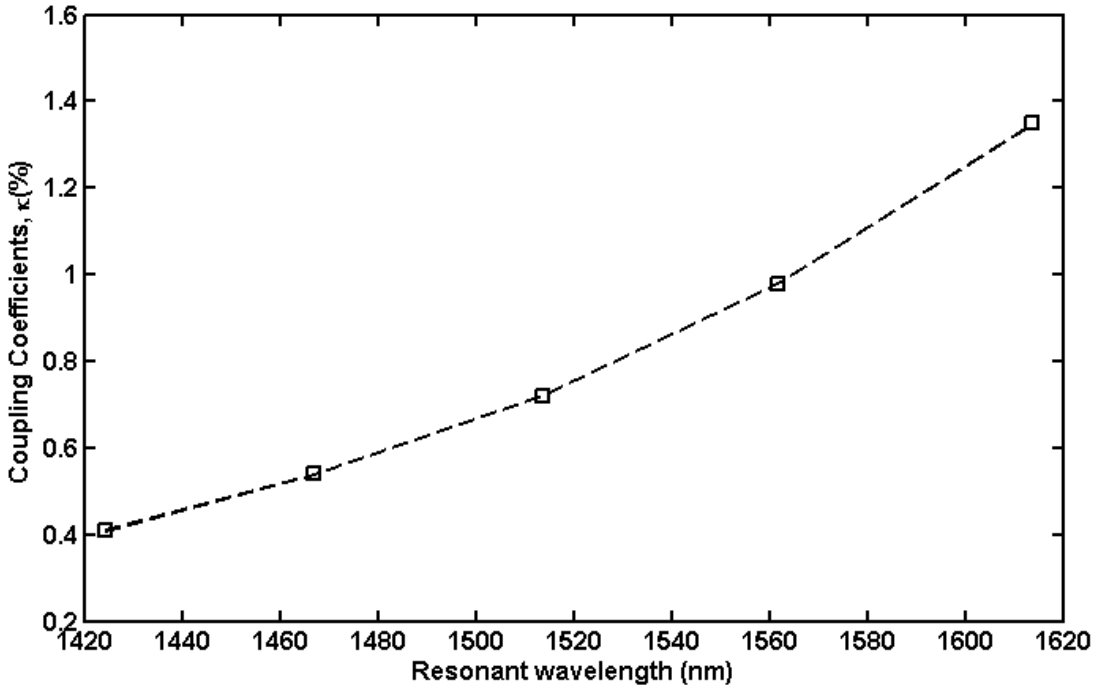

Figure 8.7 Variation of coupling coefficients κ with resonant wavelength λ_{res} at η = 0.7 for SCROW filled with air

Compared to the SMRR filled with SiO_2 previously considered, the SMRR filled with air shows slightly lower coupling efficiency at fixed resonance frequency with values in the range $0.5\% \le \kappa \le 1.35\%$.

Carrying on the analysis, the maximum group velocity versus resonant wavelength is reported in figure 8.8. It can be seen that the maximum group velocity ranges between 2.666×10^5 m/s and 8.905×10^5 m/s in the frequency window of interest.

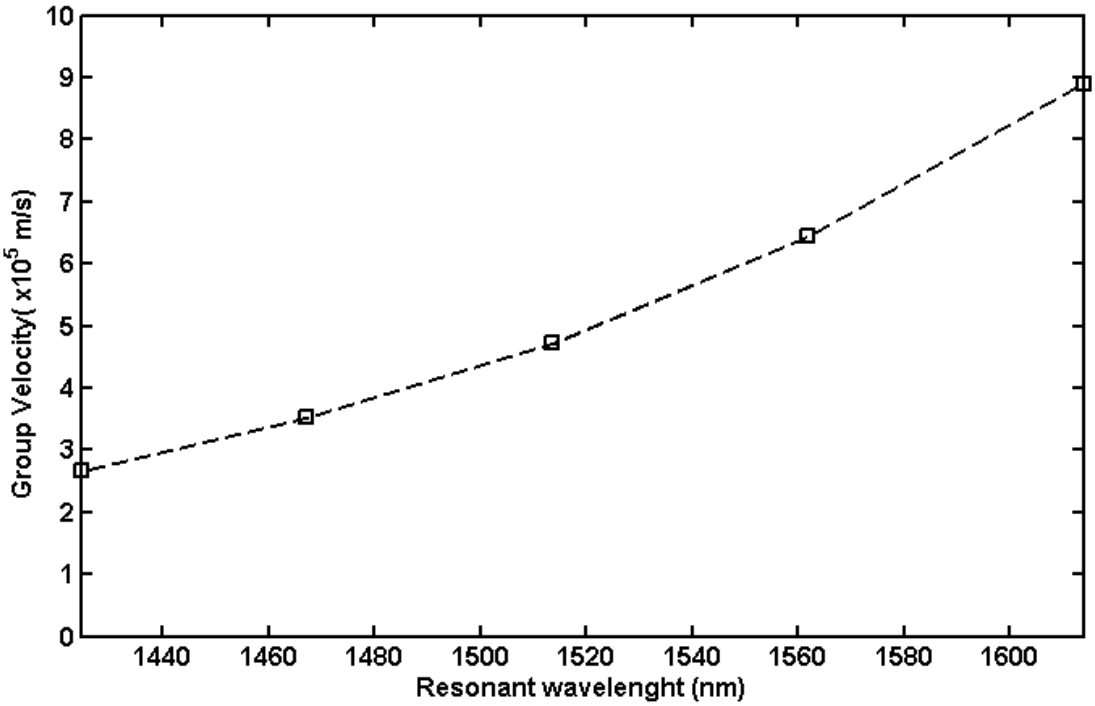

Figure 8.8 Variation of group velocity with resonant wavelength λ_{res} at η = 0.7 for SCROW filled with air

Next, figure 8.9 shows the variation of slowing factor with the resonant wavelength. It shows that the slowing factor decreases in the high resonant wavelengths.

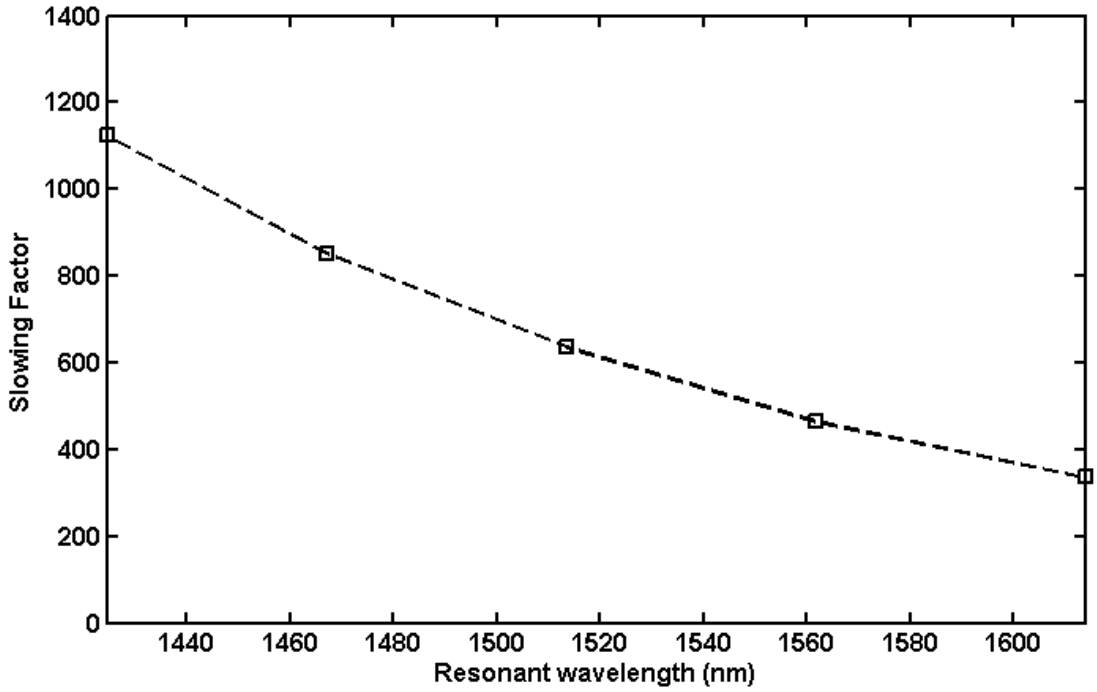

Figure 8.9 Variation of slowing factor with resonant wavelength λ_{res} at η = 0.7 for SCROW filled with air

From figure 8.9, the slowing factor is found in the range from 337 to 1125 which is slightly increased if compared to the case of SiO_2 filled SCROW at fixed frequencies.

Then, the variation of delay time of SCROW with coupling coefficients for different number of resonators is shown in figure 8.10.

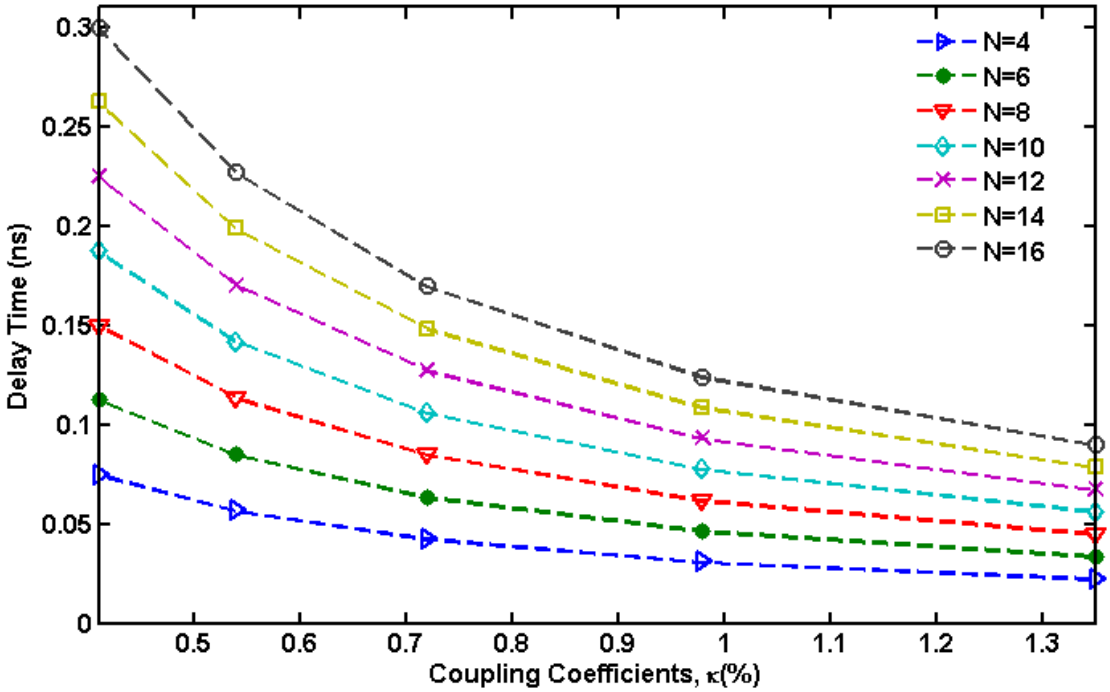

Figure 8.10 Variation of delay time with coupling efficiency for different N at η = 0.7 for SCROW filled with Air

This figure shows the delay time variation for different coupling coefficients and number of stages taken in the SCROW. Similarly to the case of SiO_2 filled SCROW.

Figure 8.10 suggests that, when the number of rings is increased, the amount of delay time rapidly increases. Comparing the two cases of different slot materials, it can be noted that at fixed values of N and κ, the SCROW filled with air allows for slightly higher delay times.

Table 8.1 below holds a direct comparison of 10 resonators delay line composed of various types of resonators in different material system at 1.55 μm.

Table 8.1 comparison of CROW delay lines consisting of N = 10 resonators

Resonator Type	n_{eff}	R (μm)	κ(%)	Q	Net loss (dB)	Delay (ps)	FOM
SMRR filled with SiO_2	2.908	2.5	1.38	4892	35	55	1.248
SMRR filled with Air	2.895	2.5	1.35	5043	34	56	1.256
III-V semiconductor MRR [43, 81]	3	10	1	5000	33	31	1.300

As evidenced by the comparison in Table 8.1, application requirements, such as acceptable losses, and material system, dictates the type of resonator that will be the most suitable. In order to achieve long delay without too much attenuation, resonators with high quality factor are required. Therefore, from Table 8.1, it is observed that the proposed design, based on air slot ring resonators, outperforms the counterpart designs, including the structure reported in [43], [81], and therefore it is identifies as optimum design for the desired purposes.

8.6 Summary

This chapter has presented an overview of optical delay lines based on optical microcavity ring resonators, with a detailed look at delay line parameters. A number of key issues in designing delay lines have been addressed. After that, the chapter explained the specific case of implementing slotted ring resonators for optical delay lines. Coupling efficiency of the SMRRs has been numerically investigated by 2D S-MRTD. The group velocity, slowing factor, and delay time have been determined by analytical expressions that are rigorously employed to analyse and optimise the performance of optical delay lines based on such configuration. After that, a comparison

was made between conventional delay lines and newly suggested optical delay lines in terms of achievable delay time, losses, and figure of merit. It was found that the newly suggested optical delay line based on slotted ring resonators can achieve higher delay time with overall smaller ring size while keeping the same level of losses.

Chapter 9

Conclusions and Future Research Directions

9.1 Conclusion

This thesis has addressed MRTD computational modelling and design of micro- and nano-scale integrated optical devices. Particularly, micarocavity ring resonators for the potential of high-density integration with other photonic devices. The primary objectives of this research were to develop and refine MRTD algorithms for modelling the electrodynamics of optical materials and structures, and to put into practice these techniques to the emerging class of microcavity devices.

During the course of this research, MRTD formulations based on UPML approach were developed for modelling microcavity ring resonators. Rigorous validations of this algorithm have demonstrated the potential for high accuracy of this model over large bandwidth. This thesis presented detailed MRTD modelling results for micarocavity ring resonators, and discussed the key design parameters and tradeoffs that were identified consequently of these modelling investigations. The MRTD approach proved to be much more accurate in modelling the MRR than the previously used FDTD approach. Finally, the comparison between different slot and non slot configurations within the microcavity illustrated the advantage of the slotted ring structure for providing higher performance of coupled -resonator optical waveguide structures which are found to be useful in designing optical delay lines.

Future Research Directions

Since the introduction of MRRs in 1969, researchers have never stopped to seek for new analytical and numerical tools to allow a better understanding and the accurate design of these structures. Even though the work in this field has allowed for the design and

analysis of MRRs based devices, there is much room for improvement, and there are many stones which have been left unturned. For instance, waveguide losses and ring losses have to be technologically improved in order to realise more complex functions and devices. Although, plenty of technological steps are being tackled, the complexity of the devices increases and the design and characterisation of the devices need more attention. For this reason, accurate tools predicting the behaviour of complex devices are of particular interest to come to grips with these complexities with many parameters and design choices.

In this thesis, microcavity ring resonators and its application to optical communications have been studied and analysed thoroughly. The performance of the MRRs is mainly determined by coupling efficiency, and propagation loss inside the microring resonator. Consequently, simulation tools that can be employed in order to perform a more realistic analysis and describe the field propagation as affected by the out-of-plane losses have to be available.

In the case of lateral coupling scheme, the coupling efficiency can be estimated in the context of the effective index method by reducing waveguide problems from 3D to 2D and then calculate the field overlap between the mode in the bus waveguide and the ring. Therefore, fully 3D MRTD is necessary to investigate the nature of the process in more realistic way that can enable improved optimisation of the design of MRRs and allow better comparison with experimental data.

It is clear the MRRs will play groundbreaking role in future optical signal processing and computing. However, owing to their small space scale that involves expensive fabrication processes, a small number of those devices have been realised. The

prohibitive costs of these fabrication processes have pushed research efforts be directed towards creating innovative, comprehensive, and accurate numerical tools for the analysis and design of such devices which can represent a solid foundation for the growth of photonics. Therefore, adding scaling/wavelet in the expansion of the field. MRTD can offer great potential to build time and space adaptive codes where the level of resolution in time and space dramatically changes.

Another possible direction is to investigate the features and properties of MRRs in nonlinear materials that can be basic building blocks for nonlinear components. This is can be achieved by adapting the MRTD code at hand in order to cope with nonlinear phenomena such as dispersion within the field.

The aims and milestone set at the beginning of this project have been met, and the main contributions to knowledge generated in this work can be summarised as follows

- Become thoroughly familiar with the MRTD numerical modelling technique and developed numerical technique for implementing very fine resolution in time and in space, successfully implemented them within the MRTD method, and made full assessment of its performance.
- Created novel design MRRs for the purpose of optical communication.
- Carried out the analysis of MRRs based slotted waveguides.
- Offered new highly competitive and highly efficient designs of optical delay lines based slotted ring resonators.

Appendices

Appendix A

A.1 Maxwell's Equations

Maxwell's equations are a powerful tool to account for the propagating electromagnetic waves in dielectric media and, in particular, in MRRs devices. There are mainly four electromagnetic field vectors that govern the electromagnetic phenomena. These four electromagnetic vectors describe the relationship between electric and magnetic fields that are function of both position r [m] and time t [s] [38]. In their differential form, Maxwell's equations for EM propagating are written as:-

$$\nabla \times E = -\frac{\partial B}{\partial t} + M \tag{A.1}$$

$$\nabla \times H = \frac{\partial D}{\partial t} + J \tag{A.2}$$

$$\nabla . D = \rho \tag{A.3}$$

$$\nabla . B = 0 \tag{A.4}$$

where E is the vectorial electric field, in V/m, H is the vectorial magnetic field, in A/m, D is the electric flux density, in Coul/m^2, B is magnetic flux density, in Wb/m^2, M is the (fictitious) equivalent magnetic current density, in V/ m^2, J is the current density, in A/m^2, ρ is the free charge density, in Coul/m^3.

The physical background behind theses equations is that according to (A.1) the origin of the electrical field vortices ($\nabla \times E$) is the time-dependent change of magnetic field ($-\partial B/\partial t$). At the same time as (A.2), the magnetic field vortices ($\nabla \times H$) can be either time-dependent change of the electric flux density ($\partial D/\partial t$) or a result of the current

density in the material (*J*).

In order for a linear, homogeneous, and isotropic medium, the following constitutive relations are written

$$B = \mu H \tag{A.5}$$

$$D = \varepsilon E \tag{A.6}$$

$$J = \sigma E \tag{A.7}$$

$$M = \sigma^{*} H \tag{A.8}$$

where ϵ is the dielectric permittivity, in F/m, μ is the magnetic permeability of the medium, in H/m, σ is the electric conductivity, in S/m, σ^* is the equivalent magnetic loss, in Ω/m.

By handling equations (A.1) and (A.2), the following system of six scalar equations in Cartesian coordinate are obtained from Maxwell's equations for electromagnetic propagation theory, as expressed below:-

$$\frac{\partial E_x}{\partial t} = \frac{1}{\varepsilon}\left(\frac{\partial H_z}{\partial y} - \frac{\partial H_y}{\partial z} - \sigma E_x\right) \tag{A.9}$$

$$\frac{\partial E_y}{\partial t} = \frac{1}{\varepsilon}\left(\frac{\partial H_x}{\partial z} - \frac{\partial H_z}{\partial x} - \sigma E_y\right) \tag{A.10}$$

$$\frac{\partial E_z}{\partial t} = \frac{1}{\varepsilon}\left(\frac{\partial H_y}{\partial x} - \frac{\partial H_x}{\partial y} - \sigma E_z\right) \tag{A.11}$$

$$\frac{\partial H_x}{\partial t} = \frac{1}{\mu}\left(\frac{\partial E_y}{\partial z} - \frac{\partial E_z}{\partial y} - \sigma^{*} H_x\right) \tag{A.12}$$

$$\frac{\partial H_y}{\partial t} = \frac{1}{\mu}\left(\frac{\partial E_z}{\partial x} - \frac{\partial E_x}{\partial z} - \sigma^{*} H_y\right) \tag{A.13}$$

$$\frac{\partial H_z}{\partial t} = \frac{1}{\mu}\left(\frac{\partial E_x}{\partial y} - \frac{\partial E_y}{\partial x} - \sigma^* H_z\right) \tag{A.14}$$

Appendix B

B.1 Introduction to Method of Moment (MoM)

Like any numerical techniques based on method of moments, MRTD can be derived with applying specific expansion and testing function [109]. The idea behind method of moments is to represent the unknown function, $f(x,t)$ as a sum of unknown coefficients, a_n multiplied by known basis functions, c_n. The unknown coefficients can be calculated using a system of equations that is developed by choosing a number of testing functions ω_n that is equal to the number of unknown coefficients. For instance, in 1D problem if:-

$$f(x) = \frac{\partial b(x)}{\partial x} \tag{B.1}$$

where $f(x)$ represent unknown function and $b(x)$ is known function.

Thus the function in (B.1) is expanded as following

$$f(x,t) = \sum_{n=0}^{N} a_n c_n(x) \tag{B.2}$$

By means of inner product,

$$\langle \omega_n, f \rangle = \langle \omega_n, b' \rangle = \int \omega_n(x) f(x) dx \tag{B.3}$$

A system of linear equations can be created as

$$\begin{bmatrix} a_1\langle \omega_1, c_1 \rangle & a_2\langle \omega_1, c_2 \rangle & \cdots & a_N\langle \omega_1, c_N \rangle \\ a_1\langle \omega_2, c_1 \rangle & a_2\langle \omega_2, c_2 \rangle & \cdots & a_N\langle \omega_2, c_N \rangle \\ \vdots & \vdots & \ddots & \vdots \\ a_1\langle \omega_N, c_1 \rangle & a_2\langle \omega_N, c_2 \rangle & \cdots & a_N\langle \omega_N, c_N \rangle \end{bmatrix} = \begin{bmatrix} \langle \omega_1, b' \rangle \\ \langle \omega_2, b' \rangle \\ \vdots \\ \langle \omega_N, b' \rangle \end{bmatrix} \tag{B.4}$$

Solving these equations lead to determining unknown coefficients a_n. It is obvious from (B.4) that the matrix becomes diagonal when the following property for testing functions holds

$$\langle \omega_m , c_n \rangle = \delta_{m,n} \tag{B.5}$$

So that each coefficient can be calculated as

$$a_n = \langle \omega_n , b' \rangle \tag{B.6}$$

The base function can also be used as testing function if the following holds

$$\langle \omega_m , \omega_n \rangle = \delta_{m,n} \tag{B.7}$$

This technique is called Galerkin's procedure.

Appendix C

C.1 Updated MRTD Technique

By means of Galerkin's method, the MRTD update equations can be calculated with wavelet discretisation of electric and magnetic fields. The MRTD update equations are evaluated by localising the coefficients in time and space, using the time basis functions and scaling/wavelet functions respectively.

C.2 Approximation in time: testing with pulse functions

MRTD update in time is performed by testing with the time basis functions that give the localization of the expansion coefficients in time. Thus, in order to construct explicit scheme in MRTD, the pulse functions, whose time derivatives lead to two Dirac Delta functions placed at the edges of the pulse as shown in figure C.1, are used as time expansion coefficient [74]

$$\frac{\partial h_{i+\frac{1}{2}}(t)}{\partial t} = \delta\left(t-(i+\frac{1}{2})\Delta t\right) - \delta\left(t-(i-\frac{1}{2})\Delta t\right) \tag{C.1}$$

The time derivatives of the pulse functions that form the time discretisation are Delta series as depicted by top line of figure C.1.

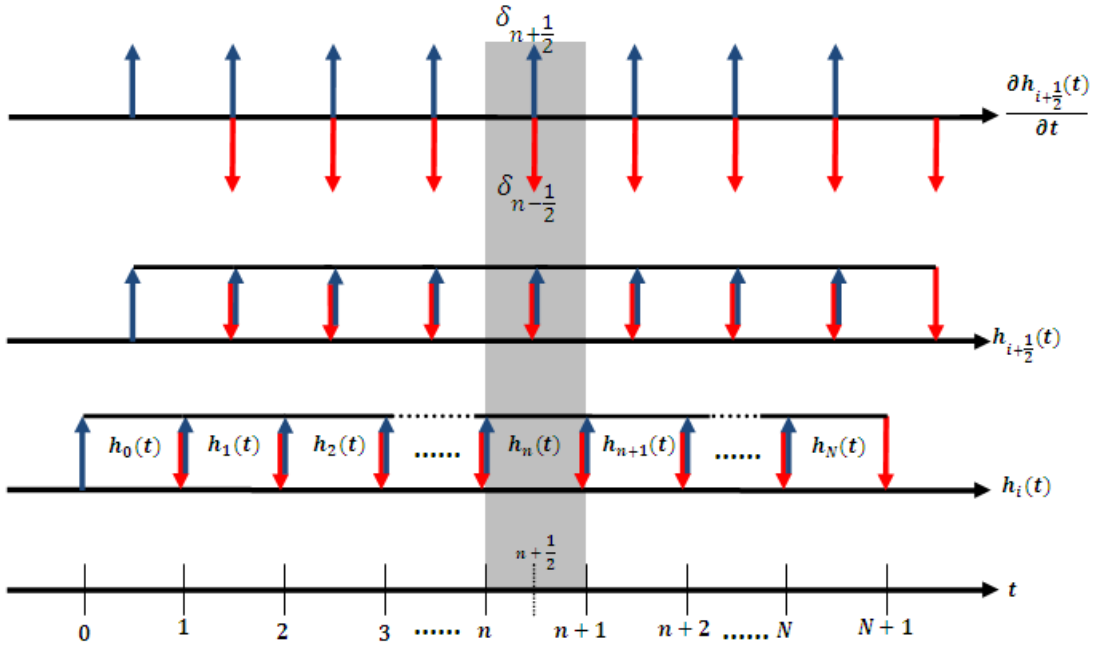

Figure C.1 Representation of the derivative of the basis functions in time when h_i are pulses functions

From Maxwell's equations, the coefficients of D (and E) are located at time step *n*. At the same time as B (and H) coefficients are located at time step *n*+1/2. The expansion of the E-field in time is expressed by [74]

$$E\left(\vec{r},t\right)=\sum_{i=0}^{N} h_i\left(t\right)_i E\left(\vec{r}\right) \tag{C.2}$$

where ${}_i E\left(\vec{r}\right)$ is the wavelet/scaling discretisation in space at time step *i*, $h_i(t)$ is testing pulse functions as shown in figure C.1.

Similarly, *B*-field can be expressed as [74]

$$B\left(\vec{r},t\right)=\sum_{i=0}^{N} h_{i+\frac{1}{2}}\left(t\right)_{i+\frac{1}{2}} B\left(\vec{r}\right) \tag{C.3}$$

where ${}_{i+\frac{1}{2}}B\left(\vec{r}\right)$ is the wavelet/scaling discretisation in space at time step i+1/2.

Assuming no magnetic loss, equation (A.12) can be rewritten as

$$\frac{\partial B_x}{\partial t} = \left(\frac{\partial E_y}{\partial z} - \frac{\partial E_z}{\partial y} \right) \tag{C.4}$$

By performing the inner product to equation C.4 with $h_i(t)$

$$\left\langle h_i , \frac{\partial B_x}{\partial t} \right\rangle = \left\langle h_i , \frac{\partial E_y}{\partial z} - \frac{\partial E_z}{\partial y} \right\rangle \tag{C.5}$$

Taking the following expressions into account

$$\left\langle h_i(t), E\left(\vec{r}, t\right) \right\rangle = {}_i E\left(\vec{r}\right) \Delta t \tag{C.6}$$

$$\left\langle h_i(t), \frac{\partial B\left(\vec{r}, t\right)}{\partial t} \right\rangle = {}_{i+\frac{1}{2}}B\left(\vec{r}\right) - {}_{i-\frac{1}{2}}B\left(\vec{r}\right) \tag{C.7}$$

The following formula is obtained

$${}_{i+\frac{1}{2}}B_x\left(\vec{r}\right) - {}_{i-\frac{1}{2}}B_x\left(\vec{r}\right) = \Delta t \left[\frac{\partial_i E_y\left(\vec{r}\right)}{\partial z} - \frac{\partial_i E_z\left(\vec{r}\right)}{\partial y} \right] \tag{C.8}$$

Subsequently, the updated term ${}_{i+\frac{1}{2}}B_x\left(\vec{r}\right)$ is obtained

$${}_{i+\frac{1}{2}}B_x\left(\vec{r}\right) = {}_{i-\frac{1}{2}}B_x\left(\vec{r}\right) + \Delta t \left[\frac{\partial_i E_y\left(\vec{r}\right)}{\partial z} - \frac{\partial_i E_z\left(\vec{r}\right)}{\partial y} \right] \tag{C.9}$$

It is clear from (C.9) that the new field component B_x at i+1/2 is dependently calculated from the value at previous time step at i-1/2.

C.3 Approximation in space: testing with scaling/wavelet functions

In 3D space, the basis functions are separable functions expressed as *V(x)V(y)V(z)*, where *V* represents either φ_l scaling functions, or $\psi_{l,p}^{r}$ wavelet functions, with $l = i, j, k$ as directional index in the three space directions. The approximation of derivatives in space domain can be performed by applying testing functions through the time differentiated functions in (C.9).

For practical purposes, the discretisation of the field is required to be represented in vectorial notation that is a generalised form for any wavelet basis [19]. Therefore, all the wavelet/scaling coefficients are expressed as

$$
{}_{n+\frac{1}{2}}\vec{B}_{x,i,j,k} = \begin{bmatrix}
{}_{n+\frac{1}{2}}B^{x,\varphi\varphi\varphi}_{i,j,k} \\
{}_{n+\frac{1}{2}}B^{x,\psi\varphi\varphi}_{i,j,k,0,0} \\
\vdots \\
{}_{n+\frac{1}{2}}B^{x,\varphi\varphi\psi}_{i,j,k,r_{\max.z},2^{r_{\max.z}}-1} \\
{}_{n+\frac{1}{2}}B^{x,\psi\psi\varphi}_{i,j,k,0,0,0,0} \\
\vdots \\
{}_{n+\frac{1}{2}}B^{x,\varphi\psi\psi}_{i,j,k,r_{\max.y},2^{r_{\max.y}}-1,r_{\max.z},2^{r_{\max.z}}-1} \\
{}_{n+\frac{1}{2}}B^{x,\psi\psi\psi}_{i,j,k,0,0,0,0,0,0} \\
\vdots \\
{}_{n+\frac{1}{2}}B^{x,\psi\psi\psi}_{i,j,k,r_{\max.x},2^{r_{\max.x}}-1,r_{\max.y},2^{r_{\max.y}}-1,r_{\max.z},2^{r_{\max.z}}-1}
\end{bmatrix} \tag{C.10}
$$

The vector, *V*, represents wavelet/scaling function is introduced as follows

$$V_{i,j,k} = \begin{bmatrix} \varphi_i(x)\varphi_j(y)\varphi_k(z) \\ \psi^0_{i,0}(x)\varphi_j(y)\varphi_k(z) \\ \vdots \\ \varphi_i(x)\varphi_j(y)\psi^{r_{\max.z}}_{k,2^{r_{\max.z}}-1}(z) \\ \psi^0_{i,0}(x)\psi^0_{j,0}(y)\varphi_k(z) \\ \vdots \\ \varphi_i(x)\psi^{r_{\max.y}}_{j,2^{r_{\max.y}}-1}(y)\psi^{r_{\max.z}}_{k,2^{r_{\max.z}}-1}(z) \\ \psi^0_{i,0}(x)\psi^0_{j,0}(y)\psi^0_{k,0}(z) \\ \vdots \\ \psi^{r_{\max.x}}_{i,2^{r_{\max.x}}-1}(x)\psi^{r_{\max.y}}_{j,2^{r_{\max.y}}-1}(y)\psi^{r_{\max.z}}_{k,2^{r_{\max.z}}-1}(z) \end{bmatrix} \quad \text{(C.11)}$$

Therefore

$$B_x\left(\vec{r}\right)^{n+\frac{1}{2}} = \sum_{i,j,k} V^T_{i,j,k} \; B_{x,i,j,k}^{n+\frac{1}{2}} \quad \text{(C.12)}$$

By performing the inner product of equation (C.9) with each wavelet/scaling coefficients in equation (C.11), the updated equation of *B* component can be derived and written as [74]

$$B_{x,i,j,k}^{n+\frac{1}{2}} = B_{x,i,j,k}^{n-\frac{1}{2}} + \frac{\Delta t}{\Delta x \Delta y \Delta z}\left[\sum_m U^{B_x}_{E_y,m\,n} E_{y,i,j,k+m} + \sum_m U^{B_x}_{E_z,m\,n} E_{z,i,j+m,k}\right] \quad \text{(C.13)}$$

where U represents the matrix of the inner products between E and B basis functions.

From equation (C.13), it can be noted that B_x field is expressed by the basis functions which are misplaced in the positive *y* and *z* direction. Whereas the basis functions represent E_y and E_z are offset in z-direction and in y-direction respectively.

For two different field components, F_1 (being the updated field generated) and F_2 (being the updated field generator), the general form of the U matrices is [74]

$$U_{F_2,m}^{F_1}=\begin{bmatrix}\left\langle {}_{F_1}V_1,\dfrac{\partial\,{}_{F_2}V_1\big|_m}{\partial n}\right\rangle & \left\langle {}_{F_1}V_1,\dfrac{\partial\,{}_{F_2}V_2\big|_m}{\partial n}\right\rangle & \cdots & \left\langle {}_{F_1}V_1,\dfrac{\partial\,{}_{F_2}V_L\big|_m}{\partial n}\right\rangle\\ \left\langle {}_{F_1}V_2,\dfrac{\partial\,{}_{F_2}V_2\big|_m}{\partial n}\right\rangle & \left\langle {}_{F_1}V_2,\dfrac{\partial\,{}_{F_2}V_2\big|_m}{\partial n}\right\rangle & & \\ \vdots & & \ddots & \\ \left\langle {}_{F_1}V_L,\dfrac{\partial\,{}_{F_2}V_L\big|_m}{\partial n}\right\rangle & & & \left\langle {}_{F_1}V_L,\dfrac{\partial\,{}_{F_2}V_L\big|_m}{\partial n}\right\rangle\end{bmatrix} \tag{C.14}$$

where $\partial/\partial n$ is the derivative in space with n=*y*,*z*, m represents the offset in the direction of differentiation, L= $2^{3+r_{\max,x}+r_{\max,y}+r_{\max,z}}$, is the rank of U matrices.

As an illustration, both B_x and E_y fields are collocated in *x* and *y* direction and they are misplaced in *z*-direction. Considering the offset in *x*-, *y*-, and *z*-directions are s_x, s_y, and s_z respectively, the entry (2, 2) of (C.14) will be [74]

$$U_{E_y,m,2,2}^{B_{x1}}=\left\langle \psi_{i,0}^{0}(x)\varphi_{j+s_y}(y)\varphi_{k+s_z}(z),\frac{\partial}{\partial z}\psi_{i,0}^{0}(x)\varphi_{j+s_y}(y)\varphi_{k}(z)\right\rangle=$$

$$=\iiint\psi_{i,0}^{0}(x)\varphi_{j+s_y}(y)\varphi_{k+s_z}(z)\frac{\partial}{\partial z}\left(\psi_{i,0}^{0}(x)\varphi_{j+s_y}(y)\varphi_{k}(z)\right)\partial x\partial y\partial z \tag{C.15}$$

Separating the integral by direction, the following formula is obtained

$$\iiint\psi_{i,0}^{0}(x)\varphi_{j+s_y}(y)\varphi_{k+s_z}(z)\frac{\partial}{\partial z}\left(\psi_{i,0}^{0}(x)\varphi_{j+s_y}(y)\varphi_{k}(z)\right)\partial x\partial y\partial z=$$

$$=\int\psi_{i,0}^{0}(x)\psi_{i,0}^{0}(x)\partial x\int\varphi_{j+s_y}(y)\varphi_{j+s_y}(y)\partial y\int\varphi_{k+s_z}(z)\frac{\partial\varphi_{k}(z)}{\partial z}\partial z \tag{C.16}$$

Since the collocated basis functions are orthogonal, therefore equation (C.16) can be written as

$$\int \psi_{i,0}^{0}(x)\psi_{i,0}^{0}(x)\partial x \int \varphi_{j+s_y}(y)\varphi_{j+s_y}(y)\partial y \int \varphi_{k+s_z}(z)\varphi_{k}(z)\partial z = \Delta x \cdot \Delta y \cdot \int \varphi_{k+s_z}(z)\frac{\partial \varphi_{k}(z)}{\partial z}\partial z \quad \text{(C.17)}$$

As it can be seen from equation (C.17), the triple integral is converted into 1D integral and its value relays on the selection of the basis functions being evaluated either analytically or numerically. Based on each basis functions family used, these values can be tabulated and as a result they do not need to be calculated for each simulation. Following this procedure all the update equations for the rest components can be derived in the same way.

C.4 Media discretisation

Having updated the *B* and *D* components and by means of constitutive relationship, the actual *H* and *E* fields can be calculated depends on the media characteristics. By means of isotropic and anisotropic media, the material constant can be either scalar or tensor quantity. In this thesis, only materials that are linear, isotropic, and nondispersive are considered. Supposing a medium with magnetic permeability $\mu=\mu_0$, the only constitutive relationship to be taken into account is the one to obtain *E* field from update of *D* and it can be written as

$$E_d\left(\vec{r},t\right) = \frac{1}{\varepsilon\left(\vec{r},t\right)} D_d\left(\vec{r},t\right) \quad \text{(C.18)}$$

where $\varepsilon\left(\vec{r},t\right)$ represents the space- and time-dependent permittivity of the media, *d* is the direction can be *x*, *y* or *z*.

Following the Galarkin's method and by using scaling function in space and pulse function in time, equation (C.18) can be discretised.

For simplicity, the discretisation of the field components is considered for the case of expansion in only scaling function in space which are expressed as

$$F_x\left(\vec{r},t\right)=\sum_{k,l,m,n=-\infty}^{+\infty} {}_kF^{\varphi_x}_{l+\frac{1}{2},m,n}\, h_k(t)\varphi_{l+\frac{1}{2}}(x)\varphi_m(y)\varphi_n(z) \tag{C.19}$$

$$F_y\left(\vec{r},t\right)=\sum_{k,l,m,n=-\infty}^{+\infty} {}_kF^{\varphi_y}_{l,m+\frac{1}{2},n}\, h_k(t)\varphi_l(x)\varphi_{m+\frac{1}{2}}(y)\varphi_n(z) \tag{C.20}$$

$$F_z\left(\vec{r},t\right)=\sum_{k,l,m,n=-\infty}^{+\infty} {}_kF^{\varphi_z}_{l,m,n+\frac{1}{2}} h_k(t)\varphi_l(x)\varphi_m(y)\varphi_{n+\frac{1}{2}}(z) \tag{C.21}$$

where $F_r\left(\vec{r},t\right)=\left[E_r\left(\vec{r},t\right),D_r\left(\vec{r},t\right)\right]$, with $r=x,y,z$, ${}_kF^{\varphi_r}_{l,m,n}$ is the field expansions coefficients in terms of scaling functions, l,m,n, and k are the indices that describe the localisation in space and time.

In time, the function $h_k(t)$ is given by

$$h_k(t)=h\left(\frac{t}{\Delta t}-k\right) \tag{C.22}$$

with

$$h(t)=\begin{cases}1 & for \quad |t|<\frac{1}{2}\\ \frac{1}{2} & for \quad |t|=\frac{1}{2}\\ 0 & for \quad |t|>\frac{1}{2}\end{cases} \tag{C.23}$$

while in space, the scaling function is defined as

$$\varphi_m(x)=\varphi\left(\frac{x}{\Delta x}-m\right) \tag{C.24}$$

After substituting the field expansions into equation (C.18) and sampling them with pulse functions in time and scaling functions in space, it is assumed that

$$\varepsilon_r\left(\vec{r},t\right)=\varepsilon_r(x)\varepsilon_r(y)\varepsilon_r(z)\varepsilon_r(t) \tag{C.25}$$

For instance, the sampling of *x*-component of equation (C.18) with $\varphi_{l+1/2}(x), \varphi_m(y)$, $\varphi_n(z)$, and $h_k(t)$ brings to

$$ {}_k D^{\varphi_x}_{l+\frac{1}{2},m,n} = \sum_{k',l',m',n'=-\infty}^{+\infty} \varepsilon(x)^{\varphi_x}_{l+\frac{1}{2},l'+\frac{1}{2}} \varepsilon(y)^{\varphi_x}_{m.m'} \varepsilon(z)^{\varphi_x}_{n,n'} \varepsilon(t)^{x}_{k,k'k'} E^{\varphi_x}_{l'+\frac{1}{2},m',n'} \tag{C.26} $$

where the coefficients $\varepsilon(y)^{\varphi_x}_{m.m'}$, $\varepsilon(t)^{x}_{k,k'}$ represent the integrals

$$ \varepsilon(r)^{\varphi_x}_{m,m'} = \frac{1}{\Delta r} \int_{-\infty}^{+\infty} \varphi_m(r) \varepsilon_x(r) \varphi_{m'}(r) dr \tag{C.27} $$

$$ \varepsilon(t)^{x}_{k,k'} = \frac{1}{\Delta t} \int_{-\infty}^{+\infty} h_k(t) \varepsilon_x(t) h_{k'}(t) dt \tag{C.28} $$

Appendix D

D.1 Numerical Dispersion and Stability

Numerical dispersion is always associated with all simulations carried out with any numerical techniques. This is due to the variation of phase velocity of the propagation waves along the computational domain with wavelength.

The level of variation relies on different factors such as the wavelength of propagated wave, the direction in which the wave is propagating inside the computational domain, and the selected mesh size for the discretisation of the computational domain. Thus, the numerical dispersion has proven itself as non-physical phenomena and it is unwanted for the reason that it can be associated with either phase delay or phase error which can be seen as pseudo reflections. Therefore, in order to overcome the unavoidable side effect of the discretised nature of all numerical techniques, the restrictions upon the space discretisation have to be set in place so as to minimise the numerical dispersion.

Similar to the restrictions set upon the time discretisation, they are put in place so as to keep away from numerical instability that can cause the computed results to increase with no limit as time-marching continues.

This section focuses on laying out the scheme used in this work in terms of choosing the proper space and time step size in order to minimise the unavoidable numerical dispersion and avoid numerical instability.

D.2 numerical dispersion

In Simulations carried out with the MRTD method it is possible to note that the

wavenumber of the propagating waves in the updating of the numerical scheme can be varying in computational domain with angular frequency. This phenomenon is known as numerical dispersion and it has to be taken into account in order to keep away from delays or phase errors travelling into the computational domain that may cause non-physical results. This can be accomplished by choosing proper space and time step size. The dispersion relation in three-dimensions for the ideal case in isotropic, nondispersive and linear medium is

$$\vec{k} = k_x \hat{i} + k_y \hat{j} + k_z \hat{k} \tag{D.1}$$

where

$$k = \sqrt{k_x^2 + k_y^2 + k_z^2} \tag{D.2}$$

with

$$k = \pm \frac{\omega}{c} \tag{D.3}$$

and

$$c = \frac{1}{\sqrt{\mu\varepsilon}} \tag{D.4}$$

Taking into account these parameters, the phase v_p, and group velocity v_g are obtained

$$v_p = \pm \frac{\omega}{k} = \pm c \tag{D.5}$$

$$v_g = \pm \frac{\partial \omega}{\partial k} = \pm c \tag{D.6}$$

It is obvious from equations (D.5) and (D.6) that the frequency and the wavelength are linearly linked and that both phase velocity and group velocity are not connected with frequency.

These relationships turn out to be more complex due to the discretised nature of the scheme which is intrinsically related to time and space. The space is a number of small cells which build up the grid in which the waves propagate rather than in any direction whereas the time is considered as a sequence of discrete time steps. This means that the propagation velocity of the numerical wave modes is totally reliant on both direction and frequency.

As stated in [10], the numerical dispersion for a discretised computational domain for FDTD is

$$\left[\frac{1}{\Delta x}\sin\left(\frac{k_x\Delta x}{2}\right)\right]^2+\left[\frac{1}{\Delta y}\sin\left(\frac{k_y\Delta y}{2}\right)\right]^2+\left[\frac{1}{\Delta z}\sin\left(\frac{k_z\Delta z}{2}\right)\right]^2= \left[\frac{1}{c\cdot\Delta t}\sin\left(\frac{\omega\Delta t}{2}\right)\right]^2 \tag{D.7}$$

Contrast to the above dispersion equation, which is only equivalent to MRTD scheme with Haar scaling functions, it is shows clearly that increasing the resolution by one level efficiently doubles the resolution of the method. Therefore, the general relationship can be formulated simply multiplying the space step by *u* as follows [98]

$$\left[\frac{1}{u_x\Delta x}\sin\left(\frac{u_xk_x\Delta x}{2}\right)\right]^2+\left[\frac{1}{u_y\Delta y}\sin\left(\frac{u_yk_y\Delta y}{2}\right)\right]^2+\left[\frac{1}{u_z\Delta z}\sin\left(\frac{u_zk_z\Delta z}{2}\right)\right]^2= \left[\frac{1}{c\cdot\Delta t}\sin\left(\frac{\omega\Delta t}{2}\right)\right]^2 \tag{D.8}$$

where

$$u_i=\frac{1}{2^{r_{\max,\,i}+1}}\quad,\quad i=x,y\ or\ z \tag{D.9}$$

Likewise, the general dispersion analysis for any wavelet basis and resolution level can be obtained as

$$\left[\frac{1}{u_x\Delta x}\left(\sum_{l=0}^{L_s-1}a(l)\sin\left((l+\tfrac{1}{2})\theta_x\right)\right)\right]^2+\left[\frac{1}{u_y\Delta y}\left(\sum_{l=0}^{L_s-1}a(l)\sin\left((l+\tfrac{1}{2})\theta_y\right)\right)\right]^2+\left[\frac{1}{u_z\Delta z}\left(\sum_{l=0}^{L_s-1}a(l)\sin\left((l+\tfrac{1}{2})\theta_z\right)\right)\right]^2 =$$

$$\left[\frac{1}{c\cdot\Delta t}\sin\left(\frac{\omega\Delta t}{2}\right)\right]^2 \tag{D.10}$$

where

$$\theta_r = \frac{u_r k_r \Delta r}{2} \quad , \quad r = x, y \text{ or } z \tag{D.11}$$

D.3 Numerical stability

It has been clearly shown in the above that careful choice of space and time step size can have an effect on the wave propagation characteristics and substantially decrease numerical dispersion. In the same way, bounding the time step can guarantee numerical stability. MRTD with expansion in scaling functions only impose a specific limit on the selection of the time step that is linked to the space step [74]

$$\Delta t \le \frac{1}{\sum_{i=0}^{L_s-1}|a(l)|\sqrt{\frac{1}{\mu\varepsilon}\left(\frac{1}{\Delta x^2}+\frac{1}{\Delta y^2}+\frac{1}{\Delta z^2}\right)}} \tag{D.12}$$

In the specific case of a cubic cell having $\Delta x = \Delta y = \Delta z = \Delta$, the criteria is written as follows

$$\Delta t \le \frac{1}{c\sum_{i=0}^{L_s-1}|a(l)|\sqrt{\left(\frac{1}{\Delta^2}+\frac{1}{\Delta^2}+\frac{1}{\Delta^2}\right)}} = \frac{\Delta}{c\sum_{i=0}^{L_s-1}|a(l)|\sqrt{3}} \tag{D.13}$$

It can be easily seen that in the two-dimensional case, for a uniform mesh in *x*-*z* plane, the relation becomes

$$\Delta t \leq s \frac{\Delta}{c}, \tag{D.14}$$

where *s* stand for the Courant number and can be evaluated by

$$s = \frac{1}{\sqrt{2}\sum_{l=0}^{L_s-1}|a(l)|} \tag{D.15}$$

The Courant number represents the stability factor in two dimensions and highly relies on the order of the utilised basis functions [98]. From equation (D.14) it is obvious that time limit, compared to time limit for FDTD scheme, is smaller when the same cell size is adopted. While a coarser grid resolution is allowed. Consequently, overall accurate and efficient results can be obtained.

The general formula of the stability condition, for any MRTD basis and any level of wavelet resolution is demonstrated in [19] as

$$\Delta t \leq \frac{1}{c\sum_{l=-L_s}^{L_s}|a(l)|\sqrt{\left(\frac{1}{u_x\Delta x}\right)^2+\left(\frac{1}{u_y\Delta y}\right)^2+\left(\frac{1}{u_z\Delta z}\right)^2}} \tag{D.16}$$

Appendix E

E.1 Uniaxial Perfectly Matched Layers

The two dimensional S-MRTD scheme has been used in conjunction with the UPML scheme, first introduced by Gedney in 1996 [87], that rigorously truncates the computational domain. Contrasted to Perfectly Matched Layer (PML) scheme proposed by Berenger [47] and based on a non-physical split-field [47], this formulation considers the edge layer as an artificial anisotropic and uniaxial absorbing material by translating the mathematical model of PML into a physical one.

The key advantage of UPML formulation is that it does not require any splitting of the electromagnetic field component, although the absorbing characteristics remain unaffected. In order to establish a foundation for discussion of UPML, the derivation of the properties of this non-physical medium is shown in this section and can be found in full details in [47]. In order to do so, a two dimensional space is considered as illustrated in figure E.1.

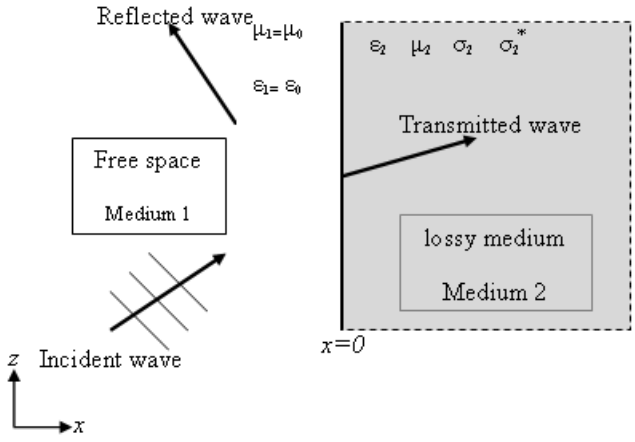

Figure E.1 Schematic diagram of a 2D *TEy* polarised plane wave propagating between two media

Figure E.1 shows a TE_y polarised uniform plane wave that is propagating on free-space towards an uniaxial medium which interference is at $x = 0$, whose electric and magnetic tensors are given by [10] $\overline{\overline{\varepsilon}} = \varepsilon_2 \overline{\overline{s}}$, $\overline{\overline{\mu}} = \mu_2 \overline{\overline{s}}$ where

$$\overline{\overline{s}} = \begin{bmatrix} s_x^{-1} & 0 & 0 \\ 0 & s_x & 0 \\ 0 & 0 & s_x \end{bmatrix} \tag{E.1}$$

where ε_2, μ_2 are the electric permittivity and the magnetic permeability, respectively, of the uniaxial medium in medium 2.

$$s_i = k_i + \frac{\sigma_i}{j\omega\varepsilon_0} \quad i = x, y \text{ or } z \tag{E.2}$$

The parameters k_i absorb the energy of evanescent waves that reach the UPML layers while σ_i are attenuation factors in the UPML region. No reflection is generated, and the plane wave is entirely transmitted into the uniaxial region for all angles of incidence θ. Such a medium is fundamentally indistinguishable to the PML proposed by Berenger and its defined UPML due to its uniaxial anisotropy. Each side of MRTD grid can be bounded with layer of UPML. However, there are areas in which the UPML itself is not uniaxial in strict sense of the definition. These areas are the corner regions as shown, for a 2D case, in figure E.2

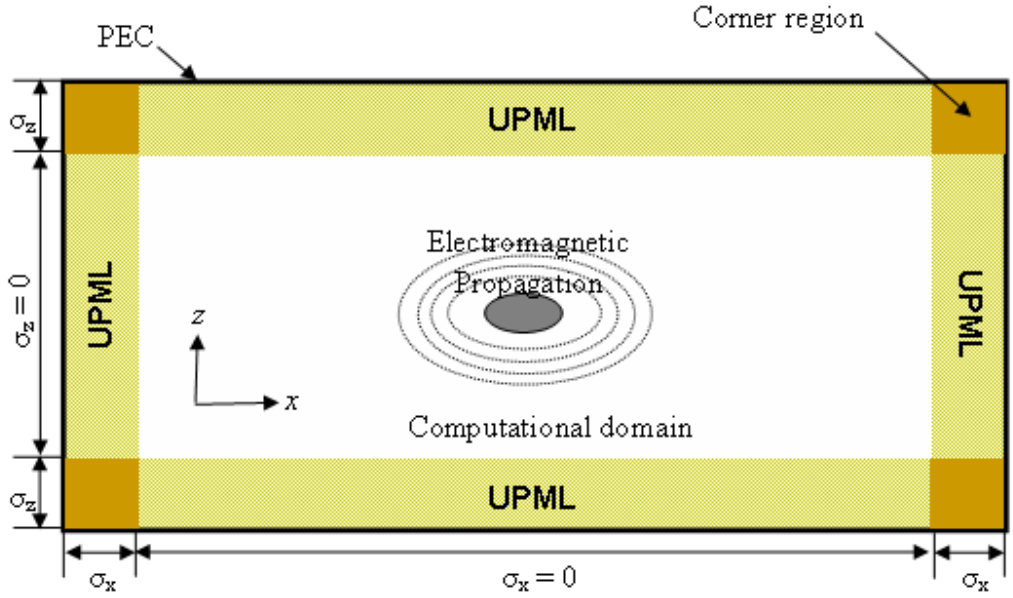

Figure E.2 Schematic diagram of UPML boundary condition for a 2D-TE_y MRTD grid

It can be noticed from this figure that in corner areas there is superposition of different UPML layers. In this case, the expression of the tensor that multiplies the electric permittivity and magnetic permeability for this medium is given by

$$\overline{\overline{s}} = \begin{bmatrix} s_x^{-1} & 0 & 0 \\ 0 & s_x & 0 \\ 0 & 0 & s_x \end{bmatrix} \cdot \begin{bmatrix} s_z & 0 & 0 \\ 0 & s_z^{-1} & 0 \\ 0 & 0 & s_z \end{bmatrix} = \begin{bmatrix} s_x^{-1} s_z & 0 & 0 \\ 0 & s_x s_z^{-1} & 0 \\ 0 & 0 & s_x s_z \end{bmatrix} \tag{E.3}$$

with s_x and s_y defined as in equations (E.2). While the corner regions in a 3D case are shown in figure E.3.

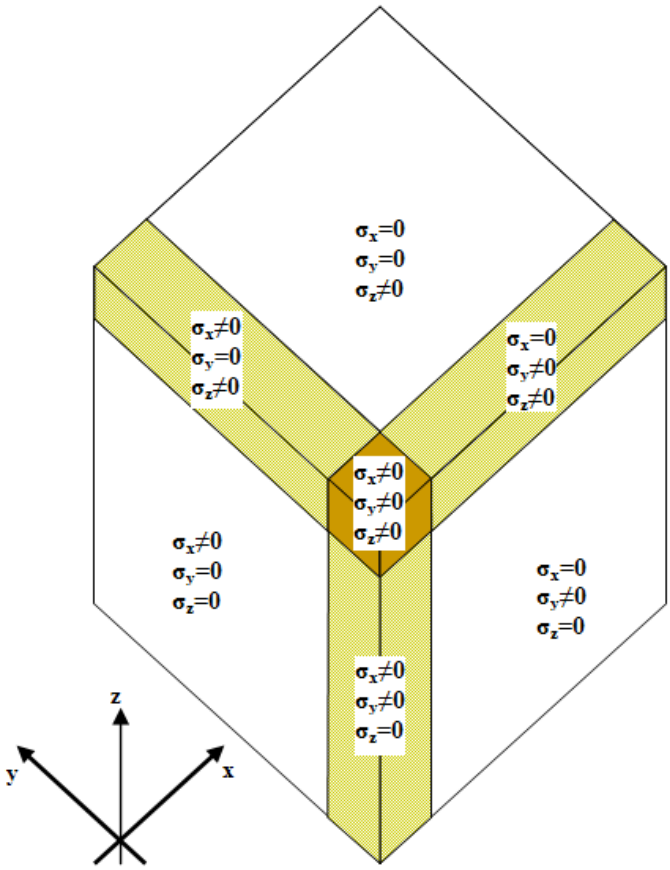

Figure E.3 Schematic diagram of UPML boundary condition for a 3D-TE_y MRTD grid

The tensor at the corner region is described as

$$\overline{\overline{s}} = \begin{bmatrix} s_x^{-1} & 0 & 0 \\ 0 & s_x & 0 \\ 0 & 0 & s_x \end{bmatrix} \cdot \begin{bmatrix} s_y & 0 & 0 \\ 0 & s_y^{-1} & 0 \\ 0 & 0 & s_y \end{bmatrix} \begin{bmatrix} s_z & 0 & 0 \\ 0 & s_z & 0 \\ 0 & 0 & s_z^{-1} \end{bmatrix} = \begin{bmatrix} s_x^{-1} s_y s_z & 0 & 0 \\ 0 & s_x s_y^{-1} s_z & 0 \\ 0 & 0 & s_x s_y s_z^{-1} \end{bmatrix} \quad \text{(E.4)}$$

E.2 UPML boundary condition in S-MRTD

The work carried out in this thesis uses the MRTD method to simulate the optical devices based on microcavity ring resonators. As such, the required mathematical derivations for the UPML boundary condition applied to MRTD technique are shown

here. The derivations are based on the previously introduced work in [10, 87] in the context of the FDTD algorithm.

Starting from Maxwell's equations in frequency domain

$$\nabla \times \overline{E} = -j\omega\mu_0 \overline{\overline{\mu}}\,\overline{H} \tag{E.5}$$

$$\nabla \times \overline{H} = j\omega\varepsilon_0 \overline{\overline{\varepsilon}}\,\overline{E} \tag{E.6}$$

In the UPML layers, applying for a 2D case for TE_y propagation, the time-domain equations (E.5) and (E.6) are written as [10]

$$\frac{\partial H_x}{\partial z} - \frac{\partial H_z}{\partial x} = j\omega\varepsilon_0 \frac{s_x s_z}{s_y} E_y \tag{E.7}$$

$$\frac{\partial E_y}{\partial z} = j\omega\mu_0 \frac{s_y s_z}{s_x} H_x \tag{E.8}$$

$$\frac{\partial E_y}{\partial x} = -j\omega\mu_0 \frac{s_x s_y}{s_z} H_z \tag{E.9}$$

Using the following proper constitutive relations

$$D_y = \varepsilon \frac{s_x}{s_y} E_y \tag{E.10}$$

$$B_x = \mu \frac{s_z}{s_x} H_x \tag{E.11}$$

$$B_z = \mu \frac{s_y}{s_z} H_z \tag{E.12}$$

The following relationships between *D*, *H*, *B*, and *E* in the UPML region are expressed as

$$\frac{\partial H_x}{\partial z} - \frac{\partial H_z}{\partial x} = \frac{\partial}{\partial t}\left(k_z D_y\right) + \frac{\sigma_z}{\varepsilon_0} D_y \tag{E.13}$$

$$\frac{\partial E_y}{\partial z} = \frac{\partial B_x}{\partial t} \tag{E.14}$$

$$-\frac{\partial E_y}{\partial x} = \frac{\partial}{\partial t}\left(k_x B_z\right) + \frac{\sigma_x}{\varepsilon_0} B_z \tag{E.15}$$

$$\frac{\partial D_y}{\partial t} = \varepsilon\left(\frac{\partial}{\partial t}(k_x E_y) + \frac{\sigma_x E_y}{\varepsilon_0}\right) \tag{E.16}$$

$$\frac{\partial}{\partial t}\left(k_x B_x\right) + \frac{\sigma_x}{\varepsilon_0} B_x = \mu\left[\frac{\partial}{\partial t}\left(k_z H_x\right) + \frac{\sigma_z}{\varepsilon_0} H_x\right] \tag{E.17}$$

$$\frac{\partial}{\partial t}\left(k_z B_z\right) + \frac{\sigma_z}{\varepsilon_0} B_z = \mu\left[\frac{\partial H_z}{\partial t}\right] \tag{E.18}$$

Following the Galerkin's method, the above equations are descretised by testing them with scaling function in space domain. In this regard, second-order central difference in time domain is approved. While two-steps update scheme for each field component is achieved. Referring to the geometry of the grid in figure 3.1, and with $k_i = 1$ and $\sigma_y = 0$, the following set of discretised equations is obtained

$${}_n B^{x,\varphi}_{i+\frac{1}{2},j} = {}_{n-1}B^{x,\varphi}_{i+\frac{1}{2},j} - \Delta t \sum_{l=-L_s}^{L_s-1} a(l)\left(\frac{E^{y,\varphi}_{i+\frac{1}{2},j+l+\frac{1}{2}}}{\Delta z}\right) \tag{E.19}$$

$${}_n H^{x,\varphi}_{i+\frac{1}{2},j} = \left(\frac{2\varepsilon_0 - \sigma_z \Delta t}{2\varepsilon_0 + \sigma_z \Delta t}\right){}_{n-1}H^{x,\varphi}_{i+\frac{1}{2},j} + \left(\frac{2\varepsilon_0 + \sigma_x \Delta t}{2\varepsilon_0 + \sigma_z \Delta t}\right)\frac{1}{\mu_0}{}_n B^{x,\varphi}_{i+\frac{1}{2},j} - \left(\frac{2\varepsilon_0 - \sigma_x \Delta t}{2\varepsilon_0 + \sigma_z \Delta t}\right)\frac{1}{\mu_0}{}_{n-1}B^{x,\varphi}_{i+\frac{1}{2},j} \tag{E.20}$$

$${}_n B^{z,\varphi}_{i,j+\frac{1}{2}} = \left(\frac{2\varepsilon_0 - \sigma_x \Delta t}{2\varepsilon_0 + \sigma_x \Delta t}\right){}_{n-1}B^{z,\varphi}_{i,j+\frac{1}{2}} + \left(\frac{2\varepsilon_0 \Delta t}{2\varepsilon_0 + \sigma_x \Delta t}\right)\sum_{l=-L_s}^{L_s-1} a(l)\left(\frac{E^{y,\varphi}_{i+l+\frac{1}{2},j+\frac{1}{2}}}{\Delta x}\right) \tag{E.21}$$

$${}_n H^{z,\varphi}_{i,j+\frac{1}{2}} = {}_{n-1}H^{z,\varphi}_{i,j+\frac{1}{2}} + \left(\frac{2\varepsilon_0 + \sigma_z \Delta t}{2\varepsilon_0}\right)\frac{1}{\mu_0}{}_n B^{z,\varphi}_{i,j+\frac{1}{2}} - \left(\frac{2\varepsilon_0 - \sigma_z \Delta t}{2\varepsilon_0}\right)\frac{1}{\mu_0}{}_{n-1}B^{z,\varphi}_{i,j+\frac{1}{2}} \tag{E.22}$$

$$ {}_{n+\frac{1}{2}}D^{y,\varphi}_{i+\frac{1}{2},j+\frac{1}{2}} = \left(\frac{2\varepsilon_0 - \sigma_z \Delta t}{2\varepsilon_0 + \sigma_z \Delta t}\right) {}_{n}D^{y,\varphi}_{i+\frac{1}{2},j+\frac{1}{2}} + \left(\frac{2\varepsilon_0 \Delta t}{2\varepsilon_0 + \sigma_z \Delta t}\right) \sum_{l=-L_s}^{L_s-1} a(l) \left(- \frac{{}_{n}H^{x,\varphi}_{i+\frac{1}{2},j-l-1}}{\Delta z} + \frac{{}_{n}H^{z,\varphi}_{i-l-1,j+\frac{1}{2}}}{\Delta x} \right) \tag{E.23} $$

$$ {}_{n+\frac{1}{2}}E^{y,\varphi}_{i+\frac{1}{2},j+\frac{1}{2}} = \left(\frac{2\varepsilon_0 - \sigma_x \Delta t}{2\varepsilon_0 + \sigma_x \Delta t}\right) {}_{n}E^{y,\varphi}_{i+\frac{1}{2},j+\frac{1}{2}} + \left(\frac{2\varepsilon_0}{\varepsilon_0 \varepsilon_{i+\frac{1}{2},j+\frac{1}{2}} (2\varepsilon_0 + \sigma_x \Delta t)} \right) \left({}_{n+\frac{1}{2}}D^{y,\varphi}_{i+\frac{1}{2},j+\frac{1}{2}} - {}_{n-\frac{1}{2}}D^{y,\varphi}_{i+\frac{1}{2},j+\frac{1}{2}} \right) \tag{E.24} $$

where ε is the permittivity of the medium, σ_x , σ_z are the electric conductivity of the UPML layers. So as to optimise the absorption properties of the UPML layers, the parameters σ_i (i=x, z) must have a proper spatial distribution in the UPML regions.

Here, the geometric grading profile has been adopted so that

$$ \sigma_i(i) = \frac{\sigma_{\max} \, i^m}{d^m} \tag{E.25} $$

where d is the depth of the UPML, m stands for the order of the polynomial variation. The selection of σ_{max} that minimises the reflection from boundaries is [99]

$$ \sigma_{\max} \approx \frac{(m+1)}{150 \pi \Delta \sqrt{\varepsilon_r}} \tag{E.26} $$

where Δ is the uniform spatial discretisation adopted.

Appendix F

F.1 2-D S-MRTD code with UPML absorbing boundary condition

```
!!!!!!!!!!!!!!!!!!!!!!!!!!!!!!!!!!!!!!!!!!!!!!!!!!!!!!!!!!!!!!!!!!!!!!!!!!!!!!!!!!!!!!!!!!!!!!!!!!!!!!!!!!!!!!!!!!!!!!!

!                    2-D MRTD code with UPML absorbing boundary condition

!!!!!!!!!!!!!!!!!!!!!!!!!!!!!!!!!!!!!!!!!!!!!!!!!!!!!!!!!!!!!!!!!!!!!!!!!!!!!!!!!!!!!!!!!!!!!!!!!!!!!!!!!!!!!!!!!!!!!!!

!     Program Author: Nabeil Abduljallil Abubaker Abujnah

!                            Faculty of Advanced Technology

!                            University of Glamorgan

!                            Pontypridd, CF37 1DL

!                            Wales, UK

!        Copy right 2011

!!!!!!!!!!!!!!!!!!!!!!!!!!!!!!!!!!!!!!!!!!!!!!!!!!!!!!!!!!!!!!!!!!!!!!!!!!!!!!!!!!!!!!!!!!!!!!!!!!!!!!!!!!!!!!!!!!!!!!!

implicit none

real(8), parameter::pi=3.14159265358979, c0= 2.99792458d8, n_1=10

real(8), parameter::mu0=4.*pi*1.d-7, eps0=1./(c0**2*mu0)

real(8), parameter:: epsr1=10.24, epsr2=1

real(8), parameter::taus=20d-15, delays=80d-15

real(8), parameter::ix=444, iz=444

real(8), parameter::n_step=25000

real(8), parameter::ix_out1m=2.5e-6,ix_out2m=9.599e-06

real(8), parameter::iz_out3m=6.0495e-6

real(8), parameter::ix_sorm=1.46e-6
```

```
real(8), parameter::pmlx=20, pmlz=20

real(8), parameter::dx=0.02725d-6, dz=0.02725d-6

real(8), parameter::Ls=5, q=0.1

!!!!!!!!!!!!!!!!!!!!!!!!!!!!!!!!!!!!!!!!!!!!!!!!!!!!!!!!!!!!!!!!!!!!!!!!!!!!!!!!!!!!!!!!!!!!!!!!!!!!!!!!!!!!!!!!

!!!!                    Declare Parameters

!!!!!!!!!!!!!!!!!!!!!!!!!!!!!!!!!!!!!!!!!!!!!!!!!!!!!!!!!!!!!!!!!!!!!!!!!!!!!!!!!!!!!!!!!!!!!!!!!!!!!!!!!!!!!!!!

real(8), dimension(ix,iz):: ey, hx, hz, dy,eppy, epy,hpx,hpz,dpy,sigmax , sigmaz, bpx,

bpxold, bpz, bpzold, dpyold

real(8), dimension(ix,iz):: eps_inf, coe1, coe2, der1,der2,der3,der3old, num_hpx,

denom_hpx, num_bpz, denom_bpz

real(8)::                  lambda_f, omega_f, dt, tem, lambda_sh,

etax,etaz,r0,sigmax0,sigmaz0,kx,kz,sigmaxm,sigmazm

real(8), dimension(1,21):: Ey_out, Ey_ing, Ey1, Ey2,Hz1,Hz2,Hx1,Hx2,Ey3,Ey4

,Hx3,Hx4,Hz3,Hz4

real(8), dimension(1,iz):: te_ey, Ey_1,Ey_2,Ey_3,Ey_4, Hz_1,Hz_2,Hz_3,Hz_4

real(4)::                 dur,field

real(4)::                 c,z,m, tau, delay, ix_out1, ix_out2,iz_out3, ix_sor

real(8), dimension(n_step):: source1, energy1, energy2

integer::                 i,j,p,n,t1,t2,rat,rat2,n_2,nn,nnn,r,s,l,nc,t3,t4,Nf,Nsh,shift

real(8), dimension(1,2*Ls):: a_4,a_2,a_cdf_24, a_cdf_26


!!!!!!!!!!!!!!!!!!!!!!!!!!!!!!!!!!!!!!!!!!!!!!!!!!!!!!!!!!!!!!!!!!!!!!!!!!!!!!!!!!!!!!!!!!!!!!!!!!!!!!!!!!!!!!!!

open(unit=100, file='eps_inf.dat', status='old')
```

```
open(unit=151, file='te_ey.dat', status='old')

open(unit=153, file='CDF(2,4).dat', status='old')

!!!!!!!!!!!!!!!!!!!!!!!!!!!!!!!!!!!!!!!!!!!!!!!!!!!!!!!!!!!!!!!!!!!!!!!!!!!!!!!!!!!!!!!!!!!!!!!!!!!!!!!!!!!!!!!!!!!!!!!

!                  This step is to open new files to be used to store the calculated Data          !

!!!!!!!!!!!!!!!!!!!!!!!!!!!!!!!!!!!!!!!!!!!!!!!!!!!!!!!!!!!!!!!!!!!!!!!!!!!!!!!!!!!!!!!!!!!!!!!!!!!!!!!!!!!!!!!!!!!!!!!

open(unit=157, file='sigmax.dat', status='unknown')

open(unit=158, file='sigmaz.dat', status='unknown')

open(unit=108, file='ddt.dat')

open(unit=109, file='der1.dat')

open(unit=110, file='der2.dat')

open(unit=111, file='eppy.dat')

open(unit=112, file='hppx.dat')

open(unit=113, file='hppz.dat')

open(unit=902, file='dt', status='unknown')

open(unit=903, file='Ey1', status='unknown')

open(unit=904, file='Ey2', status='unknown')

open(unit=905, file='Ey3', status='unknown')

open(unit=906, file='Ey4', status='unknown')

open(unit=909, file='Hz1', status='unknown')

open(unit=910, file='Hz2', status='unknown')

open(unit=916, file='Hx2', status='unknown')
```

```
!!!!!!!!!!!!!!!!!!!!!!!!!!!!!!!!!!!!!!!!!!!!!!!!!!!!!!!!!!!!!!!!!!!!!!!!!!!!!!!!!!!!!!!
!                        Reading data                                    !
!!!!!!!!!!!!!!!!!!!!!!!!!!!!!!!!!!!!!!!!!!!!!!!!!!!!!!!!!!!!!!!!!!!!!!!!!!!!!!!!!!!!!!!
do i=1,ix
read(100,3000) (eps_inf(i,j), j=1,iz)
end do
!!!!!!!!!!!!!!!!!!!!!!!!!!!!!!!!!!!!!!!!!!!!!!!!!!!!!!!!!!!!!!!!!!!!!!!!!!!!!!!!!!!!!!!!
!            stability criterion                                         !
!!!!!!!!!!!!!!!!!!!!!!!!!!!!!!!!!!!!!!!!!!!!!!!!!!!!!!!!!!!!!!!!!!!!!!!!!!!!!!!!!!!!!!!!
dt=q*(dx/c0)
write(*,*) 'step dt=' , dt
write(902,5000) dt
n_2=n_step/n_1
lambda_f=1.5d-6
omega_f=2.*pi*c0/lambda_f
coe2=eps0*eps_inf
kx=1
kz=1
m=2.5
etaz=sqrt(mu0/(eps0*epsr1))
etax=sqrt(mu0/(eps0*epsr2))
field=0.
sigmaxm=(m+1)/(150*pi*dx*sqrt(epsr2))
```

```
do i=Ls+1,pmlx+Ls
sigmax(i,Ls:iz-Ls)=sigmaxm*((pmlx+Ls-i+1)/pmlx)**m
end do
do i=ix-pmlx+1-Ls,ix-Ls
sigmax(i,Ls:iz-Ls)=sigmaxm*((i-ix+pmlx+Ls)/pmlx)**m
end do
sigmax(pmlx+Ls+1:ix-pmlx-Ls,Ls:iz-Ls)=0
sigmazm=(m+1)/(150*pi*dz*sqrt(epsr1))
do j=Ls+1,pmlz+Ls
end do
do j=iz-Ls-pmlz+1,iz-Ls
sigmaz(Ls:ix-Ls,j)=sigmazm*((j-iz+pmlz+Ls)/pmlz)**m
end do
sigmaz(Ls:ix-Ls,Ls+pmlz+1:iz-Ls-pmlz)=0
do i=1,ix
write(157,3000) (sigmax(i,j), j=1,iz)
write(158,3000) (sigmaz(i,j), j=1,iz)
end do
!!!!!!!!!!!!!!!!!!!!!!!!!!!!!!!!!!!!!!!!!!!!!!!!!!!!!!!!!!!!!!!!!!!!!!!!!!!!!!!!!!!!!!!!!!!!!!
!!! COEFFICIENT CALCULATING
!!!!!!!!!!!!!!!!!!!!!!!!!!!!!!!!!!!!!!!!!!!!!!!!!!!!!!!!!!!!!!!!!!!!!!!!!!!!!!!!!!!!!!!!!!!!!!
do r=1,ix
do s=1,iz
```

```
num_bpz(r,s)=2*eps0*kx-sigmax(r,s)*dt
denom_bpz(r,s)=2*eps0*kx+sigmax(r,s)*dt
num_hpx(r,s)=2*eps0*kz-sigmaz(r,s)*dt
denom_hpx(r,s)=2*eps0*kz+sigmaz(r,s)*dt
end do
end do
delay=real(delays)/real(dt)
write(*,*) delay
tau=real(taus)/real(dt)
write(*,*) 'tau=', tau
ix_sor=int(real(ix_sorm)/real(dx))
write(*,*) 'ixsor=', ix_sor
ix_out1=int(real(ix_out1m)/real(dx))
write(*,*) 'ix_out1=', ix_out1
ix_out2=int(real(ix_out2m)/real(dx))
iz_out3=int(real(iz_out3m)/real(dx))
do n=1,n_step
tem=((real(n-delay)/real(tau))**2)
end do
do nn=1,n_2
call system_clock(t1,rat)
do nnn=1,n_1
  n=n_1*(nn-1)+nnn
```

```
der1=0
der2=0
der3=0
do r=Ls,ix-Ls-1
do s=Ls,iz-Ls-1
  do l=1,2*Ls
  der1(r,s)=der1(r,s)+a_cdf_24(1,l)*(epy(r,s-(l-Ls)+1))
  end do
end do
end do
do r=Ls,pmlx+Ls
do s=Ls,iz-1-Ls
  bpx(r,s)=bpx(r,s)-(dt/dz)*der1(r,s)
end do
end do
do r=ix-pmlx-Ls,ix-Ls-1
do s=Ls,iz-1-Ls
  bpx(r,s)=bpx(r,s)-(dt/dz)*der1(r,s)
end do
end do
do r=Ls,ix-Ls-1
do s=Ls,Ls+pmlz
  bpx(r,s)=bpx(r,s)-(dt/dz)*der1(r,s)
```

```
end do
end do
do r=Ls,ix-Ls-1
do s=iz-Ls-pmlz,iz-Ls-1
  bpx(r,s)=bpx(r,s)-(dt/dz)*der1(r,s)
hpx(r,s)=(num_hpx(r,s)/denom_hpx(r,s))*hpx(r,s)+(1/(denom_hpx(r,s)*mu0))*(denom_
bpz(r,s)*bpx(r,s)-num_bpz(r,s)*bpxold(r,s))
end do
bpxold=bpx
do r=Ls+pmlx+1,ix-Ls-1-pmlx
do s=Ls+pmlz+1,iz-Ls-1-pmlz
  hpx(r,s)=hpx(r,s)-(dt/(mu0*dz))*der1(r,s)
end do
end do
do r=Ls,ix-Ls-1
do s=Ls,iz-Ls-1
  do l=1,2*Ls
  der2(r,s)=der2(r,s)+a_cdf_24(1,l)*(epy(r-(l-Ls)+1,s))
  end do
end do
end do
do r=Ls,ix-Ls-1
do s=Ls,Ls+pmlz
```

```
bpz(r,s)=(num_bpz(r,s)/denom_bpz(r,s))*bpz(r,s)+((2*dt*eps0)/dx/denom_bpz(r,s))*der
2(r,s)
  hpz(r,s)=hpz(r,s)+(denom_hpx(r,s)/(2*eps0*mu0))*bpz(r,s)-
(num_hpx(r,s)/(2*eps0*mu0))*bpzold(r,s)
end do
end do
do r=Ls,ix-Ls-1
do s=iz-Ls-pmlz,iz-Ls-1
   hpz(r,s)=hpz(r,s)+(denom_hpx(r,s)/(2*eps0*mu0))*bpz(r,s)-
(num_hpx(r,s)/(2*eps0*mu0))*bpzold(r,s)
end do
end do
do r=Ls,Ls+pmlx
do s=Ls,iz-Ls-1
bpz(r,s)=(num_bpz(r,s)/denom_bpz(r,s))*bpz(r,s)+((2*dt*eps0)/dx/denom_bpz(r,s))*der
2(r,s)
   hpz(r,s)=hpz(r,s)+(denom_hpx(r,s)/(2*eps0*mu0))*bpz(r,s)-
(num_hpx(r,s)/(2*eps0*mu0))*bpzold(r,s)
end do
end do
do r=ix-pmlx-Ls,ix-Ls-1
do s=Ls,iz-Ls-1
```

```
bpz(r,s)=(num_bpz(r,s)/denom_bpz(r,s))*bpz(r,s)+((2*dt*eps0)/dx/denom_bpz(r,s))*der
2(r,s)
end do
end do
bpzold=bpz
do r=Ls+pmlx+1,ix-Ls-1-pmlx
do s=Ls+pmlz+1,iz-Ls-1-pmlz
  hpz(r,s)=hpz(r,s)+(dt/(mu0*dx))*der2(r,s)
end do
end do
do r=Ls+1,ix-Ls
do s=Ls+1,iz-Ls
  do l=1,2*Ls
  der3(r,s)=der3(r,s)+a_cdf_24(1,l)*(-hpx(r,s-(l-Ls))/dz+hpz(r-(l-Ls),s)/dx)
  end do
end do
end do
do r=Ls+1,ix-Ls
do s=Ls+1,Ls+1+pmlz-1
dpy(r,s)=(num_hpx(r,s)/denom_hpx(r,s))*dpy(r,s)+((2*eps0*dt)/denom_hpx(r,s))*der3(
r,s)
epy(r,s)=(num_bpz(r,s)/denom_bpz(r,s))*epy(r,s)+((2*eps0)/(coe2(r,s)*denom_bpz(r,s))
)*(dpy(r,s)-dpyold(r,s))
```

```
end do
do r=Ls+1,ix-Ls
do s=iz-pmlz-Ls+1,iz-Ls
dpy(r,s)=(num_hpx(r,s)/denom_hpx(r,s))*dpy(r,s)+((2*eps0*dt)/denom_hpx(r,s))*der3(
r,s)
epy(r,s)=(num_bpz(r,s)/denom_bpz(r,s))*epy(r,s)+((2*eps0)/(coe2(r,s)*denom_bpz(r,s))
)*(dpy(r,s)-dpyold(r,s))
end do
end do
do r=Ls+1,Ls+pmlx
do s=Ls+1,iz-Ls
dpy(r,s)=(num_hpx(r,s)/denom_hpx(r,s))*dpy(r,s)+((2*eps0*dt)/denom_hpx(r,s))*der3(
r,s)
epy(r,s)=(num_bpz(r,s)/denom_bpz(r,s))*epy(r,s)+((2*eps0)/(coe2(r,s)*denom_bpz(r,s))
)*(dpy(r,s)-dpyold(r,s))
end do
end do
do s=Ls+1,iz-Ls
dpy(r,s)=(num_hpx(r,s)/denom_hpx(r,s))*dpy(r,s)+((2*eps0*dt)/denom_hpx(r,s))*der3(
r,s)
epy(r,s)=(num_bpz(r,s)/denom_bpz(r,s))*epy(r,s)+((2*eps0)/(coe2(r,s)*denom_bpz(r,s))
)*(dpy(r,s)-dpyold(r,s))
end do
```

```
end do
dpyold=dpy
do r=Ls+1+pmlx,ix-Ls-pmlx
do s=Ls+1+pmlz,iz-Ls-pmlz
 dpy(r,s)=dpy(r,s)+dt*(der3(r,s))
 end do
end do
epy(ix_sor,pmlz+Ls+1:iz-Ls-1)=epy(ix_sor,pmlz+1+Ls:iz-pmlz-1-
Ls)+te_ey(1,pmlz+1:iz-pmlz-1-Ls)*source1(n)
Ey1(1,1:21)=epy(ix_out1,106:126)
Ey2(1,1:21)=epy(ix_out2,106:126)
Ey3(1,1:21)=epy(298:318,iz_out3)
Ey4(1,1:21)=epy(ix_out1,318:338)
Hz1(1,1:21)=hpz(ix_out1,106:126)
Hz2(1,1:21)=hpz(ix_out2,106:126)
Hz3(1,1:21)=hpz(298:318,iz_out3)
Hz4(1,1:21)=hpz(ix_out1,318:338)
Hx1(1,1:21)=hpx(ix_out1,106:126)
Hx2(1,1:21)=hpx(ix_out2,106:126)
Hx3(1,1:21)=hpx(298:318,iz_out3)
Hx4(1,1:21)=hpx(ix_out1,318:338)
write(903,3000) Ey1(1,1:21)
write(904,3000) Ey2(1,1:21)
```

```
write(905,3000) Ey3(1,1:21)
write(906,3000) Ey4(1,1:21)
write(909,3000) Hz1(1,1:21)
write(910,3000) Hz2(1,1:21)
write(911,3000) Hz3(1,1:21)
write(912,3000) Hz4(1,1:21)
write(915,3000) Hx1(1,1:21)
write(916,3000) Hx2(1,1:21)
write(917,3000) Hx3(1,1:21)
write(918,3000) Hx4(1,1:21)
if (mod(n,1250).eq.0) then
do i=1,ix
write(950,3000) (epy(i,j), j=1,iz)
end do
end if
end do
3000 format(<iz>E25.16 E3)
6000 format(<ix>E25.16 E3)
4000 format(<n_step>E25.16 E3)
5000 format(1E25.16E3)
call system_clock(t2,rat)
dur=real(t2-t1)/real(rat)
field=field+dur
```

```
write(*,100) n,dur,field/60.
end do
write(*,*) 'TOTAL DURATION= ', field/60., 'MINTS'
100 format('STEP  n=  ', I9 , '  PARTIAL DURATION=  ' , F7.3,'  ELAPSED  ', F7.1 ,'
MINTS  ')
end program
```

Appendix G

G.1 MATLAB m. file to build up the MRR

```
%*************************************************************************
%  This MATLAB m-file build up the structure of interest that is going to be
%considered          (this code is for microcavity ring resonator)
%*************************************************************************
%   Program author: Nabeil Abduljallil Abubaker Abujnah                   %
%                Faculty of Advanced Technology
%                University of Glamorgan
%                Pontypridd
%                CF37 1DL
%                Wales, UK
%                naabujna@glam.ac.uk
%               Copyright 2011
%%%%%%%%%%%%%%%%%%%%%%%%%%%%%%%%%%%%%%%%%%%%%%%%%%%%%%%%%%%%%%%%%%%%%%%
clear all
clc
tic
c0=2.99792458e8;
mu0=4*pi*1e-7;
eps0=1/c0^2/mu0;
lambda0= 1.5e-06;
```

```
n1=1;

n3=n1;

n2=3.2;

g1=0.245e-06;

g2=g1;

W=0.3e-06;

R1=2.5e-06;

R2=R1-W;

d=(2*R1);

dx=0.02725e-06;

dz=dx;

Lx=12.099e-06;

ix=round(Lx/dx);

Loff=3e-06;

A=round(Loff/dx);

B=round(W/dz);

C=round(g1/dz);

D=round(R1/dx);

Loff=A*dx;

Lz1=(2*Loff)+(2*W)+(2*g1)+(2*R1);

iz=(2*A)+(2*B)+(2*C)+(2*D);

Lz=iz*dz;

   izcore1=A+1;
```

```
    izcore2=A+B;
    izcore3=(iz/2)+D+C;
    izcore4=izcore3+B-1;
    eps_00=[n1^2 n2^2 n3^2];
    DeltaZ=null(1,1);
    DeltaX=null(1,1);
    DeltaX=repmat(dx,ix);
    DeltaX=DeltaX(1,:);
    DeltaZ=repmat(dz,iz);
    DeltaZ=DeltaZ(1,:);
eps_inf(1:ix,1:iz)=eps_00(1);
eps_inf(1:ix,izcore1:izcore2)=eps_00(2);
eps_inf(1:ix,izcore3:izcore4)=eps_00(2);
fz=round(iz/2);
fx=round(ix/2);
for i=1:ix
    for j=1:iz
        if (R2^2<=(((i-fx)*dx)^2+((j-fz)*dz)^2) & (((i-fx)*dx)^2+((j-fz)*dz)^2) <= R1^2)
            eps_inf(i,j)=eps_00(2);
        end;
        end
end
DeltaZZ(1)=DeltaZ(1);
```

```
DeltaXX(1)=DeltaX(1);
for i=2:iz
      DeltaZZ(i)=DeltaZZ(i-1)+DeltaZ(i);
end
 for i=2:ix
    DeltaXX(i)=DeltaXX(i-1)+DeltaX(i);
end
figure (2)
surf(eps_inf)
shading flat
colorbar
view(2)
toc
save eps_inf.dat eps_inf -ascii -double
save DeltaX.dat DeltaX -ascii -double
save DeltaZ.dat DeltaZ -ascii -double
figure (3)
surf(DeltaZZ,DeltaXX,eps_inf)
xlabel('x')
ylabel('y')
xlabel('z')
view(2)
save DeltaXX.dat DeltaXX -ascii -double
```

```
save DeltaZZ.dat DeltaZZ -ascii –double

function [neff,Ey,Hz,x]=te(lambda0,n1,n2,n3,W,dx);

AA=input('Loff(this value have to be taken from the workspace )=');

Lz= input('Lz(this value have to be taken from the workspace )=');

LL=Lz-(AA+W);

k0=2*pi/lambda0;

c0=2.99792458e8;

f0=c0/lambda0;

mi0=1.256637061e-6;

neff=fzero(@(x)(k0*sqrt(n2^2-x^2)+...

   atan(sqrt((n2^2-x^2)/(x^2-n1^2)))+...

   atan(sqrt((n2^2-x^2)/(x^2-n3^2)))),[(n1+n1/1000) n2]);

alfa=-atan(G1/G2);

C1=1;

C2=-C1*G1/(G2*sin(alfa));

C3=-G2*sin(G2*W+alfa)*C2/G3;

x1=((-1*AA):dx:(0.0e-6-dx-dx));

x2=(0.0e-6:dx:(W-dx));

x3=(W:dx:((LL+W)));

Hz1=-G1/(j*(2*pi*f0)*mi0)*C1*exp(G1.*x1);

Hz2=G2/(j*(2*pi*f0)*mi0)*C2*sin(G2.*x2+alfa);

Hz3=G3/(j*(2*pi*f0)*mi0)*C3*exp(-G3.*(x3-W));

Ey1=C1*exp(G1.*x1);
```

```
Ey2=C2*cos(G2.*x2+alfa);

Ey3=C3*exp(-G3.*(x3-W));

Hz=[Hz1,Hz2,Hz3];

Hz=Hz/max(Hz);

Ey=[Ey1,Ey2,Ey3];

Ey=Ey/max(Ey);

x=[x1,x2,x3];

x=x/1e-6;

te_ey=abs(Ey);
```

References

[1] A. B. Matsko, (2009), "Practical Applications of Microresonators in Opticas and Photonics", *Taylor & Francis Group, Lcc*,

[2] A. Baby, and B. R. Singh, (2004), "Improve design of 8-channel silicon-on-insulator (SOI) arrayed waveguide grating (AWG) multiplexer using tapered entry into the slab waveguides", *Fibre and integrated Optics.*, Vol. 23, no. 5, pp. 365-373.

[3] A. Canciamilla, M. Torregiani, C. Ferrari, F. Morichetti, R. M. De La Rue, A. Samarelli, M. Sorel, A. Melloni, (2010), "Silicon coupled-ring resonator structures for slow light applications: potential, impairments and ultimate limits", *J. Opt*., vol. 12, pp. 1-7.

[4] A. Elshaari, A. Aboketak, S. F. Preble, (2010), "Controlled storage of light in silicon cavities", *Opt. Express*., Vol. 18, no. 3, pp. 3014-3022.

[5] A. Himeno, K. Kato, and T. Miya, (1998), "Silicon-based planar lightwave circuits", *IEEE J. of Selected Topic in Quantum Electronics.*, Vol. 4, no. 6, pp. 913-924.

[6] A. Guarino, G. Poberaj, D. Rezzonico, R. Degl'innocenti, and P. Gunter, (2007), "Electro-Optically tunable microring resonator in lithium niobate", *Nature Photonics.*, Vol. 1, pp. 407-410.

[7] A. Melloni, and M. Martinelli, (2002), "Synthesis of direct- coupled resonators bandpass filter for WDM systems", *J. lightwave Technol*., Vol. 20, no. 2, pp. 296-303.

[8] A. Melloni, F. Morichetti, C. Ferrari, M. Martinelli, (2008), " Continuously tunable 1- byte delay in coupled-resonator optical waveguides", *Opt. Lett.*, Vol. 33, no. 20, pp. 2389- 2391.

[9] A. R. Bushyagen, and M. M. Tentzeris, (2005), "Multiresolution time Domain in electromagnetic," *1*st *ed, USA:* Morgan & Claypool.

[10] A. Taflove, and S. C. Hagness, (2005), *Computational Electrodynamics: the finite-difference time-domain method*, Artech House.

[11] A. Yariv, (1973), "Coupled-Mode Theory for Guided-Wave Optics", IEEE journal of Quantum Electronics, Vol. 9, no. 9, pp. 919-933.

[12] B. E. Little, S. T. Chu, H. A. Haus, J. Foresi, and J. P. Laine, (1997), "Microring resonator channel dropping filters", *J. lightwave Technol*., Vol. 15, no. 6, pp. 998-1005.

[13] B. E. Little, S. T. Chu, J.V. Hryniewicz, and P.P Absil, (2000), "Filter synthesis for periodically coupled microring resonators", *Opt.Lett*, Vol. 25, no.5, pp. 344-346.

[14] B. Mukherjee, (2000), "WDM Optical Communication Networks: Progress and Challenges", *IEEE journal on selected areas in communications*, Vol. 18, no. 10.

[15] C. G. Varzquez, S. E. Vargas, J. M. Sanchez-Pena, A. B. Gonzalo, (2004), 'Demultiplexers for ultranarrow channel spacing based on Mach-Zehnders and ring resonators', *Opt. Engineering*, Vol. 43, no. 9, pp. 2080-2086.

[16] C. K. Madsen, G. Lenz, A. J. Bruce, M. A. Capuzzo, L. T. Gomez , T. N. Nielsen, I. Brener, (1999), "Multistage dispersion compensator using ring resonators", *Opt. Lett.*, Vol. 24, no. 22, pp. 1555-1557.

[17] C. M. Furse, D. H. Roper, D. N. Buechler, D. A. Christensen, C. H. Durney, (2000), "The problem and treatment of DC offsets in FDTD simulations", *IEEE Trans. on Antennas and Propagation*, vol. 48, pp. 1198-1201.

[18] C. Ramakrishna, (2003), "Optical Communications: An overview", *International Conference on Electrical & Computer Enginerring (ICECE)*, 29th Oct-1st Nov.2003.

[19] C. Sarris and L. P. B. Katehi, (2001), "Fundamental gridding-related dispersion effects in multiresolution time-domain schemes", *IEEE Trans. Microwave Theory Tech*., vol. 49, pp. 2248-2257.

[20] C. Varzquez, S. Vargas, J, M, S. Pena, (2000), "Design and tolerance analysis of a router with an amplified resonator and Bragg gratings", *Applied Opt*., Vol. 39, no. 12, pp. 1934-1940.

[21] C. Y. Chao, W. Fung, and L. J. Guo, (2006), "Polymer microring resonators for biochemical sensing applications", *IEEE J. Sel. Top. Quantum Electron.*, Vol. 12, no. 1, pp. 134-142.

[22] D. G. Rabus, M. Hamacher, U. Troppenz, and H. Heidrich, (2002), " High-Q channel- dropping filters using ring resonators with integrated SOA's", *IEEE J. Photon. Technol. Let.*, Vol. 14, no. 10, pp. 1442-1444.

[23] D. G. Rabus, M. Hamacher, U. Troppenz, H. Heidrich, (2002), "Optical Filters Based on Ring Resonators With Integrated Semiconductor Optical Amplifiers in GaInAsP–InP", *IEEE Journal of Selected Topics in Quantum Electronics,* Vol. 8, no. 6, pp. 1405-1411.

[24] D. G. Rabus, (2007), *Integrated Ring Resonators: The compendium*. Springer-Verlag Berline Heidelberg.

[25] D. Rafizadeh, J. P. Zhang, S, C. Hagness, A. Taflove, K. A. Stair, and S. T. Ho, (2002), "Waveguide-Coupled AlGaAs/GaAs microcavity ring and disk resonators with high finesse and 21.6-nm free spectral range", *Optical Letters,* Vol. 22, no. 16, pp. 1244-1246.

[26] E. A. J. Marcatilt, (1969), "Bends in Optical Dielectric Guides", *J. The Bell System Technol J*, Vol. 48, no. 7, pp. 2103-2132.

[27] E. Krioukov, D. J. W. Klunder, A. Driessen, J. Greve, and C. Otto, (2002), "Sensor based on an integrated optical microcavities", *Optical Letters,* Vol. 27, no. 27,pp. 512-514.

[28] E. M. Tentzeris, R. L. Robertson, J. Harvey, and L. Katehi , (1999), " Satbility and dispersion analysis of Battle-Lemarie based MRTD scheme", *IEEE Trans.Microwave theory & Tech.,* Vol. 47, no. 7, pp. 1004 – 1013.

[29] F. Liu, Q. Li, Z. Zhang, M. Qin, Y. Su, (2008), "Optical Tunable delay Line in silicon Microring Resonator Based on thermal Nonlinear Effect", *Sel. Top. Quantum Electron*., Vol. 14,no. 3, pp. 706-712.

[30] F. Xia, L. Sekaric, Y. Vlasov, (2007), "Ultracompact Optical buffers on a silicon chip", *nature photon*., no. 1, pp. 65-71.

[31] G. Carat, R. Gillard, J. Citerne, and J. Wiart, (2000), "An efficient analysis of planar microwave circuits using a DWT-based Haar MRTD scheme", *IEEE Trans. Microwave Theory Tech*., vol. 48, pp. 2261-2270.

[32] G. Lenz, C. K. Madsen, (1999), "General Optical All-pass Filter structures for Dispersion control in WDM systems", *J. lightwave Technol*., Vol. 17, no. 7, pp. 1248-1254.

[33] G. Lifante, (2003), *Integrated Photonics Fundamentals*, Wiley.

[34] H. Nishihara, M. Haruna, and T. Suhara, (1989), "*Optical Integrated Circuits"*, McGrawHill.

[35] H. Simos, C. Hesaritakis, D. Alexandropoulos, D. Syyridis, (2007), "Intraband crosstalk propertie of add-drop filters based on active microring resonators", *IEEE Photon.Technol. Lett.*, Vol. 19, no. 20 pp. 1649-1651.

[36] H. Uetsuka, (2004), "AWG technologies for dense WDM applications", *IEEE J. Sel. Top. Quantum Electron.* , Vol. 10, no. 2, pp. 393-402.

[37] I. Neokosmidis, T. Kamalakis, T. Sphicopoulos, (2007), "Optical Delay Lines Based on Soliton Propagation in Photonic Crystal Coupled Resonator Optical Waveguides", *IEEE Quantum Electron*.,Vol. 43,no. 7, pp. 560-567.

[38] J. C. Maxwell, (1964), "A Dynamic Theory of the Electromagnetic Field".

[39] J. Gotze, J. E. Odegard, P. Rieder, and C. S. Burrus, (1996), "Approximate moments and regularity of efficiently implemented orthogonal wavelet transform", in *Proc. IEEE Int. Circuits Syst. Symp. Dig*., pp. 405-408.

[40] J. Haavisto, G. A. Pajer, (1980), "Resonance effects in low-loss ring waveguides", *Opt. Lett*,Vol. 12,no. 5, pp. 510—512.

[41] J H. Shapiro, (2009), "The Quantum Theory of Optical Communications", *IEEE journal on selected topics in quantum electronics*, Vol. 15, no. 6.

[42] J. Khurgin, (2005), "Adiabatically tunable optical delay lines and their performance limitations ", *Opt. Lett*, Vol. 30, no. 20 , pp. 2778-2780, 2005

[43] J. B. Khurgin, (2005), "Slowing and stopping photons using backward frequency conversion in quasi-phase-matched waveguides", *Phys. Rev .A.*, Vol. 72, no. 2. p.023810.

[44] J. K. S. Poon , J. Scheuer, S. Mookherjea, G. T. Paloczi, Y. Y. Huang, A. Yariv, (2004), "Matrix analysis of microring coupled-resonator optical waveguides ", *Optics Express,*Vol. 12, no. 1, pp. 90-103.

[45] J. K. S. Poon, J. Scheuer, Y. Xu, A. Yariv, (2004), "Designing coupled-resonator optical waveguide delay lines", *J. Opt. Soc. Am. B,* Vol. 21, no. 9, pp. 1665-1673.

[46] J. Niegemann, W. Pernice, and K. Busch, (2009), " Simulation of Optical resonators using DGTD and FDTD", *Pure Appl. Opt J.*, Vol. 11, no. 11, pp. 1-10.

[47] J. P. Berenger, (1994), "A perfectly matched layer for the absorption of electromagnetic waves", *J. Comput. Phys*., vol. 114, pp. 185-200.

[48] J. Yang, Q. Zhou and R. T. Chen, (2002), "Polymer-waveguide-based thermal Optical Switch using total-internal-reflection effect", *Appl. Phys. Lett.*, Vol. 81, no. 16, pp. 2947-2949.

[49] K. Honda, E. M. Garmire, K. E. Wilson, (1984), "Characteristics of an integrated optics ring resonator fabricated in glass", *J. Lightwave Technol*,Vol. 5, no. 2, pp. 714-719.

[50] K. J. Vahala, (2003), "Optical Microcavities", *Nature*, Vol. 424, no. 6950, pp. 839-846.

[51] K. Oda, , N. Takato, and H. Toba, (1991), "A wide-FSR waveguide Double-Ring Resonator for optical FDM Transmission systems", J. *lightwave Technol.*, Vol. 9, no. 6, pp. 728-736.

[52] K. Okamoto, (2006), *Fundamental of Optical Waveguides*, Elsevier.

[53] K. R. Hiremath, (2009), "Analytical modal analysis of bent slot waveguides", *J. Opt.Soc. Am. A*, Vol. 26, no. 11, pp.2321-2326.

[54] K. S. Kunz and R. J. Luebbers, (1993), *Finite Difference Time Domain Method for Electromagnetics*, CRC PRESS.

[55] K. Vahala, (2004), "Opical resonators and filters", *in optical Microcavities*, London, UK: Would Scientific, pp. 1-32.

[56] L B. Soldano, and E. C. M. Pennings, (1995), "Optical Multimode Interference Devices Based on Self-imaging: Principles and applications", *J. Lightwave Technol.*, Vol. 13, no. 4, pp. 615-627.

[57] L. Caruso, I. Montrosset (2003), "Analysis of a racetrack microring resonator with MMI coupler", *J. lightwave Technol*., Vol. 21, no. 1, pp. 206-210.

[58] L. Eldada, (2004), "Optical Communication Components", *Review of Scientific Instrument*, Vol. 75, no. 3.

[59] L. Rayleigh, (1912), "The Problem of the Whispering Gallery", *in Scientific Papers, Cambridge University, Cambridge, England*, Vol. 5, pp. 617—620, 1912.

[60] L. R. Dalton, B. H. Robinson, A. K. Y. Jen, W. H. Steier, R. Neilsen, (2003), "Systematic Development of High Bandwidth Low Drive Voltage Organic Electro-optics Devices and Their Applications", *Opt.mater*, Vol. 21, no. 1-3, pp. 19-28.

[61] M. Fujii and W. J. R. Hoefer, (2000), "Dispersion of time domain wavelet Galerkin method based on Daubechies compactly supported scaling functions with three and four vanishing moments", *IEEE Microwave Guided Wave Lett.*, vol. 10, pp. 125-127.

[62] M. Fujii, and W. J. R. Hoefer, (2001), "Application of Biorthogonal Interpolating Wavelets to the Galerkin Scheme of Time Dependent Maxwell's Equations", *IEEE Microwave & Wireless Components Lett.*, Vol. 11, no. 1, pp. 22 – 24.

[63] M. F. Yanik, S. Fan S, (2004), "Stopping light all optically ", *Phys.Rev.Lett.*, Vol. 92,no. 8 , pp. 1-18.

[64] M. F. Yanik, W. Suh, Z. Wang, S. Fan, (2004), "Stopping light in a waveguide with an all-optical analogue of electromagnetically induced transparency", *Phys. Rev. Lett*., Vol. 93, no. 23, p.233903.

[65] M. K. Chin, and S. T. Ho, (1998), "Design and Modeling of Waveguide-Coupled Single-Mode Microring Resonators ", *J. lightwave Technol.*, Vol. 11, no. 8, pp. 1433-1446.

[66] M. Koshiba, (1990), *Optical Waveguide Analysis*, McGrawHill.

[67] M. Kohtoku, S. Oku, Y. Kadota, Y. Shibata, Y. Yoshikuni, (2000), "200-GHz FSR Periodic Multi/Demultiplexer with Flattened Transmission and Rejection Band by Using a Mach–Zehnder Interferometer with a Ring Resonator", *IEEE Photon. Techn. Lett.*, Vol. 12, no. 9, pp. 1174-1176.

[68] M. Krumpholz, L. P. B. Katehi, (1996), "MRTD: New Time Domain Scheme Based on Multiresolution Analysis", *IEEE Trans.Microwave theory & Tech.*, Vol. 44, no. 4, pp. 555 – 571.

[69] M. K. Smit, E. C. M. Pennings, H. B. Blok, (1993), "A normalized approach to the design of low-loss optical waveguide bends", *J. Lightwave Technol*, Vol. 11,no. 11, pp. 1737-1742.

[70] M K. Smit, and C V. Dam, (1996), "Phasar Based WDM Devices: Principles, design and applications", *IEEE J. Sel. Top. Quantum Electron.* , Vol. 2, no. 2, pp. 236-250.

[71] M. Lee, M. E. Gehm, M. A. Neifeld, (2010), "Systematic design study of an all-optical delay line based on Brillouin scattering enhanced cascade coupled ring resonators", *J. Physics. Opt.*, Vol. 12, pp. 1-23.

[72] M Takenaka and Y. Nakano, (2007), "InP Photonic wire waveguide using InAlAs oxide cladding layer", *Opt. Express,* Vol. 15, no. 13, pp. 8422-4827.

[73] M S. Borella, J. P. Jue, D. B.anerjee, B. Ramamurthy, and B. Mukherjee, (1997), "Optical Components for WDM Lighwave Networks", IEEE *Proc.*, Vol. 85, no. 8.

[74] N. Bushyager, and E. M. Tentzeris, (2005), *MRTD (Multi Resolution Time Domain) Method in Electromagnetics*.

[75] P. G. Petropoulos, (1994), "Stability and phase error analysis of FD-TD in dispersive dieletrics", *IEEE Trans. Antennas Propag*., vol. 42, pp. 62-69.

[76] P. P. Absil, J. V. Hryniewicz, B. E. Little, R. A. Wilson, L. G. Joneckis, P. T. Ho, (2000), "Compact Microring Notch Filters", *IEEE Photon. Techn. Lett.*, Vol. 12, no. 4, pp. 398-400.

[77] P. P. Yupapin, W. Suwancharoen, (2007), "Chaotic signal generation and cancellation using a micro ring resonator incorporating an optical add/drop multiplexer", *Opt. Communications*, Vol. 280, no. 2, pp. 343-350.

[78] Q. Xu, D. Fattal, and R. G. Beausoleil, (2008), "Silicon microring resonators with 1.5-μm radius", *Opt. Express*,Vol. 16, no. 6,pp. 4309-4315.

[79] R. E. Slusher, (1994), "Optical processes in microcavities", *semicond. Sci. Technol*., Vol. 9, no. 11S, pp. 2025-2030.

[80] R. Grover, T. A. Ibrahim, T. N. Ding, Y. Leng, L. C. Kuo, S. Kanakaraju, K. Amarnath, L. C. Calhoun., and P. T. Ho, (2003), "Leterally coupled InP-based

single-mode microracetrack notch filter ", *IEEE Photon. Techn. Lett.*, Vol. 15, no. 8, pp. 1082 – 1084.

[81] R. Grover, V. Van, T. A. Ibrahim, P. P. Absil, L. C. Calhoun, F. G. Johnson, J. V. Hryniewicz, and P. T. Ho, (2005), "Parallel cascaded semiconductor microring resonators in high order and wide-FSR filters", *J. Lightw. Technol.*, Vol. 20, no. 5, pp. 900-905.

[82] R. Letizia, S. S. A. Obayya, (2008), "Efficient multiresolution Time Domain Analysis of Arbitrarily Shaped Photonic devices", *IET Optoelectronics.*, Vol. 2, no. 6, pp. 241 – 253.

[83] R. Ramponi, M. Marangoni, and R. Osellame, (2001), "Dispersion of the ordinary refractive-index change in a proton-exchanged $LiNbO_3$ Waveguide", *Appl. Phys. Lett.*, Vol. 78, no. 15, pp. 2098-2100.

[84] S. Arnold, (2001), "Microsheres photonic atoms and the physics of nothing", *Americn Scientist*, Vol. 89,no. 5, pp. 414-421.

[85] S. Blair, and Y. Chen, (2001), "Resonant-enhanced evanescent-wave fluorescence biosensing with cylindrical optical cavities", *Applied Optics*, Vol. 40, no. 4, pp. 570-582.

[86] S. C. Hagness, D. Rafizadeh, S. T. Ho, A. Taflove, (1997), "FDTD Microcavity Simulations: Design and Experimental Realization of Waveguide –Coupled Single-Mode Ring and Whispering-Gallery-Mode Disk Resonators", *J. Lightwave Technol.*, Vol. 15, no. 11, pp. 2154-2165.

[87] S. D. Gedney, (1996), "An anisotropic perfectly matched layer absorbing media for the truncation of FDTD lattice", *IEEE Trans. Antennas Propagat.*, vol. 44, pp. 1630-1639.

[88] S. J. Emelett, and R. A. Soref, (2005), "Synthesis of dual-microring–resonator crossconect filters", *Opt. Express*, Vol. 13, no. 20, pp. 4439-4456.

[89] S. Mikroulis, H. Simos, E. I. Rodit, and D. Syvridis, (2005), "Ultrafast all-optical AND logic operation based on four-wave mixing in a passive InGaAsP/InP microring resonator", *IEEE Photon. Technol. Lett.*, Vol. 17, no. 9, pp. 1878-1880.

[90] S. Mitatha, N. Pornsuwancharoen, P. P. Yupapin (2009), "A Simultaneous Short-Wave and Millimeter-WaveGeneration Using a Soliton Pulse Within a Nano-Waveguide", *IEEE Photon. Techn. Lett.*, Vol. 21, no. 13, pp. 932-934.

[91] S. Sandhu, M. L. Povinelli, M. F. Yanik, S. Fan, (2006), "Dynamically tuned coupled-resonator delay lines can be nearly dispersion free", *Opt. Lett*, 2006, Vol. 31, no. 13, pp. 1985-1987.

[92] S. Sandhu, M. L. Povinelli, S. Fan, (2007), "Stopping and time reversing a light pulse using dynamic loss tuning of coupled-resonator delay lines", *Opt. Lett*, Vol. 32, no. 22, pp. 3333-3335.

[93] S. Sohma, T Watannabe, T. Shibata, and H. Takahashi, (2005), "Compact and low power consumption 16 × 16 optical matrix switch with silicabased PLC technology", OFC2005, OThV4.

[94] S. Suzuki, K. Oda, and Y. Hibino, (1995), "Integrated-optics double-ring resonators with a wide free spectral range of 100 GHz", *J. lightwave Technol.*, Vol. 13, no. 8, pp. 1766-1771.

[95] S. Y. Tseng, C. Fuentes-Hernandez, D. Owens, and B. Kippelen, (2007), "Variable Splitting ratio 2 × 2 MMI Coupler using Multimode waveguide holograms", *Opt. Express.*, Vol. 15, no. 14, pp. 9015-9021.

[96] T. Barwicz, M. Popovic, M. R. Watts, P. T. Rakich, E. P. Ippen, and H. I. Smith, (2006), " Fabrication of add-drop filter based on frequency-matched microring resonators", *J. Lightwave Technol.*, Vol. 24, no. 5, pp. 2207-2218.

[97] T. Barwicz, M. R. Watts, M. A. Popovic, P. T. Rakich, L. Socci , F. X. Kartner, E. P. Ippen, and H. I. Smith, (2007), "Polarization-Transparent microphotonic devices in the strong confinement limit" , *Nature Photonics*, no. 1, pp. 57-60.

[98] T. Dogaru, and L. carin, (2001), "Multiresolution Time-Domain using CDF Biorthogonal Wavelets", *IEEE Trans on Microwave Theory & Tech.*, Vol. 49, no. 4, pp. 685 – 691.

[99] T. Dogaru, and L. Carin, (2002), "Application of Haar-wavelet-based multiresolution time-domain schemes to electromagnetic scattering problems", *IEEE Trans. Antennas Prop*., vol. 50, pp. 774-784.

[100] Theodor Tamir, (1990), "*Guided-Wave Optoelectronics*", Springer-Verlag., Springer Series in Electronics and Photonics, Vol. 96, 2nd ed.

[101] T. Ibrahim, K. Amarnath, L. Kuo, R. Grover, V. Van, and P. Ho, (2004), "Photonic logic NOR gate based on two symmetric microring resonators", *Opt. Lett*., Vol. 29,no. 23, pp. 2779-2781.

[102] V. Almedia, C. A. Barrios, R. Panepucci, M. Lipson, (2004),"All-optical control of light on a silicon chip", *Nature*, Vol. 431, pp1081-1084.

[103] V. R. Almeida, Q. Xu, C. A. Barrios, M. Lipson, (2004), "Guiding and confining light in void nanostructure", *Opt.lett*, Vol. 29, no. 11,pp.1209-1211.

[104] V. Sandoghdar, (1996), "Very low threshold whispering-gallery-mode microsphere laser", *Physical Review A*, Vol. 45, no. 3, pp. 1777-1780.

[105] V. Van, T. A. Ibrahim, K. Ritter, P. P. Absil, F. G. Johnson, R. Grover, J. Goldhar, and P. T. Ho, (2002), "All-optical nonlinear switching in GaAs-AlGaAs microring resonator", *IEEE Photon. Technol. Lett*., Vol. 14, no. 1, pp. 74-76.

[106] W. Y. Cheong, Y. M. Lee, K. H. Ra, J, G. Kang, and C. C. Shin, (1999), "Wavelet-Galerkin Scheme of time-dependent inhomogeneous electromagnetic problems ", *IEEE Microw. Guided Wave Lett.*, Vol. 9, no. 8, pp. 297 – 299.

[107] X. Zhu, T. Dogaru, and L. Carin, (2003), "Three-Dimensional Biorthogonal Multiresolution Time-Domain Method and its application to electromagnetic scattering poblems ", *IEEE Trans,On Antenna and Propag.*, Vol. 51, no. 5, pp. 1085 – 1092.

[108] Y. Asahara, S Nakayama, O. Maruyama, S. Ohmi, H. Sakai, and H. Takahashi, (1998), "Design and Characteristics of a demultiplex star coupler", OFC1998, WQ7.

[109] Y. Chen, Q. Cao, and R. Mittra, (2005), Multiresolution Time Domain Scheme for Electromagnetic Enginerring, john Wiley &Sons.

[110] Z. Bian, B. Liu, A. Shakouri, (2003), "InP-Based passive ring-resonator-coupled laser", *IEEE J. Quantum Electron.* , Vol. 39, no. 7, pp. 859-865.

[111] Z. S. Yang, N. H. Kwong, R. Binder, A. L. Smirl, (2005), "Distortionless light pulse delay in quantum-well Bragg structures", *Opt. Lett*, Vol. 33, no. 20, pp. 2790-2792.

List of Author Publications

As a result of hard work and intensive research throughout the duration of this PhD, a number of journal papers and conference papers have been submitted, accepted for publication, and presented. The journal papers are listed below

- N Abujnah, R Letizia, and S. S. A. Obayya, "Design Consideration of Microcavity Ring Resonators," *accepted for publication in IET Optoelectronics*.

- N Abujnah, R Letizia, and S. S. A. Obayya, "Time Domain Analysis of Optical Storage Based on Slotted Microcavity Ring Resonators," *under preparation to be submitted to IEEE Journal of Lightwave Technology*.

- N Abujnah, R Letizia, and S. S. A. Obayya, "Time Domain Simulation of Optical Delay Lines Based on Slotted Microcavity Ring Resonators," *under preparation to be submitted to IEEE Journal of Lightwave Technology*.

And the conferences papers are listed below

- N Abujnah, R Letizia, and S. S. A. Obayya, (2010), "MultiresolutionTime Domain Analysis of Microcavity Ring Resonator," submitted to the Semiconductor and Integrated Optoelectronics, SIOE'10, Cardiff, 2010.

- N Abujnah, R Letizia, and S. S. A. Obayya, (2010), "Accurate Time Domain Simulation of Optical Microcavity Ring Resonators," submitted to the International Workshop on Optical Waveguide Theory and Numerical Modelling, OWTNM'10, Cambridge, 2010.

- N Abujnah, R Letizia, and S. S. A. Obayya, (2010), "Accurate Multiresolution Time Domain Analysis of Microcavity Ring Resonators," presented at UK Semiconductors, Sheffield, July 2009.

- N Abujnah, R Letizia, and S. S. A. Obayya, (2009), "Accurate Time Domain Analysis of Microcavity Ring Resonaotr," presented at the Semiconductor and Integrated Optoelectronics, SIOE'09, Cardiff, April 2009.